7. EXPERIMENTAL VALIDATION OF A MATHEMATICAL MODEL FOR FIXED-BED DESULFURIZATION

7.1. Introduction

The tendency of various metal oxides to react with sulfur-containing compounds is used to remove such species (primarily H_2S) from coal-derived gas at high temperatures. Several supported or unsupported oxides, in single or mixed form, have been studied experimentally in the literature as candidate sorbents for hot coal gas desulfurization (for example, see studies by Caillet and Harrison (1982), Yumura and Furimsky (1985), Tamhankar et al. (1986), Gangwal et al. (1989), and Efthimiadis and Sotirchos (1991)). In most cases ZnO has been used as one of the active components of the sorbent, since many studies have shown that its use leads to very low equilibrium H_2S concentrations in the exit stream of the desulfurization reactor. Coal gas desulfurization is carried out in fixed-bed reactors, but other reactor configurations, such as moving and fluidized-bed reactors, are currently under study and development (Jain et al. (1990) and Lee et al. (1990)). Fixed-bed reactors are also used, almost exclusively, in experimental studies of the performance of coal gas desulfurization sorbents.

Mathematical models for fixed-bed reactors are very useful in design and scale-up studies, especially if they are capable of predicting the behavior of these units for different conditions from those at which they were tested and validated. They are also indispensable for the analysis of experimental data from lab-scale fixed-bed reactors employed in laboratory studies since, because of the very high rate of reaction of metal oxides with H_2S, it is practically impossible to achieve differential operation of such reactors. Desulfurization in fixed-beds is a complex process requiring consideration of a large number of subprocesses for its description. One has to consider mass transport in the particles, mass transport through the product layer formed in the interior of the particles, reaction at the unreacted- reacted solid interface, and evolution of the physical microstructure of the reacting particles. Since the concentrations of sulfur-containing pollutants in coal gas streams are typically low, small amounts of heat are released during the reaction, and consequently, consideration of heat transport is not necessary for the description of the

process. A mathematical model for a fixed-bed desulfurization reactor, therefore, consists of three submodels, one for describing mass transport and reaction in the bed, another for mass transport and reaction in the particles, and a third for local reaction and structure evolution within the particle or pellet.

The equations for mass transport and reaction in the fixed-bed are relatively well-defined. Thus, what really differentiates one fixed-bed model from another is the submodel used to describe the behavior of the individual sorbent pellets or particles in the bed. If one wants to avoid the complication of developing a theoretical single pellet model and testing it, the only available alternative is to use experimental data for single pellets or differential reactors to develop an experimental single pellet model, that is, a correlation for the dependence of the average reaction rate of the pellets (or particles) on solid conversion, temperature, and reactant concentration. Of course, such a model will be useful only if the conditions used in the operations of the fixed-bed are within the range used to develop the experimental model. Such an approach was taken, among others, by Park et al. (1984) in their study of the oxidation of reduced iron oxide with water vapor, a problem fundamentally similar to that of metal oxide sulfidation.

The performance of a mathematical model for coal gas desulfurization in fixed beds is examined in this study. The mathematical model is developed along the lines of fixed-bed desulfurization model by Sotirchos and Zarkanitis (1989). The random pore and grain models of Sotirchos and Yu (1985, 1988) for gas-solid reactions with solid product were used by Sotirchos and Zarkanitis to describe the behavior of individual pellets, but in our model, we will make use of the generalized random pore model of Yu and Sotirchos (1987), a model for reaction and structure evolution in porous media of pore-network structure undergoing a gas-solid reaction with solid product. Past studies on the sulfidation of two zinc oxide sorbents in a thermogravimetric analysis system (Efthimiadis and Sotirchos, 1991) showed that this structural model can successfully describe the behavior of single particles over a broad range of operating conditions. The fixed-bed desulfurization model is evaluated using experimental data for sulfidation of ZnO sorbents in a fixed-bed reactor, obtained in our laboratory at various combinations of operating conditions using the same two sorbents used in our past studies. No adjustable parameters are used in the comparison of

model predictions and experimental data since all parameters needed for the description of individual particles using the generalized random pore model have been determined independently from thermogravimetric analysis data.

7.2. Materials

The sorbents used in this study were mixtures of metal oxides with ZnO being the main constituent and other compounds (Al_2O_3, SiO_2, CaO, and MgO) being present in smaller amounts. The fresh materials were obtained from United Catalysts in the form of $3/16''$ extrusions with the commercial names: catalysts G-72D and C7-2. The unreacted materials showed some weight loss during the heat-treatment under nitrogen flow, most probably caused by removal of volatile compounds (binder solid and humidity). For this reason, the unreacted solids were heat-treated for 30 min at $600°C$ before each sulfidation experiment. The compositional analysis of the two sorbents showed that 89% of sample G-72D and 78% of sample C7-2, on a weight basis (after heat treatment), was zinc oxide. The rest was mainly alumina and silica in sample C7-2 and alumina in sample G-72D. The extrusions were crushed and divided into particle size ranges using mechanical sieving.

Zinc Oxide Sample	G-72D	C7-2	C7-2*
Total Pore Volume (Hg porosimetry), cm^3/g	0.178	0.289	0.275
BET Surface Area, m^2/g	26.57	27.72	25.52
Most Probable Radius (Hg Porosimetry), $\AA$	115	200	200
Most Probable Radius (N_2 Adsorption), $\AA$	125	180	200

Table 7.1: Physical properties of the unreacted heat-treated sorbents. (*=Second batch of sorbent C7-2).

Particles of 297-350 μm were used in the characterization of the pore structure of the solids. In Table 7.1 we summarize the physical properties of the unreacted heat-treated materials. Pores in the range of 10,000-20 Å were accounted for in the estimation of the pore volumes of Table 7.1 that were obtained from the mercury porosimetry data. The

physical properties of the micropores (pores of radius less than 20 Å) were computed using the t-method (De Boer et al., 1965). The small micropore volume and surface area of both materials and the pore size distributions of the solids (to be presented later in Figs. 7.13 and 7.14) showed that the pore space of both samples consists primarily of mesopores (pores with radius in the range 20-500 Å) and macropores (pores with radius larger than 500 Å).The BET surface area of the two sorbents is almost the same, but there is a significant difference in their pore volumes and most probable pore radii. (The most probable radius is the value where the slope of the cumulative pore volumes vs. pore radius curve has its maximum value). Sample C7-2* corresponds to a different batch of catalyst C7-2. It can be seen from the Table 7.1 that there are negligible differences between the physical properties of the two batches of sample C7-2. Moreover, when samples of the two batches were sulfided under identical reaction conditions, the conversion vs. time curves were, within experimental error, identical. A detailed investigation of the pore structure of unreacted sorbents G-72D and C7-2 and their sulfides was carried out in another study by Efthimiadis and Sotirchos (1991).

7.3. Apparatus and Procedure

Sulfidation experiments were carried out isothermally in a fixed-bed reactor system, which is shown in Fig. 7.1. The reactor was a quartz tube of 1.5 or 0.75 *cm* I.D. mounted vertically in a 3-zone furnace, which maintained a uniform temperature profile in the reactor. The sorbent was placed in the quartz tube between two zones of spherical quartz beads (1 *mm* in diameter) of about 2 *cm* in height each. The sorbent bed was supported by quartz wool placed at the bottom of the lower zone of quartz beads and at the top of the upper zone. The configuration of the reactor allowed the measurement of the reactor temperature using two thermocouples, one introduced through the upper fitting of the tube, as shown in Fig. 7.1, and the other through the fitting at its bottom. In a typical experiment, the thermocouple tips were placed outside the bed at a distance of a few *mm* from the quartz wool. However, in two runs the upper thermocouple was placed in the middle of the sorbent bed in order to measure the variation of the temperature in the sorbent bed during the reaction. The temperature difference between the indication of

this thermocouple and that at the entrance of the reactor was less than $3°C$ at all times, implying that small amounts of energy were released by the exothermic reaction at the reaction conditions of our study.

The fixed-bed reactor of Fig. 7.1 was loaded with particles of 210-250, 297-350, and 710-850 μm. The bed voidage was computed from the dimensions of the sorbent bed, the weight of the solid, and the bulk density of each sorbent (2.7 g/cm^3 for sample G-72D and 2.0 g/cm^3 for sample C7-2), the latter determined from the skeletal density and porosity of the unreacted materials. It was found that the bed voidage was approximately 40% for the two reactor tubes and for all particles sizes used in this study. This value agrees with the experimental data of Dixon (1988) on the dependence of the void fraction in fixed-beds on the particle to tube diameter ratio.

The gas distribution system involved a system of on/off and metering valves, arranged to control the flow rate and composition of the gas stream entering the reactor. The reactive gas was a mixture of 10,500 *ppm* H_2S in nitrogen, which could be further diluted with nitrogen as shown in Fig. 7.1. Standard correlations for flow through particle beds were used to estimate the pressure drop in the bed; it was found to be negligible for all particle sizes and conditions used in our studies. The gas stream leaving the reactor was divided into two streams. The first (about 90-95% of the main stream) was sent to the vent, while the second was used for gas analysis by sending it through the sampling loop of the injection system of a chromatograph. The injection system consisted of a 6-port valve attached to an electric actuator. A programmable integrator (Chromjet of Spectra Physics) was used for automatic injection and analysis of gas samples every 3 *min*. The same reactor configuration could also be used for fluidized-bed experiments. Much larger flow rates were used to fluidize the particles during such experiments. The cyclone in Fig. 7.1 was used to separate and collect the fines produced by attrition of the sorbent particles during fluidization.

The gas chromatograph was a Varian 3300 equipped with FPD and TCD detectors. The analysis was carried out isothermally at $90°C$ with helium as the carrier gas. Preliminary experiments showed that there was a linear relation between the square root of the integrated H_2S peak and the concentration of the injected samples when the H_2S content

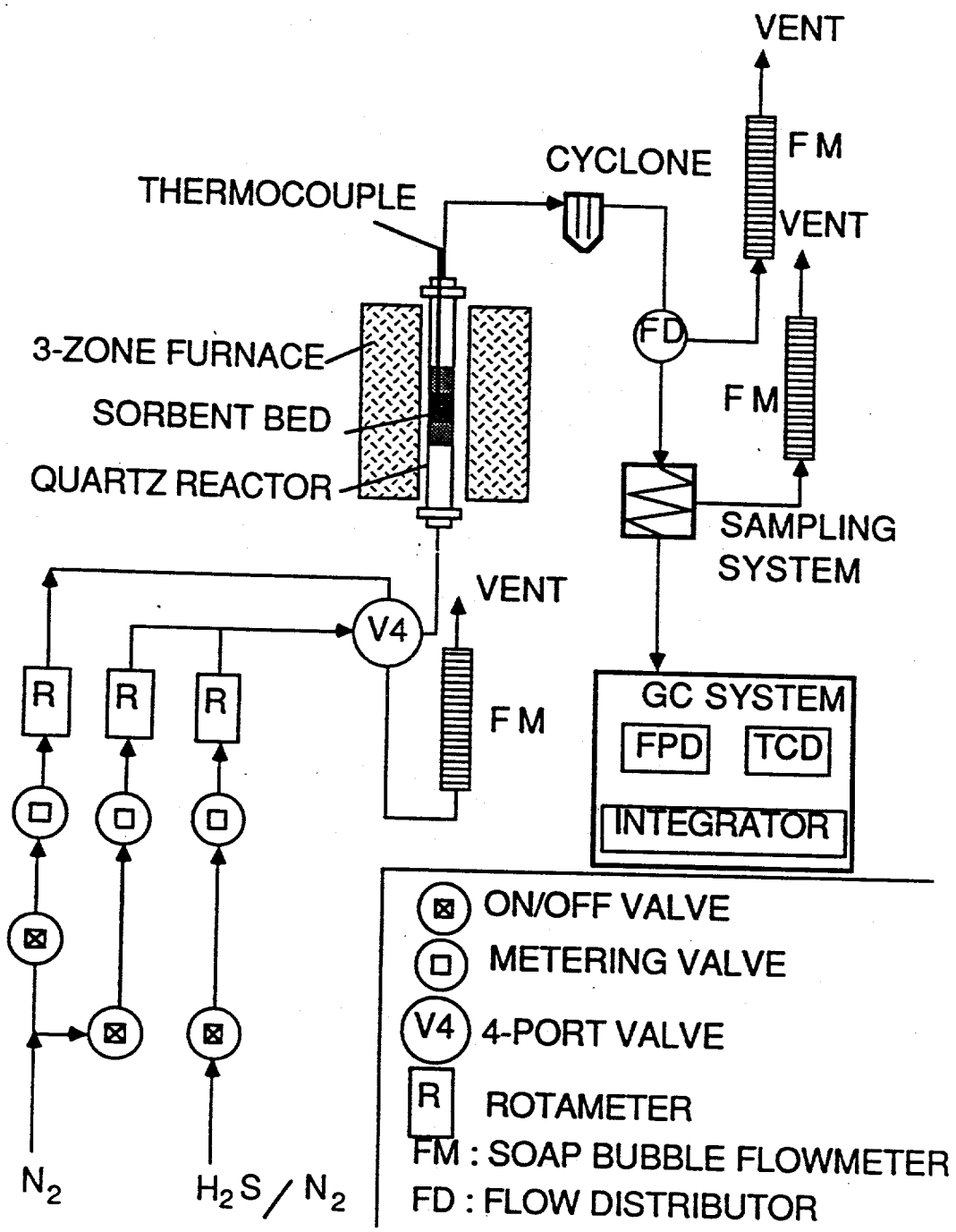

Figure 7.1: Schematic of the fixed-bed reactor and the gas analysis system.

of the stream was lower than 2,000 *ppm*. Thus, low H_2S concentrations were detected by the FPD, while higher H_2S concentrations were measured by the TCD, which could also detect nitrogen and water vapor. The weight of the sulfided sorbent was measured at the end of the experiment, and its difference from the initial sorbent weight (after the loss of the volatile compounds) was used to estimate the average conversion of the sorbent in the bed. This value was, within 1% error, in agreement with the average conversion determined from the variation of the H_2S concentration of the effluent stream of the reactor with time. Samples of reacted material were collected from different parts of the bed and were analyzed by mercury porosimetry and gas adsorption (N_2 at 77 K). A Micromeritcs Autopore II 9220 mercury porosimeter and a Quantachrome Autosorb 1 volumetric adsorption unit were used for the characterization of the samples.

7.4. Single Particle Behavior

Gas-solid reactions of the form $Solid + Gas \rightarrow Solid + \cdots$, with $\cdots$ denoting other gas species participating in the reaction, were modelled by Yu and Sotirchos (1987) in the so-called generalized random pore model. This model accounts for structural changes in the interior of the porous solid, diffusion of the gas species in the pore space and in the product layer, and chemical reaction at the interface between the unreacted and the sulfided solid. The pore space of the solid is assumed to consist of cylindrical pore segments arranged in the form of a three-dimensional lattice. The population of pores is described using the experimentally determined pore size distribution of the unreacted solid (from mercury intrusion data). The equations describing structural changes in the interior of the solid reactant with the progress of the reaction and variation of the intraparticle diffusion coefficient with the local conversion in the particle can be found in the works of Yu and Sotirchos (1987) and Zarkanitis et al. (1990).

The equations that describe diffusion of a gaseous species in a spherical porous particle and reaction with the solid are written using dimensionless quantities as follows:

$$\frac{\partial(\omega_p \epsilon_p y_p)}{\partial \tau_p} = \frac{1}{\Phi^2}\frac{1}{\rho^2}\frac{\partial}{\partial \rho}(\rho^2 \frac{\partial}{\partial \rho}(\delta^e y_p)) - \nu_A \kappa_v y_p \tag{7.1}$$

$$\frac{\partial \xi}{\partial \tau_p} = \frac{1}{(1-\epsilon_0)}\kappa_v y_p \tag{7.2}$$

y_p is the concentration of the reactive gas, ρ is the radial distance in the particle, δ^e is the effective diffusivity, κ_v is the volume-based reaction rate constant, ε_0 and ε_p are the porosities of the unreacted and reacted particle, respectively, ξ is the local conversion of the particle, ν_A is the stoichiometric coefficient of the reactive gas, and τ_p is the time. Eqs. 7.1 and 7.2 are written for a first-order reaction with respect to the gaseous reactant, since this was found to be the case for the reaction of sorbents G-72D and C7-2 with H_2S in our previous studies (Efthimiadis and Sotirchos, 1991). The boundary and initial conditions for Eqs. 7.1 and 7.2 are:

$$\frac{\partial y_p}{\partial \rho} = 0|_{\rho=0};\ \frac{Sh^e}{\delta^e}(1-y_p) = \frac{\partial y_p}{\partial \rho}|_{\rho=1} \qquad (7.3a,b)$$

$$y_p = 0 \text{ and } \xi = 0 \text{ at } \tau_p = 0 \qquad (7.4a,b)$$

The dimensionless quantities shown in Eqs. 7.1-7.4 are defined by the equations:

$$\rho = \frac{r}{a};\ y_p = \frac{c_p}{c_b};\ \delta^e = \frac{D^e}{D_0^e};\ \kappa_v = \frac{k_v}{k_{v0}};\ \omega_p = v_s c_b; \qquad (7.5a-e)$$

$$\tau_p = v_s k_s S_0 \int_0^t c_b dt';\ \Phi^2 = a^2 \frac{k_s S_0}{D_0^e};\ Sh^e = \frac{k_g a}{D_0^e} \qquad (7.6a-c)$$

The symbols used in Eqs. 7.5 and 7.6 are explained in the notation section of this paper.

Experimental data obtained during the sulfidation of G-72D and C7-2 particles of 53-350 μm were used in previous studies (Efthimiadis and Sotirchos, 1991) to test the applicability of the generalized random pore model to zinc oxide sulfidation. Excellent agreement was found to exist between model predictions and experiment. However, in some of the fixed-bed experiments, the C7-2 particles were larger than those used in our previous sulfidation studies. Therefore, additional sulfidation experiments were performed in the thermogravimetric analysis system using particles of 600-710 and 710-850 μm. C7-2 samples of about 3 mg were reacted with 0.5% H_2S diluted in nitrogen at 200 ml/min flow rate (at standard conditions). Details about the TGA reactor are given elsewhere (Efthimiadis and Sotirchos, 1991). The TGA experimental data were successfully reproduced by the generalized pore model without using any adjustable parameters since the two parameters needed for the application of the mathematical model (diffusion coefficient

in the product layer and coordination number of the pore network (i.e., average number of pores per node)) had been determined in previous studies (Efthimiadis and Sotirchos, 1991) by fitting the model predictions to the experimental data for particles in the size range 53-350 μm. Experimental and predicted conversion vs. time curves for sulfidation at $600°C$ of C7-2 particles in the size range 210-850 μm are shown in Fig. 7.2.

In the sulfidation of ZnO sorbents, as well as in most gas-solid reactions, the time associated with structural changes in the interior of the particles is much larger than the time associated with the establishment of the steady state profile of the reactive gas concentration in the particles (pseudosteady-state approximation). As a result, the transient term in Eq. 7.1 can be set equal to zero. The average reaction rate per unit of particle volume, $\bar{R}_v$, is then related to the concentration of H_2S in the surrounding gas phase (i.e., in the bed) by the equation:

$$\bar{R}_v = \bar{k}_v(\bar{\xi})c_b \tag{7.7}$$

The average conversion of a particle ($\bar{\xi}$) and the average volumetric reaction rate constant in a particle ($\bar{k}_v(\bar{\xi})$) can be computed from the local conversion (ξ) and reaction rate constant ($k_v(\xi)$) using the equations:

$$\bar{\xi} = \int_0^1 \xi \; d\rho^3 \tag{7.8}$$

$$\bar{k}_v(\bar{\xi}) = \int_0^1 k_v(\xi) y_p \; d\rho^3 \tag{7.9}$$

Shown in Fig. 7.3 is the variation of the volumetric reaction rate constants with the conversion at $600°C$ for various particle sizes of the two sorbents used in our experiments. The evolution of the average volumetric reaction rate with the average conversion in particles sulfided at $500°C$ was similar to that of Fig. 7.3. The volumetric reaction rate constants in Fig. 7.3 were normalized with respect to the initial volumetric reaction rate constant in the absence of intraparticle diffusional limitations ($k_{v0} = k_s S_0$). Therefore, the initial value of $\bar{k}_v(\bar{\xi})/k_{v0}$ is equal to the initial effectiveness factor, and as a result, in the absence of initial intraparticle diffusional limitations it should be unity. Increasing the

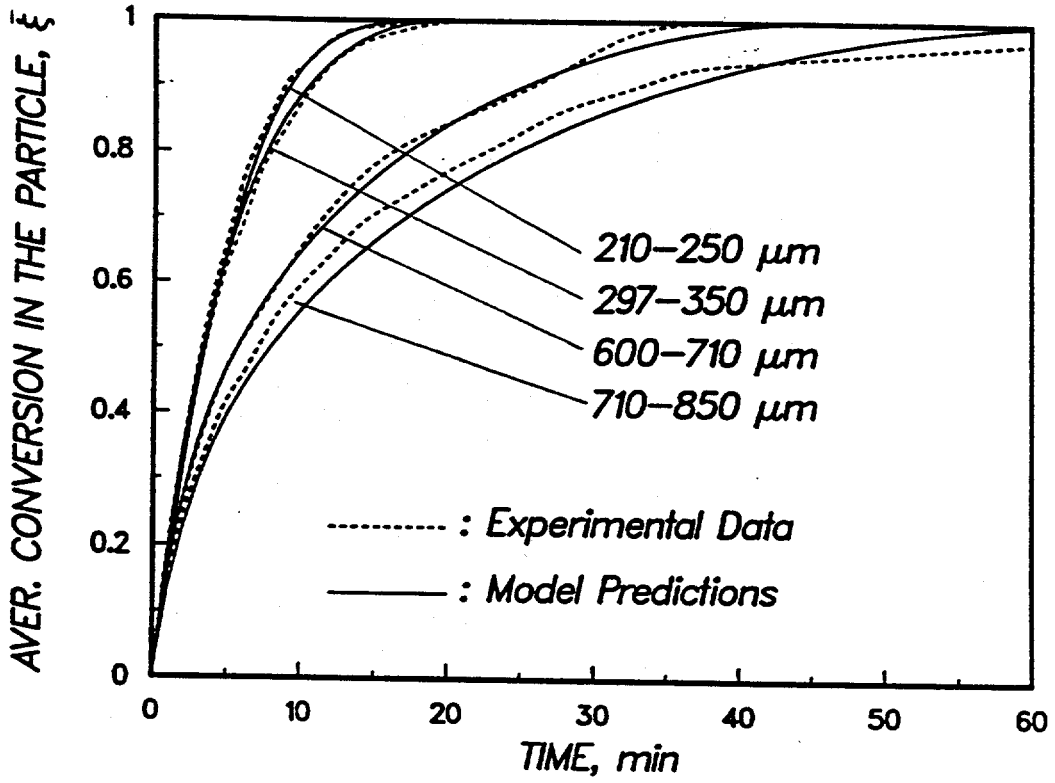

Figure 7.2: Comparison of the reactivity data obtained in a differential reactor at $600°C$ with the mathematical model predictions.

particle size intensifies the intraparticle diffusional limitations and leads to lower average reaction rate for the same average conversion in the particle. According to the results of Fig. 7.3, the average reactivity of sorbent G-72D not only is lower than that of sorbent C7-2 (same size particles) but decreases faster with the conversion as well. As the results of Table 7.1 show, sample G-72D has less pore volume per unit mass and smaller most probable radius than sample C7-2. Moreover, it was found from the analysis of the single particle sulfidation data that the effective diffusivity of H_2S in its pore space is smaller and decreases faster with the conversion than that in sample C7-2 (Efthimiadis and Sotirchos, 1991).

7.5. Mathematical Model for a Fixed-Bed Reactor

The development of a mathematical model for a fixed-bed reactor is facilitated greatly by assuming that the concentration in the bed changes negligibly within a distance equal to the particle or pellet size. The average local reaction rate and conversion at any point in the bed are then equal to the average reaction rate and conversion of a particle, which experiences ambient conditions identical to those at the same point of the bed. The average local reaction rate and conversion in the bed are given by Eqs. 7.8 and 7.9, and as a result, it is necessary to solve the structural and particle model equations at every point in the bed in order to determine their values. For a first-order reaction – as it is the case here – it is not necessary to solve these two models simultaneously with the bed equations if the pseudosteady-state approximation is used for diffusion in the product layer and diffusion and reaction in the pore space. The structural model is solved first to create a database for the particle problem, which is then solved to create a database (for the variation of $\bar{k}_v$ with $\bar{\xi}$) for the bed model. This approach was used by Sotirchos and Zarkanitis (1989) in their fixed-bed desulfurization model.

The equations that describe the material balances of the gas and the solid reactant are in dimensionless form:

$$\varepsilon_b \frac{\partial y}{\partial \tau} = \frac{\partial^2 y}{\partial x^2} - Pe \frac{\partial y}{\partial x} - \bar{\Phi}^2(\bar{\xi}) y \tag{7.10}$$

$$\frac{\partial \bar{\xi}}{\partial \tau} = \omega \bar{\Phi}^2(\bar{\xi}) y \tag{7.11}$$

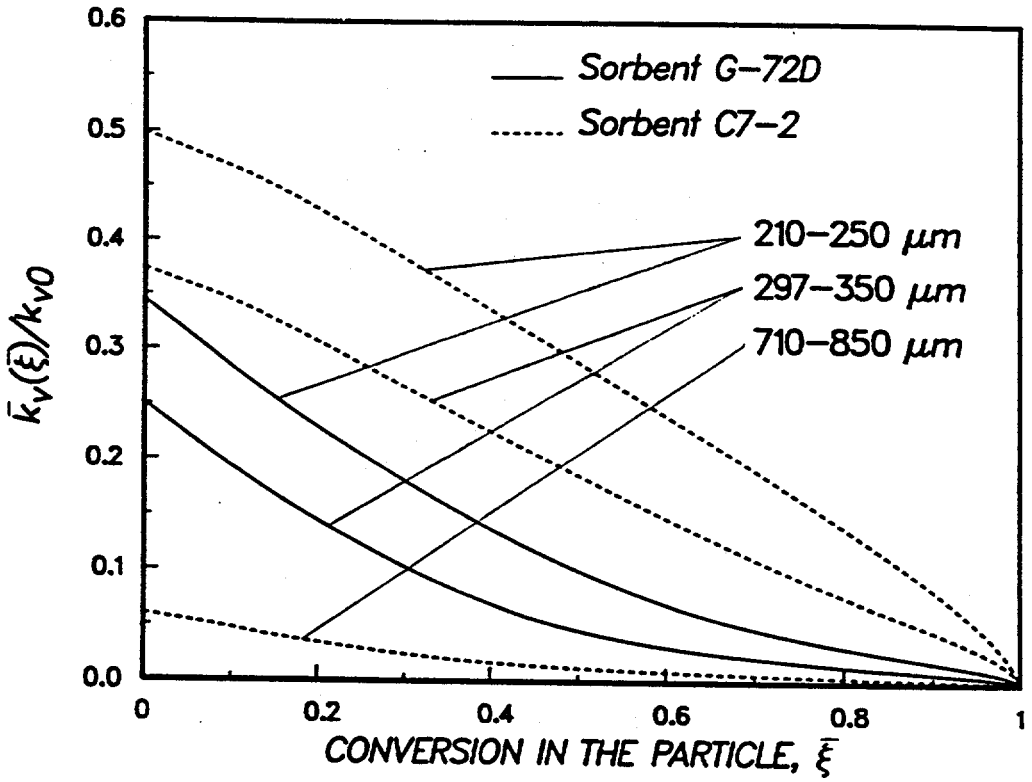

Figure 7.3: Evolution of the average volumetric reaction rate constant with the average conversion in various particle sizes at $600°C$.

where

$$y = \frac{c}{c_0}; \quad x = \frac{z}{L}; \quad Pe = \frac{uL}{D_b} \tag{7.12a,b,c}$$

$$\tau = \frac{tD_b}{L^2}; \quad \bar{\Phi}^2(\bar{\xi}) = \frac{(1-\varepsilon_b)L^2\bar{k}_v(\bar{\xi})}{D_b}; \quad \omega = \frac{v_s c_0}{(1-\varepsilon_0)(1-\varepsilon_b)} \tag{7.13a,b,c}$$

y is the concentration of the reactive gas in the bed, x is the axial distance in the bed, ε_b is the bed voidage, $\bar{k}_v(\bar{\xi})$ is the volumetric reaction rate, Pe is the Peclet number, and τ the reaction time. The symbols in Eqs. 7.12 and 7.13 are given in the notation section of this paper. The boundary and initial conditions used for Eqs. 7.10 and 7.11 are:

$$-\frac{\partial y}{\partial x} = Pe(1-y) \quad \text{at } x = 0 \tag{7.14}$$

$$\frac{\partial y}{\partial x} = 0 \quad \text{at } x = 1 \tag{7.15}$$

$$y = 0 \text{ and } \bar{\xi} = 0 \quad \text{at } \tau = 0 \tag{7.16a,b}$$

The numerical procedure followed for the solution of the above equations is described in detail by Sotirchos and Zarkanitis (1989).

Before we proceed with the presentation of the model predictions, we will briefly discuss some of the assumptions made in the development of the mathematical model for the bed. No energy balance was included in the bed model since the reactor was assumed to operate isothermally. As mentioned previously, the temperature rise in the bed was too small (less than 3^oC) to justify use of a nonisothermal model. It is assumed that the bed voidage (ε_b) remains constant during the sulfidation reaction. Even though the solid product occupies more space than the solid reactant, this assumption is not unreasonable because reaction mainly occurs in the interior of the porous particles. The ratio of the internal surface area of the solids to the geometrical external surface area is about 4,000 for particles of 200 μm and larger for the other particle sizes used in this work. The axial dispersion coefficient, D_b, was estimated from the formula $D_b = \varepsilon_b \mathcal{D}/\eta$ for $\eta = 2$. $\mathcal{D}$ is the binary diffusion coefficient of H_2S in N_2, and η is the tortuosity factor of the bed. We chose to work with this value of axial dispersion coefficients on the basis of the pulse chromatographic studies of Krishnan and Sotirchos (1990) for beds packed with zinc oxide particles of the same sizes as the ones used in our experiments.

The predictions of the mathematical model were found to be strongly influenced by the type of sorbent, size of sorbent particles, and residence time of reactive mixture in the sorbent bed. Fig. 7.4 presents simulation results for the reaction of 210-250 and 297-350 μm particles of samples G-72D and C7-2 with a mixture of 10,500 ppm H_2S in nitrogen at 600^oC. The reaction times were normalized with respect to the minimum time required for complete conversion of the bed (t_0). The space velocity for all the cases of Fig. 7.4 was 20,000 hr^{-1} (based on the volume of empty bed at standard conditions), and the reactor diameter and length were 0.75 and 3.40 cm, respectively. For small H_2S concentration in the exit stream, t/t_0 gives a direct measure of sorbent utilization (sorbent used/initial bed load) in the bed. According to the results of Fig. 7.4, the sorbent utilization decreases with increasing particle size for a given breakthrough concentration. Moreover, it takes less time to get a certain concentration at the exit of the reactor when the reactor is loaded with G-72D particles.

The conversion profiles in the reactor for the four cases of Fig. 7.4 are shown in Fig. 7.5 at reaction times 0.3, 0.6, and 0.9 (t/t_0). Because of the high value of space velocity used to obtain the results of Fig. 7.4, the contribution of the axial dispersion term in the mass balance in the bed is negligibly small. As a result, with the exception of the early stages of the reaction, the concentration profiles in the bed are identical to those of Fig. 7.5. The behavior of the results of Figs. 7.4 and 7.5 for the breakthrough curves are in agreement with those of Fig. 7.3 for the variation of the volumetric reaction rate constant. (The k_{v0} values for the two sorbents do not differ significantly.) The sorbent utilization for a certain breakthrough concentration varies in the same order as the average reactivity of the particles, and the spread of the conversion profile in the bed increases with decreasing particle reactivity.

The performance of a sorbent bed loaded with 297-350 μm particles at 600^oC, under different reactive gas flow rates corresponding to space velocities (S.V.) of 20,000, 10,000, and 2,000 hr^{-1} (at standard conditions) is examined in Fig. 7.6. The dimensions of the sorbent bed are the same as those in Fig. 7.4. Large residence times (small reactive gas flow rates) tend to reduce the spread of the conversion profile in the reactor and, hence, increase the utilization of the sorbent at the breakthrough point. Obviously, there is a

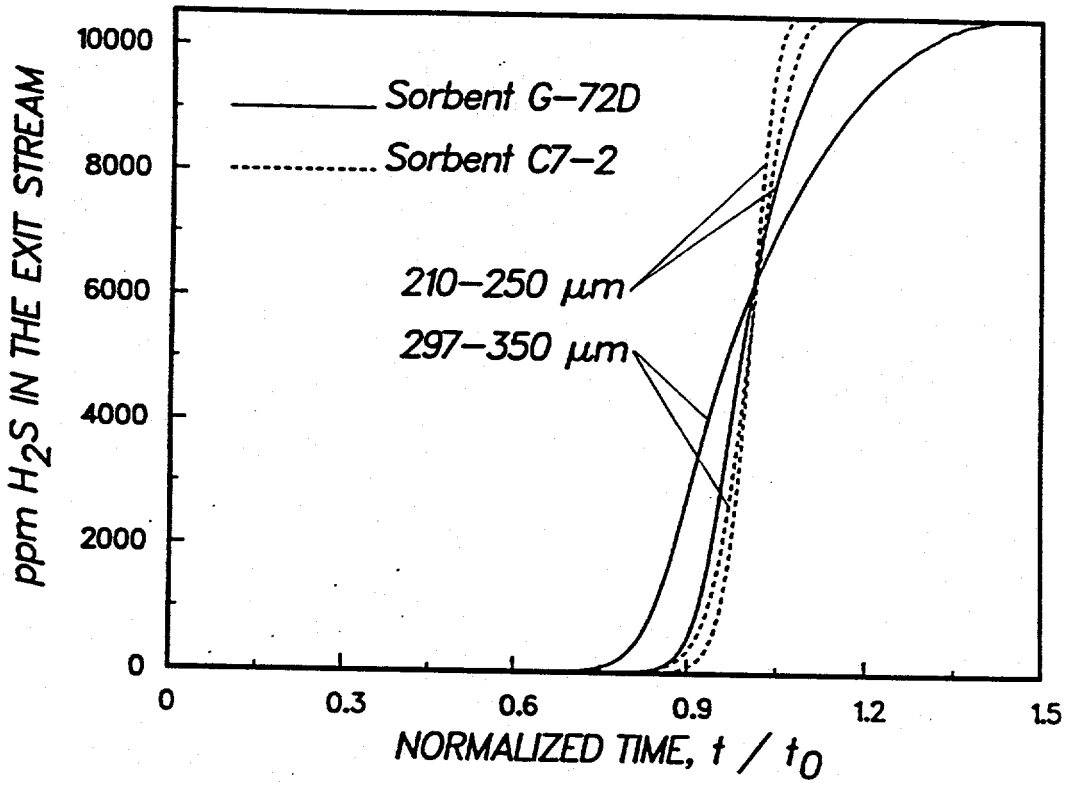

Figure 7.4: Breakthrough curves predicted by the mathematical model for sulfidation at $600°C$ of sorbent beds loaded with zinc oxide particles.

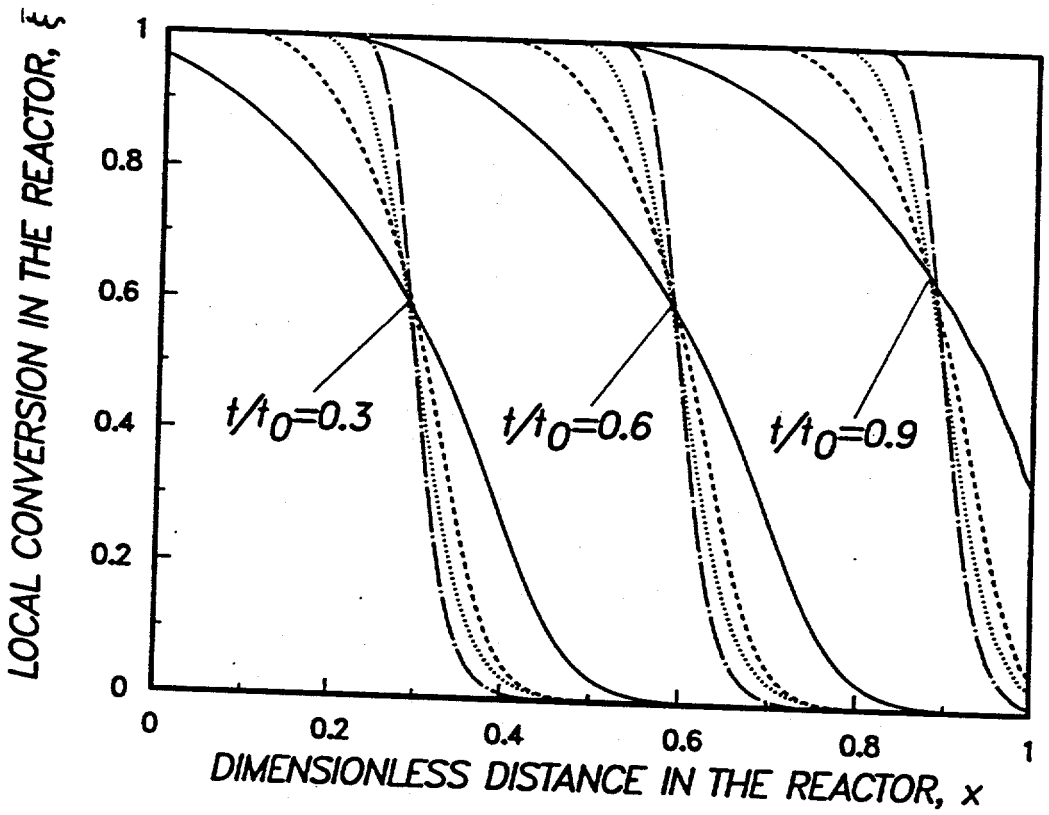

Figure 7.5: Conversion profiles in the sorbent bed at different reaction times for the cases presented in Fig. 7.4. ———: G-72D, 297-350 μm; – – –: G-72D, 210-250 μm; ·····: C7-2, 297-350 μm; – · –: C7-2, 210-250 μm.

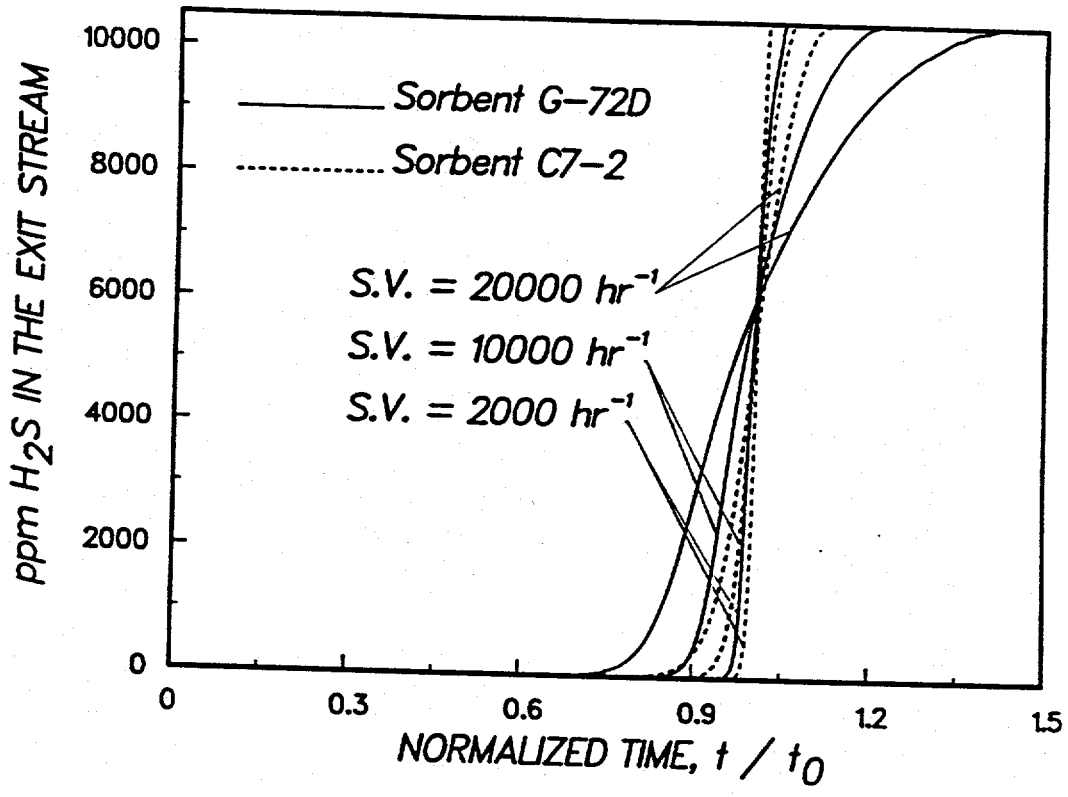

Figure 7.6: Effect of the space velocity (S.V.) of the reactive gas on the model predictions for sulfidation of 297-350 μm particles at $600°C$.

trade-off between gas throughput in the reactor and sorbent utilization. Therefore, the conditions for optimal operation depend not only on the sorbent but on the economics of the overall process (sulfidation and regeneration) as well.

7.6. Sulfidation Experiments in a Fixed-Bed Reactor and Model Predictions

In this section, we present and discuss the breakthrough curves that were measured in our experiments and compare them with the predictions of the mathematical model. The application of the model involves no unknown parameters. The parameters of the sorbent bed (particle diameter, weight of the unreacted solid, and bed length and radius) and the operating conditions (temperature and reactive gas flow rate and composition) are directly measured. On the other hand, the parameters for the particle model (diffusion, reaction, and structure evolution equations) – which are needed to determine $\bar{k}_v(\bar{\xi})$ (using Eqs. 7.8 and 7.9) – are found from the analysis of the single-particle TGA reactivity data. Table 7.2 summarizes the reaction conditions for the various fixed-bed experiments discussed in this section. The reactive mixture was 1.05% H_2S in N_2 for all experiments, with the exception of run FB209, where a mixture containing 0.509% H_2S was used.

It should be pointed out that in addition to the particle sizes listed in Table 7.2, experiments were also carried out with 53-62 and 88-105 μm particles under various reaction conditions. It was observed that particles in these size ranges tended to agglomerate in the fixed-bed reactor, leading to significant pressure drop in the reactor. Problems of this kind were not encountered in beds loaded with particles larger than 200 μm.

No H_2S was detected by the FPD (flame photometric detector) before the breakthrough point in all our experiments, implying that the H_2S concentration in the exit stream of the reactor was below the detection limit of the detector (about 1 ppm). The equilibrium concentration for the reaction of ZnO with 10,500 ppm H_2S in nitrogen at 500 and 600^oC was calculated using thermodynamic data from Barin and Knacke (1973). In accordance to our gas analysis measurements, lower H_2S concentrations than our detection limit (for example, 0.4 ppm at 600^oC) were estimated from the thermodynamic calculations.

Run	Sorbent	Particle Size (μm)	Reactor I.D. (cm)	Reactor Length (cm)	Temp. (^oC)	Space Vel. (hr^{-1})
FB107	G-72D	297-350	0.75	2.8	500	5120
FB105	C7-2	297-350	0.75	2.8	500	4920
FB104	G-72D	297-350	0.75	2.5	600	5395
FB101	C7-2	297-350	0.75	2.8	600	4880
FB102	C7-2	210-250	0.75	2.8	600	4790
FB209	G-72D	210-250	1.5	2.5	600	14620
FB108	G-72D	297-350	0.75	2.5	600	1995
FB106	C7-2	297-350	0.75	2.5	600	2070
FB212	G-72D	297-350	1.5	5.4	600	1850
FB211	C7-2	297-350	1.5	2.5	600	16120
FB301	C7-2	710-850	1.5	9.4	600	3050
FB302	C7-2	710-850	1.5	8.7	600	3320

Table 7.2: Reaction conditions used in the sulfidation experiments.

The experimental and the theoretical results of Fig. 7.7 give breakthrough curves for samples G-72D and C7-2 at 500 and 600^oC. The experimental data (the H_2S concentrations measured by GC analysis) are given by distinct points, while the model predictions are presented as continuous curves. (The results will be presented in the same way in all the other figures we will discuss in this section.) The experiments of Fig. 7.7 were performed using particles of 297-350 μm and space velocities of about 5,000 hr^{-1}. Very good agreement, both qualitative and quantitative, appears to exist between model and experiment in Fig. 7.7. This was found to true for all cases considered in our study, a remarkable result considering that all model parameters were determined from independent experiments. Relatively large deviations between the theoretical and experimental results were observed only for small breakthrough concentrations, i.e., in the vicinity of the 'elbow' of the breakthrough curve. Even if the data for small concentrations were as reliable as those

for large concentrations, this behavior should not surprise us. The sulfidation of zinc oxide is a reversible reaction, and it is thus possible its actual kinetics for small concentration values to be much different from the irreversible, linear kinetics used in the mathematical model.

The results of Fig. 7.7 indicate that the reaction temperature has almost no effect on the experimental and theoretical data. This is in agreement with the weak effect of desulfurization temperature on the behavior of single C7-2 and G-72D particles that we observed in our TGA studies (Efthimiadis and Sotirchos, 1991). Weak influence of desulfurization temperature on the experimental data was also seen in fixed-bed experiments of other desulfurization studies such as the study of Yumura and Furimsky (1985) with zinc oxide sorbents and Gangwal et al. (1989) with zinc ferrite sorbents. We did not cover a larger temperature range in our experiments, because at temperatures higher than 600^oC we may have sintering and zinc loss (above 650^oC according to Tamhankar et al. (1986) and Gangwal et al. (1989)), whereas at temperatures below 500^oC reactivity results may be corrupted by sulfur chemisorption in the sorbents (Efthimiadis and Sotirchos, 1991).

Since the residence time of the reactive mixture in the sorbent bed has strong effects on sorbent utilization (Fig. 7.6), experiments were carried out in the fixed-bed reactor of Fig. 7.1 over a broad range of space velocities (about 2,000-15,000 hr^{-1}). The experimental data and the model predictions for a bed loaded with particles of the G-72D sample and sulfided at 600^oC are shown in Fig. 7.8. Particles of 210-250 μm size were used in the FB209 run, while in all the other runs the reactor was loaded with 297-350 μm particles. The dependence of the breakthrough response of the fixed-bed desulfurization reactor on particle size and space velocity may also be seen in Fig. 7.9 for beds loaded with sample C7-2, but for a much broader range of particle size than for sample G-72D (Fig. 7.8). In agreement with the theoretical predictions of Figs. 7.4 and 7.6, the results of Figs. 7.8 and 7.9 show that an increase in the particle size or in space velocity increases the spread of the breakthrough curve and leads to lower sorbent utilization. It is interesting to note that a combination of smaller particle size and higher space velocity in run FB209 relative to the values used in run FB104 produces a breakthrough curve similar to that obtained in the latter case. The H_2S concentration used in run FB209 is half the value used in all

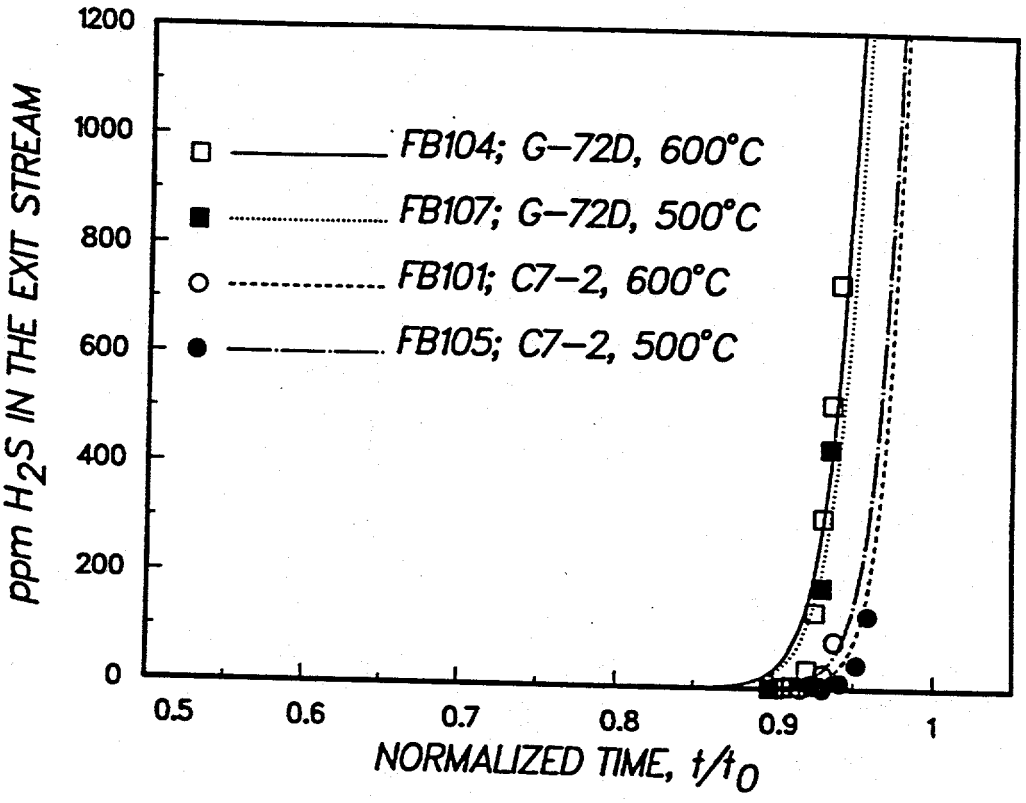

Figure 7.7: Comparison of the experimental data with the model predictions at different reaction temperatures.

other experiments but since the reaction is of first order with respect to the concentration of H_2S, results for different H_2S concentration can be compared with each other. Direct inspection of the fixed-bed model equations (Eqs. 7.10-7.16) reveals that the breakthrough curve expressed as y vs. t/t_0 is independent of the H_2S concentration at the inlet of the reactor.

It is clear from the comparison of model predictions and experimental data in Figs. 7.7-7.9 that the mathematical model successfully predicts the behavior of fixed-bed reactors loaded initially with fresh (unreacted) particles. In order to examine the ability of the model to describe the behavior of a fixed-bed reactor when desulfurization starts with a nonuniform conversion profile in the bed, we carried out experiments using beds loaded with partially reacted sorbents. Specifically, we stopped the reaction in runs FB301 and FB302 after significant H_2S concentration was detected at the outlet of the reactor (a few hundred *ppm*, as it can be seen in Fig. 7.9 for run FB302) by passing N_2 through the reactor. We then reversed the direction of flow in the bed and continued the sulfidation process under the reaction conditions used in the first step of the experiment. The experimental results obtained from these experiments are shown in Fig. 7.10, with the solid markers used for the concentrations measured during the first step of the experiments. In presenting the results, the start time for the second part of the experiments was set equal to the actual time when the first sulfidation step was stopped, t^* (τ^* in dimensionless form). The model predictions of Fig. 7.10 given by solid curves are for the first step of the experiments and were obtained by integrating the fixed-bed model equations with the initial conditions given by Eqs. 7.16a,b. The dashed curves give the model predictions for the second part of the experiment and were obtained by integrating the model equations with initial conditions:

$$y = 0 \text{ and } \bar{\xi} = \bar{\xi}^*(x) \quad \text{at } \tau = \tau^* \qquad (7.16'a,b)$$

with $\bar{\xi}^*(x)$ being the concentration profile in the inverted bed at the end of the first part of the experiment, i.e., $\bar{\xi}^*(x) = \bar{\xi}(1-x, \tau^*)$. Good agreement is again observed to exist between model predictions and experimental results, especially in the most important part of the breakthrough curve, namely, that corresponding to low H_2S concentration in the outlet stream. The tendency of the mathematical model to predict sharper breakthrough

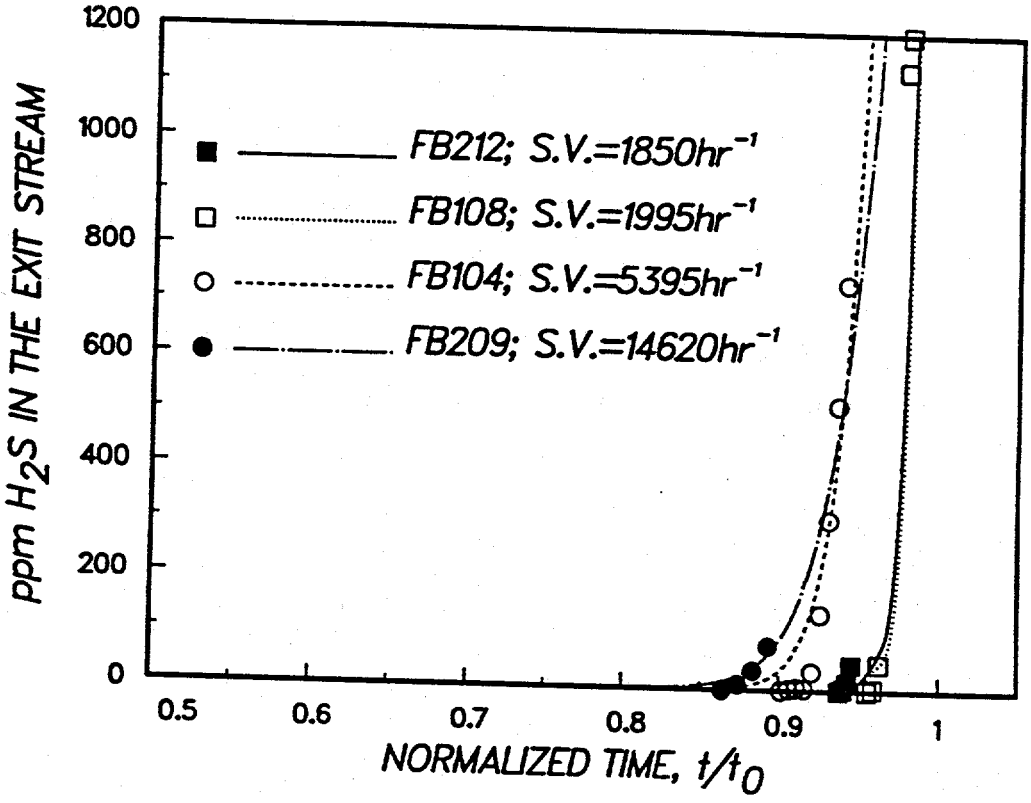

Figure 7.8: Experimental data and model predictions for sulfidation of the G-72D sample at $600°C$.

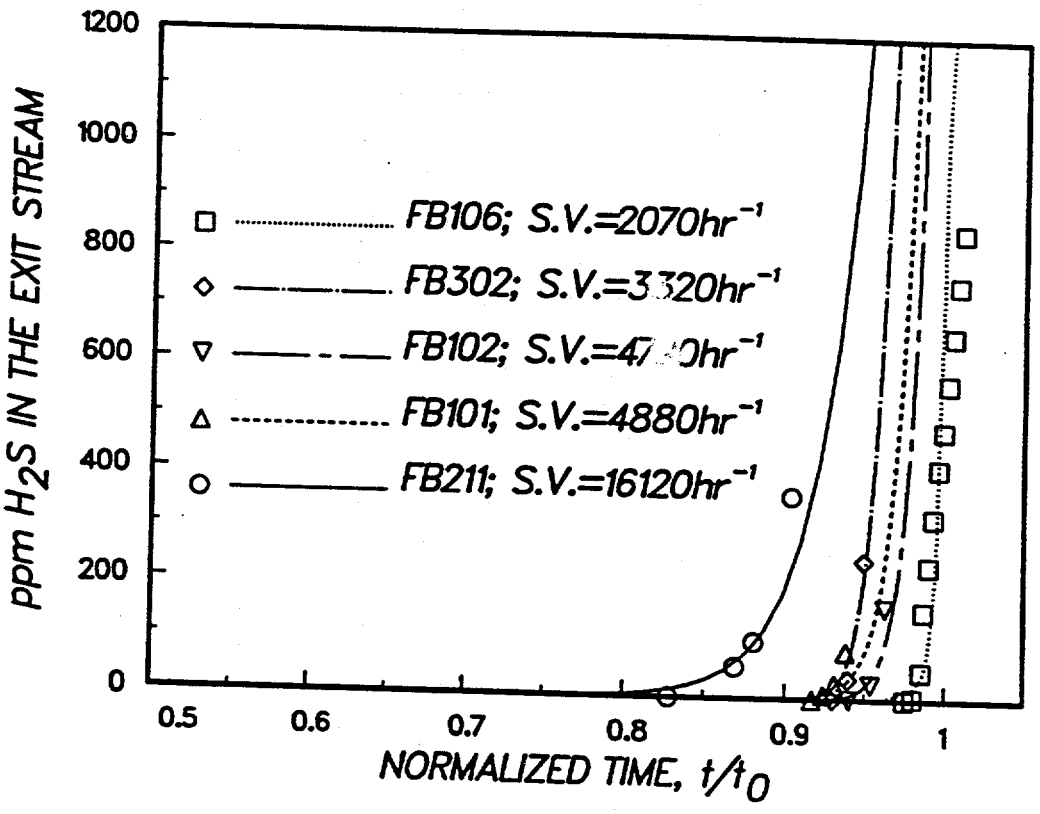

Figure 7.9: Experimental data and model predictions for sulfidation of the C7-2 sample at $600°C$.

curves in the high concentration region and, hence, faster completion of the reaction is due to overprediction of the reaction rate at high conversions by the particle model (see Fig. 7.2).

7.7. Analysis of the Pore Structure of the Sulfided Sorbents

The pore structure of the sulfided sorbents was characterized using mercury porosimetry and nitrogen adsorption at $77K$. Samples of reacted particles were collected from the top, bottom, and middle section of the bed. N_2 pycnometry measurements, made in the adsorption unit were used to estimate the skeletal densities of the unreacted and fully sulfided solids. Heat-treated samples of samples G-72D and C7-2 had skeletal densities of 5.4 and 4.8 g/cm^3, respectively. Lower densities were measured for the sulfided forms of the two sorbents (4 and 3.8 g/cm^3 for sorbents G-72D and C7-2, respectively).

The pore volumes of the fully sulfided sorbents agreed well with those predicted from the porosities and compositions of the unreacted (heat-treated) samples under the assumption that there was no change in the overall dimensions of the particles during the reaction. This finding was used to determine the average conversion of the partially reacted samples using the pore volumes obtained from the mercury porosimetry data. The average conversion $\hat{\xi}$ of a sample collected between points x_1 and x_2 in the bed is obviously equal to

$$\hat{\xi} = \frac{1}{x_2 - x_1} \int_{x_1}^{x_2} \bar{\xi} dx \tag{7.17}$$

$\hat{\xi}$ is related to the average porosity $\hat{\varepsilon}$ of the sample by the equation:

$$\hat{\xi} = \frac{\varepsilon_0 - \hat{\varepsilon}}{(1 - \varepsilon_0)(Z - 1)} \tag{7.18}$$

where Z is the volume of fully reacted solid phase per unit volume of unreacted solid phase. Z is equal to 1.56 and 1.38 for samples G-72D and C7-2, respectively. The average conversion for the partially reacted samples that were collected from the top, middle, and bottom parts of the bed are shown by dashed straight lines in Figs. 7.11 and 7.12 for samples G-72D (run FB209) and C7-2 (run FB211). Each dashed line extends over the portion of the bed, in terms of distance, that each average conversion represents. The continuous solid curves give the conversion profile predicted by the mathematical model at

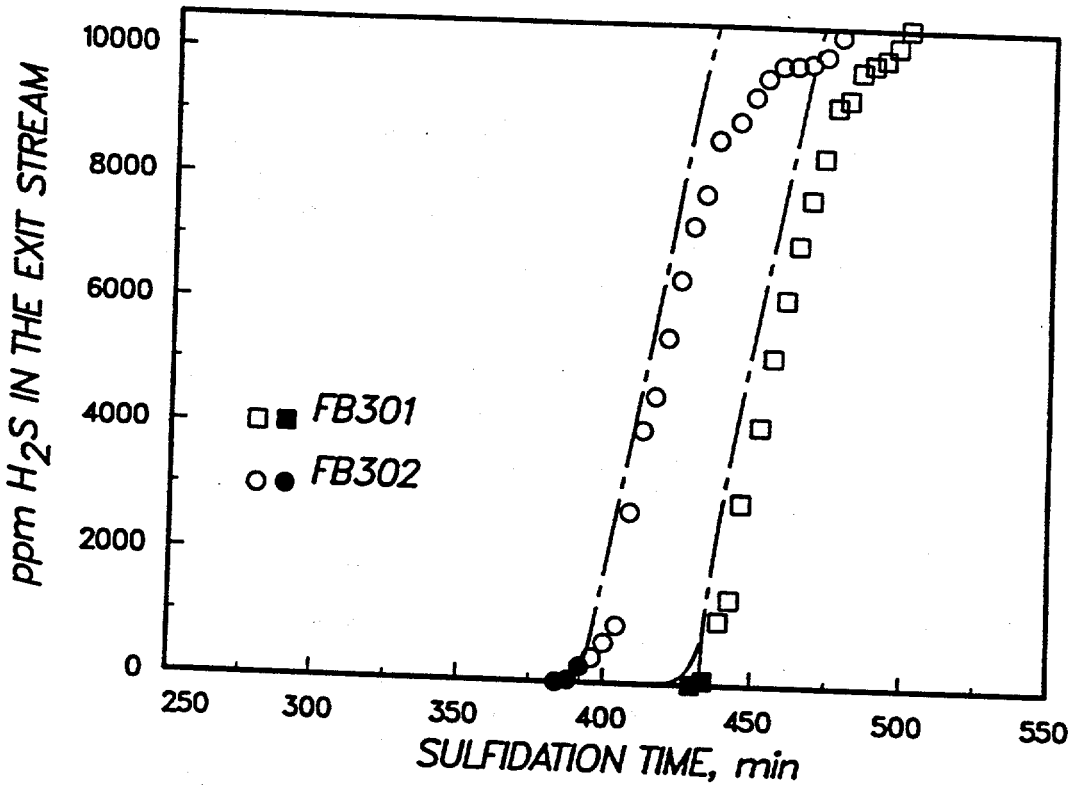

Figure 7.10: Comparison of the model predictions with the experimental data of two sulfidation runs at $600°C$.

the time the sulfidation reaction was stopped. We see that in both figures the experimental average conversion histogram is in very good agreement with the theoretical conversion profile.

The cumulative pore volume vs. pore diameter curves for the partially reacted samples of Figs. 7.11 and 7.12, determined from mercury intrusion porosimetry data, are given in Figs. 7.13 and 7.14, respectively. Shown in the figures are also the pore volume distribution curves for the unreacted sorbent (solid curves). The results of Figs. 7.13 and 7.14 show that the total pore volume decreases with increasing conversion, while the most probable pore radius of the pore volume distributions shifts toward larger pore sizes. The decrease in the total pore volume is expected since the reaction involves a solid product (ZnS) which occupies more space than the oxide from which it results. This cannot be said, however, about the displacement of the pore size distribution toward large pores. If the pore structure of the sorbents evolves only because of the reaction of H_2S with ZnO, the size of each pore should become progressively smaller as ZnO is replaced by ZnS and the pore volume distribution should move toward smaller pores. Shift of the pore size distribution toward larger pores was also observed by Grindley (1988), who performed mercury porosimetry measurements on sulfided and regenerated zinc ferrite pellets in a fixed-bed reactor.

The behavior of the pore volume distribution curves of Figs. 7.13 and 7.14 is in disagreement with the results we obtained in another study (Efthimiadis and Sotirchos, 1991) on the evolution with the conversion of the pore volume distribution of partially reacted samples of the same sorbents prepared in a fluidized-bed reactor. Pore volume distribution curves for partially reacted and fully sulfided samples of sorbent C7-2 from that study are shown in Fig. 7.15. These samples were prepared using the experimental arrangement of Fig. 7.1 with the fixed-bed replaced by a fluidized-bed reactor. Specifically, about 5 g of 710-850 μm particles were sulfided up to four different conversion levels using 1.05% H_2S in N_2 flowing at 3.5 l/min (standard temperature and pressure). The pore volume distribution of the unreacted sorbent and of the fully sulfided sorbent in the fixed-bed reactor (see Fig. 7.14) are also shown in Fig. 7.15 for comparison. As the results of Fig. 7.15 show there is no shift of the pore volume distribution of the samples prepared in

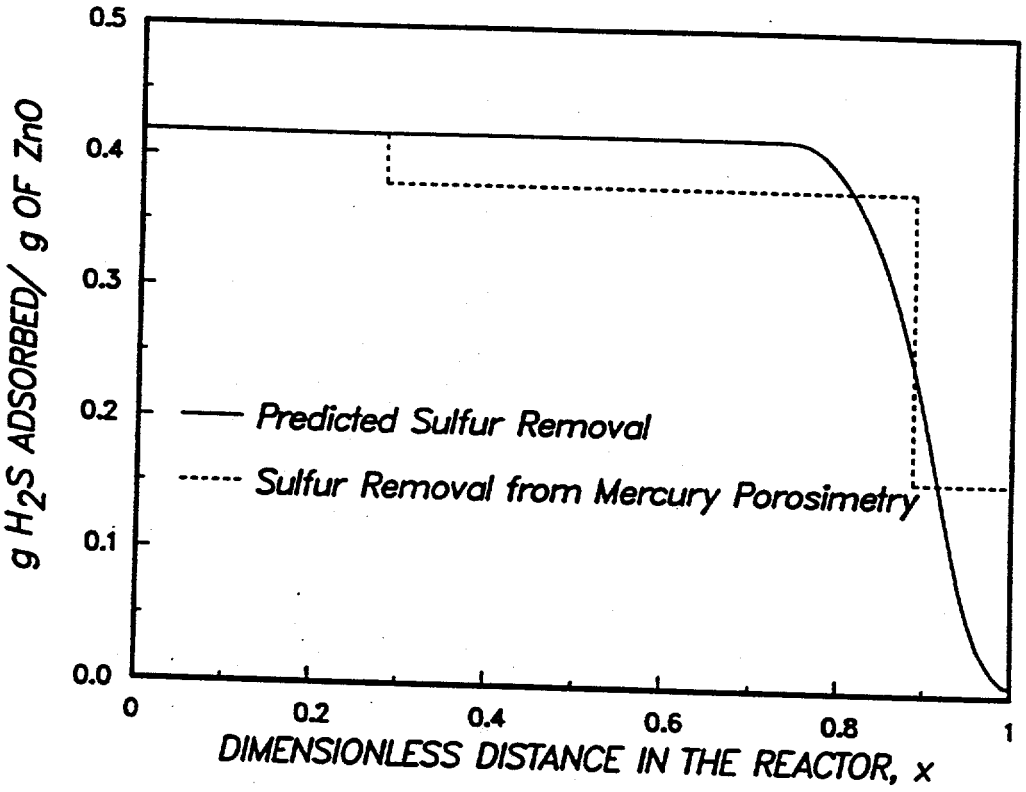

Figure 7.11: Comparison of the predicted by the mathematical model conversion profile in the sorbent bed of the FB209 run (sample G-72D) and the experimentally determined average conversion of segments of the sorbent bed.

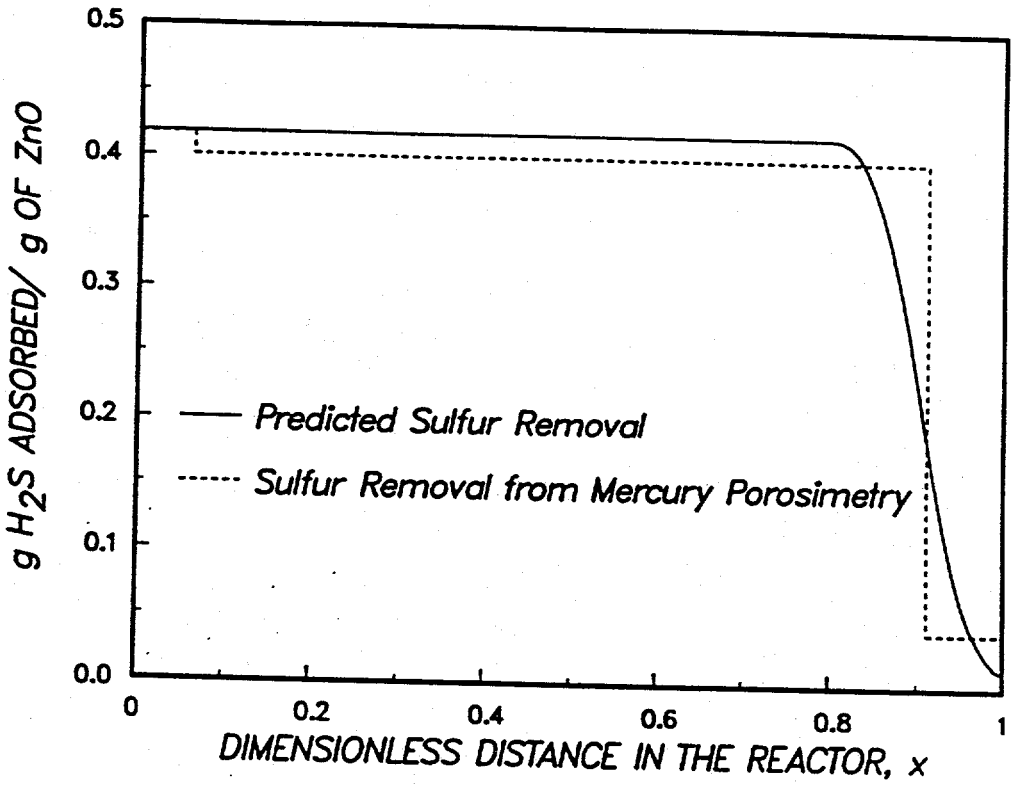

Figure 7.12: Comparison of the predicted by the mathematical model conversion profile in the sorbent bed of the FB211 run (sample C7-2) and the experimentally determined average conversion of segments of the sorbent bed.

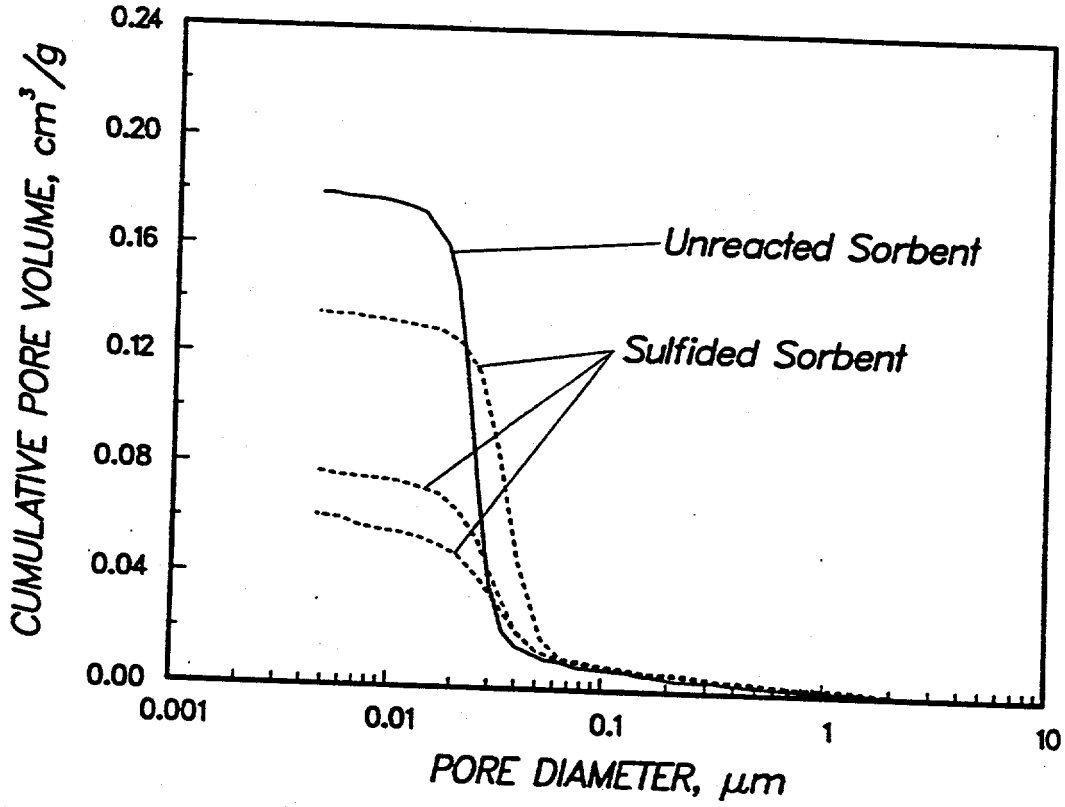

Figure 7.13: Porosimetric cumulative pore volume vs. pore diameter curves of unreacted G-72D sorbent and those of solid samples collected from the top, middle, and bottom of the sorbent bed of run FB209.

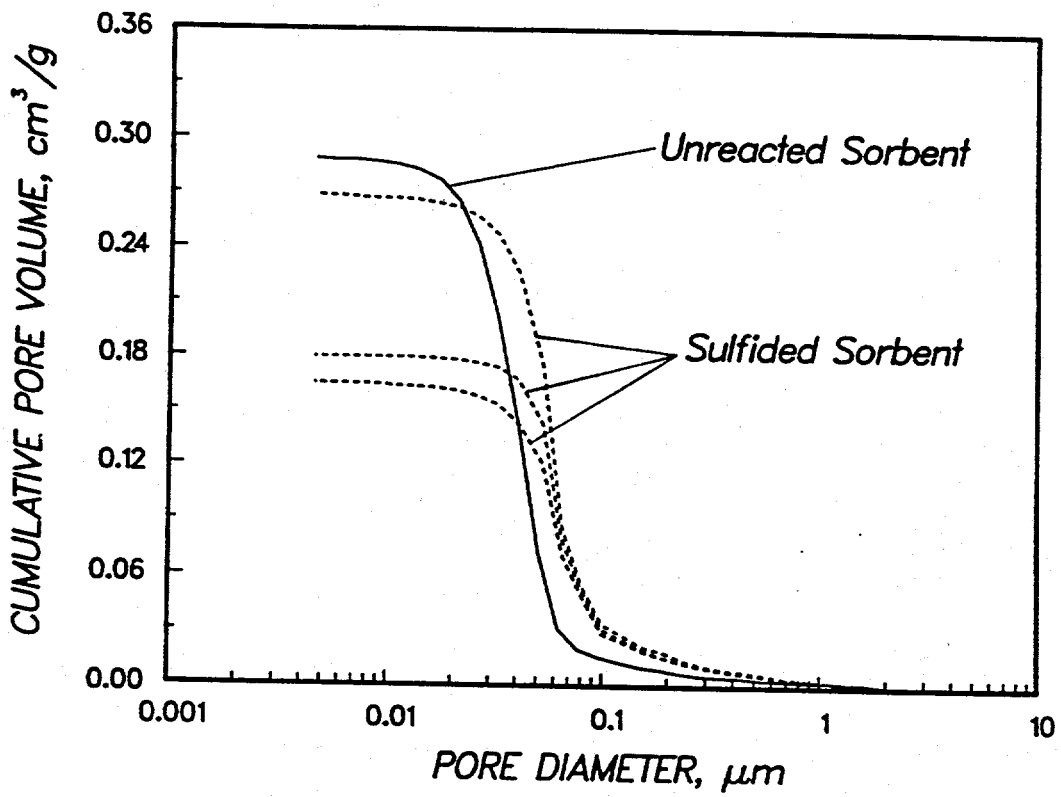

Figure 7.14: Porosimetric cumulative pore volume vs. pore diameter curves of unreacted C7-2 sorbent and those of solid samples collected from the top, middle, and bottom of the sorbent bed of run FB211.

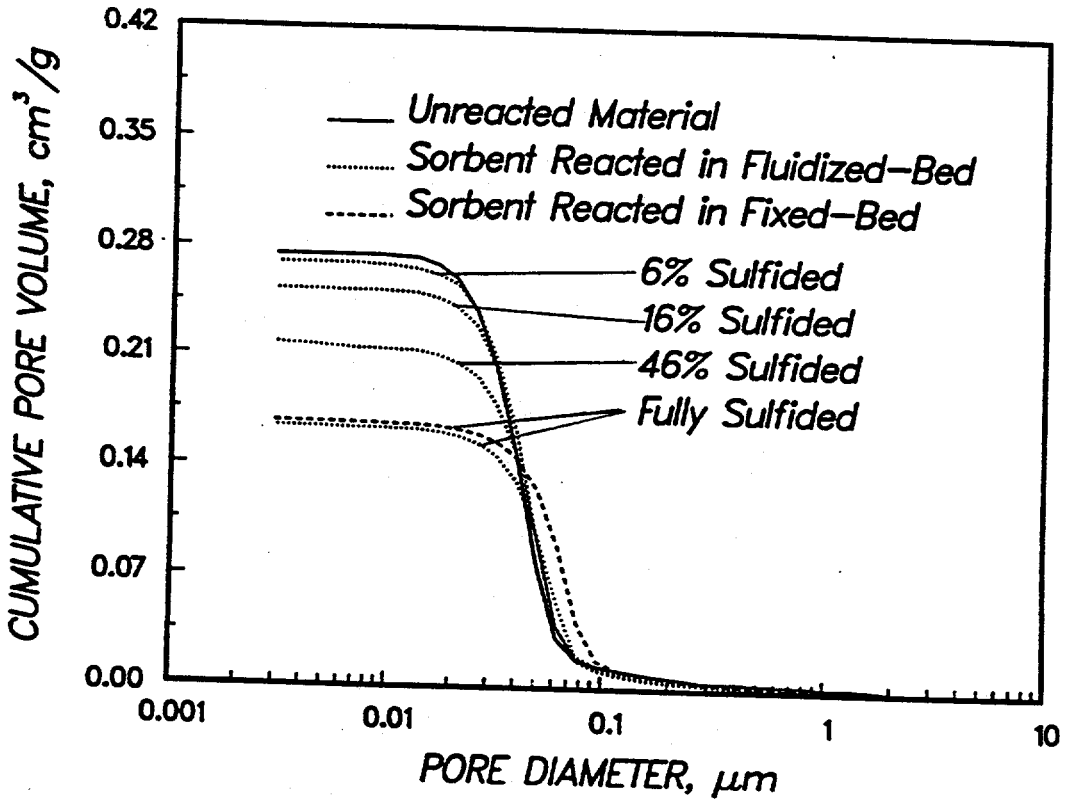

Figure 7.15: Pore volume distributions of sample C7-2 sulfided in a fluidized and in fixed-bed reactor.

the fluidized-bed reactor toward larger pores. Actually, all samples appear to have similar cumulative pore volume distributions in the region of large pores.

All particles in a fluidized-bed reactor experience, on the average, the same reaction conditions, and as a result, partially reacted samples prepared in such a reactor consist of particles of the same conversion. Samples collected from a fixed-bed reactor, on the other hand, cover a range of conversion levels, which may be rather broad depending on the part of the bed they were taken from (see Figs. 7.11 and 7.12). This difference is important when comparing the pore volume distributions of partially reacted samples of the same conversion from the two reactors, but it alone cannot explain the observed shift of the pore volume distribution of the fixed-bed samples toward large pores. However, since no mixing takes place in the fixed-bed reactor, with the exception of the layer of particles located at the entrance of the reactor, all other particles see the reactive mixture for the first time after they spend some time – which is roughly proportional to their distance from the entrance in the reactor – exposed to the product stream of the reaction, namely, a stream containing a% H_2O for a reactive mixture containing a% H_2S. Analysis of the pore structure of C7-2 particles (710-850 μm) exposed at 600^oC to a stream containing 1% H_2O for 2 hr showed shifting of the pore size distribution towards larger pores, though to a less extent than in Fig. 7.13. In view of this finding, it was postulated that the displacement of the pore size distributions of the fixed-bed samples toward large pores is caused by structural changes occurring because of the exposure of the sorbent particles to water vapor. Water vapor is also present in the fluidized-bed reactor, but since the internal surface of all particles is covered by a progressively thicker layer of sulfided phase, the occurring structural changes are less extensive.

The initial pore size distributions used in the application of the mathematical model (solid curves of Figs. 7.13 and 7.14) give pore surface areas 22 and 23 m^2/g, for sorbent G-72D and C7-2, respectively (pores greater than 50 Å in radius). These values are close to the BET surface areas of the unreacted materials (see Table 7.1). BET surface areas of fully sulfided samples of the two sorbents are listed in Table 7.3. The generalized pore model predicts that the surface area of the fully sulfided G-72D and C7-2 sorbents should be 16 and 18 m^2/g, respectively. The smaller experimental values of internal surface area for

the sulfided sorbents are not unexpected considering the displacement of the experimental pore volume distributions toward larger pores. Another reason for this discrepancy may be the use of the pore size distribution extracted from mercury intrusion data in the mathematical model. This distribution corresponds to the true pore size distribution only for an ideal structure of infinitely long cylindrical pores. For an arbitrary structure, it gives a measure of the distribution of feeder pores through which mercury invades the interior of the sorbent, and as a result it is narrower and located at smaller pore sizes than the actual pore size distribution of the solid.

Material	Experiment	Surface Area (m^2/g)
G-72D	FB209	9.4
G-72D	FB212	7.9
C7-2	FB211	13.55
C7-2	FB101	15.83
C7-2	FB102	13.62

Table 7.3: BET surface areas of fully sulfided zinc oxide sorbents.

7.8. Summary and Conclusions

Two commercially available zinc oxide sorbents were reacted at high temperatures using H_2S-N_2 mixtures in a fixed-bed reactor. Particles in the size range of 210-850 μm were used in the experiments. Breakthrough curves were determined experimentally by chromatographic analysis of the stream leaving the reactor. The comparison of experimental data obtained under the same sulfidation conditions for the two sorbents showed that the pore structure of the sorbents plays a major role in determining sorbent utilization in the bed at the breakthrough point. Other parameters having strong effects on the behavior of the reactor were the size of the particles and the residence time of the reactive mixture in the reactor. Experiments at 500 and 600^oC showed that the reaction temperature

influenced insignificantly the performance of the two solids as sorbents for H_2S removal.

Samples of fully or partially reacted particles collected from different parts of the fluidized-bed reactor were analyzed by mercury porosimetry and gas adsorption. The pore volume distribution of the reacted (partially and fully) samples was found to be shifted toward larger pores relative to the distribution of the unreacted solids. Such behavior was not seen in solids sulfided in a fluidized-bed reactor under the same conditions (temperature, pressure, and reactive gas mixture composition) as in the fixed-bed experiments. Since the particles in a fluidized-bed reactor remain exposed to the product stream of the reaction until the reaction front reaches them, it is believed that the displacement of their pore size distribution toward larger pores is caused by structural changes occurring because of their exposure in the water vapor produced by the sulfidation reaction.

The experimental results (breakthrough curves and pore structure data) were used to test the predictions of a mathematical model for fixed-bed desulfurization reactors. The behavior of each particle in the fixed-bed reactor was described using the generalized random pore model of Yu and Sotirchos (1987). Reactivity evolution data from thermogravimetric analysis experiments had been used in a past study to determine the values of the various parameters appearing in the generalized random pore model for each of the sorbents, and as a result, the application of the overall model to the fixed-bed data involved no unknown parameters. Very good agreement was observed between model predictions and experimental data for all cases examined in our study. The mathematical model reproduced successfully both the breakthrough curves and the solid conversion profiles in the fixed-bed reactor.

It must be pointed that it is not necessary to use adetailed model, like the one employed in this study, to describe the transport, reaction, and structure evolution processes in the pellets if our only objective is to use the overall mathematical model to correlate the experimental data. Since the general shape of the breakthrough curve is weakly influenced by the detail built into the pellet model, any model would succeed in reproducing the experimental curves provided that its parameters are allowed to vary from one experiment to another. For instance, Wang et al. (1990) used the unreacted-core model to describe the behavior of each pellet and obtained very good agreement between model results and

experimental data from a bench-scale reactor loaded with zinc ferrite or zinc titanate pellets. However, the the effective diffusivity values that had to be used to obtain good agreement between model and experiment were much different from those used in another study (Woods et al., 1991) to reproduce, using the unreacted-core model, sulfidation data for single pellets of the same sorbents from gravimetric experiments.

7.9. Notation

Symbols that do not appear here are defined in the text.

a	radius of the particle, cm
c	reactive gas concentration in the bed, mol/cm^3
c_0	initial reactive gas concentration in the bed, mol/cm^3
c_b	reactive gas concentration in the bulk phase, mol/cm^3
c_p	reactive gas concentration in the particle, mol/cm^3
$\mathcal{D}$	bulk diffusion coefficient, cm^2/s
D_b	axial dispersion coefficient in the fixed-bed, cm^2/s
D^e	effective diffusion coefficient in the particle, cm^2/s
D_0^e	initial effective diffusion coefficient in the particle, cm^2/s
k_g	mass transfer coefficient, cm/s
k_s	reaction rate constant in the particle, cm/s
k_v	volumetric reaction rate constant in the particle, s^{-1}
k_{v0}	initial volumetric reaction rate constant in the particle, s^{-1}
$\bar{k}_v$	average volumetric reaction rate constant in a particle or in the bed, s^{-1}
L	length of the sorbent bed, cm
Pe	Peclet number (see Eq. 7.12c)
r	radial distance in a particle, cm
$\bar{R}_v$	average reaction rate per unit of particle volume, $mol/cm^3/s$
S_0	initial surface area, cm^2/cm^3
Sh^e	Sherwood number (see Eq. 7.6c)
t	time, s

t_0	minimum time for the complete conversion of the sorbent bed, s
u	superficial velocity in the reactor, cm/s
v_s	volume of the unreacted solid per mol of the solid reactant, cm^3/mol
x	dimensionless distance in the bed
x_i	dimensionless distance of point i in the bed
y	dimensionless concentration in the bed
y_p	dimensionless concentration in the particle
z	axial distance in the bed, cm
Z	volume of fully reacted solid phase per unit volume of unreacted solid phase

Greek

δ^e	dimensionless effective diffusivity
ϵ_0	porosity of the unreacted particles
ϵ_b	bed voidage
ϵ_p	porosity of the reacted particles
$\hat{\epsilon}$	average porosity of particles located in a segment of the sorbent bed
η	tortuosity factor for axial dispersion
κ_v	dimensionless reaction rate constant in a particle
ν_A	stoichiometric coefficient of the reactive gas
ξ	local solid conversion in a particle
$\bar{\xi}$	average solid conversion in a particle or in the bed
$\hat{\xi}$	average conversion of particles located in a segment of the fixed-bed
ρ	dimensionless distance in a particle
τ	dimensionless time for the fixed-bed reactor (see Eq. 7.13a)
τ_p	dimensionless time for the particle (see Eq. 7.6a)
Φ^2	Thiele modulus for the particle (see Eq. 7.6b)
$\bar{\Phi}^2$	Thiele modulus for the sorbent bed (see Eq. 7.13b)
ω	dimensionless parameter (see Eq. 7.13c)
ω_p	dimensionless parameter (see Eq. 7.5e)

7.10. Literature References

Barin, I.; Knacke, O., *Thermochemical Properties of Inorganic Substances*, Springer-Verlag, New York (1973).

De Boer, J.H.; Linsen, B.G.; Van Der Plas, T.; Zondervan, G.J., "Studies on Pore Systems in Catalysts. VII. Description of the Pore Dimensions of Carbon Blacks by the t-method," J. Catalysis, **4**, 649-653 (1965).

Caillet, D.A.; Harrison, D.P., "Structural Property Variations in the MnO-MnS System," Chem. Eng. Sci., **37**, 625-636, (1982).

Dixon, A.G., "Correlations for Wall and Particle Shape Effects on Fixed Bed Bulk Voidage," Can. J. Chem. Eng., **66**, 705-708 (1988).

Efthimiadis, E.A.; Sotirchos, S.V., "Effects of Pore Structure on the Performance of Coal Gas Desulfurization Sorbents," AICHE Summer Meeting, Pittsburgh (1991).

Gangwal, S.K.; Harkins S.M.; Woods, M.C.; Jain, S.C.; Bossart, S.J., "Bench-Scale Testing of High-Temperature Desulfurization Sorbents," Environ. Progress, **8**, 265-269 (1989).

Grindley, T., "Sidestream Zinc Ferrite Regeneration Tests," Proceedings of the Eighth Annual Gasification and Gas Stream Cleanup Systems Contractors Review Meeting, **1**, 58-82, DOE/METC/6092 (1988).

Jain, S.C.; Gangwal, S.K.; Gal, E.; Ayala, R.E.; "A Study of the Chemical Reactivity and Mechanical Durability of High-Temperature Desulfurization Sorbents for Moving-Bed and Fluidized-Bed Applications," AIChE Summer National Meeting, San Diego (1990).

Krishnan, S.V.; Sotirchos, S.V., "Effective Diffusivity Changes during Carbonation, Recalcination, and Sulfation of Limestone Calcines," Annual AIChE Meeting, Chicago (1990).

Lee, G.T.; Gansley, R.R.; Baird, M.J., "Fluid Bed Desulfurization of Coal-Derived Gas," AIChE Summer National Meeting, San Diego (1990).

Park, H.C.; Kimura, S.; Sakai, Y.; Tone, S.; Otake, T., "An Unsteady State Analysis of Packed Bed Reactors for Gas-Solid Reactions," J. Chem. Eng. Japan, **17**, 269-274 (1984).

Sotirchos, S.V.; Yu, H.C., "Mathematical Modelling of Gas-Solid Reactions with Solid Product," Chem. Eng. Sci., **40**, 2039-2052 (1985).

Sotirchos, S.V.; Yu, H.C., "Overlapping Grain Models for Gas-Solid Reactions with Solid Product," Ind. Eng. Chem. Res., **27**, 836-845 (1988).

Sotirchos, S.V.; Zarkanitis, S., "Pellet-Model Effects on Simulation Models for Fixed-Bed Desulfurization Reactors," AIChE J., **35**, 1137-1147 (1989).

Tamhankar, S.S.; Bagajewicz, M.; Gavalas, G.R.; Sharma, P.K.; Flytzani-Stephanopoulos, M., "Mixed-Oxide Sorbents for High-Temperature Removal of Hydrogen Sulfide," Ind. Eng. Chem. Process Des. Dev., **25**, 429-437 (1986).

Wang, J.C.P.; Groves F.R.; Harrison, D.P., "Modeling High Temperature Desulfurization

in a Fixed-Bed Reactor," Chem. Eng. Sci., **45**, 1693-1701 (1990).

Woods, M.C.; Gangwal, S.K.; Harrison, D.P.; Jothimurugesan, K.. "Kinetics of the Reactions of a Zinc Ferrite Sorbent in High-Temperature Coal Gas Desulfurization," Ind. Eng. Chem. Res., **30**, 100-107 (1991).

Yu, H.C.; Sotirchos, S.V., "A Generalized Pore Model for Gas-Solid Reactions Exhibiting Pore Closure," AIChE J., **33**, 382-393 (1987).

Yumura, M.; Furimsky, E., "Comparison of CaO, ZnO, and Fe_2O_3 as H_2S Adsorbents at High Temperatures," Ind. Eng. Chem. Process Des. Dev., **24**, 1165-1168 (1985).

Zarkanitis, S.E.; Efthimiadis, E.A.; Sotirchos, S.V., "Experimental Evaluation of a Class of Distributed Pore Size Models for Gas-Solid Reactions with Solid Product," Chem. Eng. Sci., **45**, 2761-2768 (1990).

8. A PARTIALLY OVERLAPPING GRAIN MODEL FOR GAS-SOLID REACTIONS

The reaction of gases with porous solids is among the most frequently encountered reactive systems in industrial applications. The products of a gas-solid reaction may consist of gases only (e.g., char combustion and gasification), or formation of other solid species with different properties from the solid reactant may take place (e.g., reaction of sulfur-containing gases with metal oxides and deposition of ceramic material in fibrous preforms). Regardless of whether a gasification or a solid product formation reaction is considered, a mathematical model must be used to describe the structural changes that occur in the interior of the porous solid in the course of the chemical reaction. The various mathematical models presented in the literature for this purpose are usually classified into two, rather broad, categories (Ramachandran and Doraiswamy, 1982): models based on the representation of the pore space of the porous media by a collection of hollow objects (pore models) and models based on the representation of the solid phase of the porous media by an assemblage of dense objects (grain models). Hybrid and other abstract representations of the pore structure of a porous medium are also possible (Bhatia, 1987), but most of the structural models of the literature fall into either of the above categories.

In a grain model, the pore structure of the reacting solid is typically viewed as consisting of uniform in size, unconsolidated (nonoverlapping) grains, usually of spherical shape, which react independently of each other in a shrinking core fashion (Szekely et al., 1976). Because of the simplicity of the grain model expressions for the variation of the structural properties of a reacting solid with the extent of the reaction, the models that are most frequently used in the literature for the analysis and interpretation of experimental data for gas-solid reactions are based on variants of the grain model. Among the most important modifications of the original formulation of the grain model by Barner and Mantell (1968) and Szekely and Evans (1970), one could mention the extension of the model to solids with distributed grain size (Szekely and Propster, 1975), the use of variable size grains to account for density differences between the solid product and the solid reactant (Georgakis et al., 1979), and the incorporation in the model of sintering effects on the structural changes of the solid (Ranade and Harrison, 1981).

The most important deficiency of the various versions of the grain model is the assumption of nonoverlapping grains at all conversion levels and all porosities, which leads to the prediction of monotonically decreasing reaction surface area with the progress of the reaction (reacted-unreacted solid interface for reactions with solid product or pore surface for gasification reactions). Moreover, there is a minimum close packing porosity for grains of a certain shape, and therefore, the assumption of unconsolidated grains for porosities below this threshold value is physically unrealistic. These shortcomings of the grain model can be removed by allowing the grains in the structure to overlap. A grain model for partially sintered spheres was developed by Lindner and Simonsson (1981) who represented the solid reactant as aggregates of spheres in an initial state of sintering. The derivation of approximations for the evolution of the structural properties of this structure with the extent of the reaction was accomplished by considering a sphere with an average number of nearest neighbors. The structural model of Lindner and Simonsson was modified by Alvfors and Svedberg (1988) to account for the presence of inert solids in the porous medium, and the modified model was used to study the sulfation of calcined limestones and dolomites. The notion of overlapping grains was further pursued by Sotirchos (1987) and Sotirchos and Yu (1988), who developed structural models for porous media that can be represented by a population of randomly overlapping grains of distributed size. Comparison of the predictions of the random grain model (Sotirchos and Yu, 1988) with those of the corresponding random pore model (Sotirchos and Yu, 1985) showed that grain structures react in a different manner from capillary structures. Sotirchos and Zarkanitis (1989) incorporated the random grain model in a design model for fixed-bed desulfurization reactors and showed that the grain size distribution may have a strong influence on the breakthrough behavior of the bed.

The assumption of freely overlapping grains makes possible the derivation of exact analytical expressions for the dependence of the structural properties of the porous medium on the conversion, but in actual porous media, the extent of grain overlapping should vary among different solids. For porous media prepared as powder compacts, in particular, the extent of grain overlapping should be a function of processing conditions and of procedures used for their preparation. A grain representation of a porous medium that is more flexible

than that of randomly overlapping grains is obtained when one considers a population of grains with each having a hard core surrounded by a penetrable soft shell. Only the soft shells of the grains can overlap with each other, when this population of grains is used to represent the structure of the porous medium. Obviously, at the limit of zero size of hard core one obtains the random overlapping grain model, while at the limit of zero thickness of soft shell, the nonoverlapping grain model results.

A special case of the partially overlapping grain model is obtained when all grains are assumed to have the same size and the same soft shell thickness or, equivalently, hard core size. Rikvold and Stell (1985) used the scaled-particle theory of Reiss, Frisch, and Lebowitz (1959) to develop expressions for the porosity and surface of D-dimensional partially overlapping spheres of uniform size and uniform hard core radius. (For $D = 2$, the obtained structure is that of parallel, partially overlapping cylindrical grains). Tomadakis and Sotirchos (1991a) used a Monte Carlo simulation scheme to compute the structural properties of partially overlapping cylinders ($D = 2$) and found that the relations proposed by Rikvold and Stell (1985b) provided an excellent approximation to the porosity of the structure in a rather wide range of porosity and cylinder to hard core radius ratio values. The surface areas predicted by the expression of Rikvold and Stell (1985b) were lower than the numerically computed values, but the agreement between the analytical results and the numerically computed values should be deemed satisfactory in view of the large computational times needed to obtain the latter.

A structure of partially overlapping spheres, with each sphere having the same radius and hard core radius, is used as basis in this study for the development of a partially overlapping spherical grain model for gas-solid reactions with solid product. The development of the mathematical model proceeds along the lines of the grain model of Sotirchos and Yu (1988). The expressions of Rikvold and Stell (1985a) are used to follow the variation of the porosity and surface area (reaction and pore surface area) with the extent of the reaction. In order to demonstrate the flexibility of the new model, a detailed parametric sensitivity analysis of its predictions is carried out, and the results are compared with those of the randomly overlapping and nonoverlapping grain models. Finally, the model is applied to the analysis of some experimental data for the sulfidation of zinc oxide, a

reaction used to remove sulfur-containing contaminants (primarily H_2S) from coal gas at high temperatures.

8.1. Local Reaction and Structure Evolution Model

Expressions for Porosity and Internal Surface Area

We consider a structure consisting of a population of uniformly sized, spherical grains of radius R. Each grain consists of a hard core of radius R_c and a penetrable soft shell. Such a structure can be obtained from an initial structure of randomly 'packed' nonoverlapping grains of radius R_c by letting the grains 'grow' from radius R_c to radius R. It thus makes sense to parametrize the system using the porosity of the structure made up of the hard cores of the grains ϵ_c and the grain growth variable δ, the latter defined as the ratio of grain radius to hard core radius.

For $\delta < 1$, the porosity and surface area of the porous medium are given by the expressions for hard (nonoverlapping) spheres, i.e.,

$$\varepsilon = 1 - \frac{4\pi}{3} n R^3 \tag{8.1}$$

$$S = 4\pi n R^2 \tag{8.2}$$

with n being the number of grains per unit volume. As $\delta \to \infty$, i.e., $R_c \to 0$, then the structural properties of the solid are given by the equations for randomly overlapping grains, i.e.,

$$\varepsilon = \exp(-\frac{4\pi}{3} n R^3) \tag{8.3}$$

$$S = \epsilon 4\pi n R^2 \tag{8.4}$$

For other values of δ and ϵ_c, we use the expressions derived by Rikvold and Stell (1985), which in terms of the quantities defined in this study have the form:

$$\epsilon = \epsilon_c \exp\left[-\frac{(\delta^3 - 1)(1 - \epsilon_c)}{\epsilon_c}\right]$$

$$\times \exp\left[-\frac{3(1-\epsilon_c)^2}{2\epsilon_c^3}(2(\delta-1)^3 + 3\epsilon_c(\delta-1)^2)\right] \tag{8.5}$$

$$S = \frac{3\epsilon(1-\epsilon_c)\delta}{R\epsilon_c^3}[\epsilon_c^2\delta^2 + (1-\epsilon_c)(3(\delta-1)^2 + 3\epsilon_c(\delta-1))] \tag{8.6}$$

Eq. (8.6) follows from differentiation of Eq. (8.5) with respect to R, using the fact that $S = d\epsilon/dR$. For $\delta = 1$, Eqs. (8.5) and (8.6) reduce to those for nonoverlapping grains, i.e., (8.1) and (8.2), but they become indeterminate as $\delta \to \infty$.

Rikvold and Stell (1985a) derived Eqs. (8.5) and (8.6) by realizing that a structure of partially permeable spheres is isomorphic to a fluid of hard spheres of radius R_c into which one attempts to introduce a hard solute molecule of radius $(R - R_c)$. This problem forms the basis of the scaled-particle theory for hard sphere fluids of Reiss, Frisch, and Lebowitz (1959). The porosity of the partially overlapping sphere structure corresponds to the volume accessible to the center of the solute molecule, while its internal surface area corresponds to the surface accessible to the center of the solute molecule when it is in contact with at least one solvent molecule. Reiss et al. (1959) derived exact expressions for quantities equivalent to ϵ and S in terms of the contact correlation function G, that is, the radial distribution function of the solvent molecules around a solute molecule on contact between solvent and solute. Eqs. (8.5) and (8.6) are based on a quadratic approximation of G in terms of the inverse particle separation. This approximation yields exact results up to the third virial coefficient (Reiss et al., 1959), and it is commonly referred to as the scaled-particle approximation.

The porosity and surface area of a porous medium can be measured using gas adsorption and mercury porosimetry. For the case of nonoverlapping or randomly overlapping spheres, Eqs. (8.1) and (8.2) or Eqs. (8.3) and (8.4), respectively, may be used to determine the values of the two parameters, n and R, that define the population of the spherical grains. A structure of partially overlapping grains requires, as Eqs. (8.5) and (8.6) show, three parameters for its unique characterization, namely, ϵ_c, R, and δ, and consequently, additional information about the pore structure of the porous medium is needed in order to be able to specify these parameters. For man-made porous media prepared as powder compacts, the radius of the spherical grains is a known quantity, while for other porous solids, it may be determined from direct photomicrographic observation of their structure. Another alternative is to treat one of the three parameters of the partially overlapping grain model as a free parameter and thus provide the structural model that can be based on Eqs. (8.5) and (8.6) with more flexibility than the corresponding structural model for

non- or freely overlapping grains.

Figs. 8.1 and 8.2 present the variation of the porosity, ϵ, and dimensionless surface area, SR, of a structure of partially overlapping spherical grains with the grain growth variable, δ, for various values of hard core porosity. Since the hard cores of the grains cannot overlap, the hard core porosity can only take values larger than the porosity corresponding to a structure of ordered close packed spheres, ϵ_{ocp} $(= (1 - \pi/18^{1/2}) \cong 0.2595)$. For $\delta = 0$, the porosity of the grain structure is equal to unity, while its internal surface area is zero (see Figs. 8.1 and 8.2). For δ values less than unity, the solid structure obviously consists of unconsolidated (nonoverlapping) grains, and the porosity and internal surface area are given by Eqs. (8.1) and (8.2), which in terms of ϵ_c, R, and δ can be written in the form

$$\epsilon = 1 - (1 - \epsilon_c)\delta^3 \tag{8.7}$$

$$S = \frac{3(1 - \epsilon_c)\delta^3}{R} = \frac{3(1 - \epsilon_c)\delta^2}{R_c} \tag{8.8}$$

As the radius of the grains and, hence, the growth variable increase, the porosity decreases becoming equal to the hard core porosity at $\delta = 1$.

The porosity and internal surface area predicted by Eqs. (8.5) and (8.6) become identically zero only for infinitely large values of the grain growth variable, regardless of the hard core porosity of the structure, while one would expect this to be the case only for randomly overlapping grains ($\epsilon_c = 0$). Nevertheless, as Figs. 8.1 and 8.2 show, the porosity and internal surface area of a partially overlapping grain structure given by Eqs. (8.5) and (8.6) become practically zero beyond a certain value of grain growth variable – which increases with increasing hard core porosity – and consequently, the above limitation of Eqs. (8.5) and (8.6) is not expected to influence in any way the predictions of the structural model we intend to build on them. Since the grains do not overlap for $\delta < 1$, the internal surface area always increases with increasing δ in this region. The internal surface area continues to increase as δ becomes greater than unity and the soft shells of the grains start to overlap with each other, but eventually, the loss of surface area because of grain overlapping offsets the gain caused by grain growth forcing the surface area of the solid to go through a maximum. For obvious reason, the position of the maximum moves towards smaller δ values with decreasing hard core porosity.

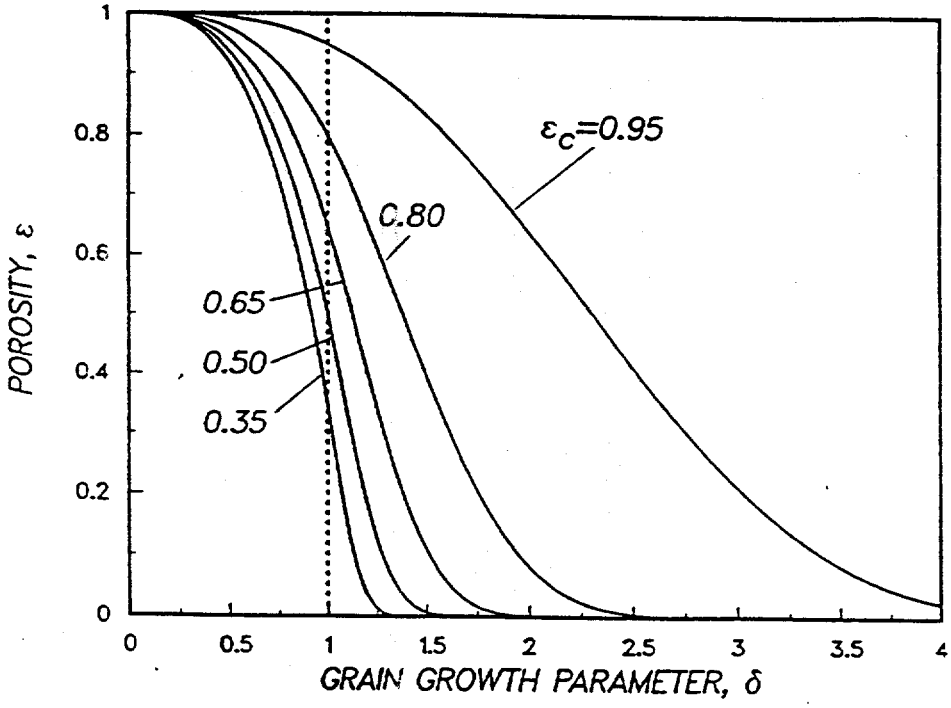

Figure 8.1. Variation of the porosity, ε, with the the grain growth variable (ratio of grain to hard core radius), δ, for several values of hard core porosity, ε_c.

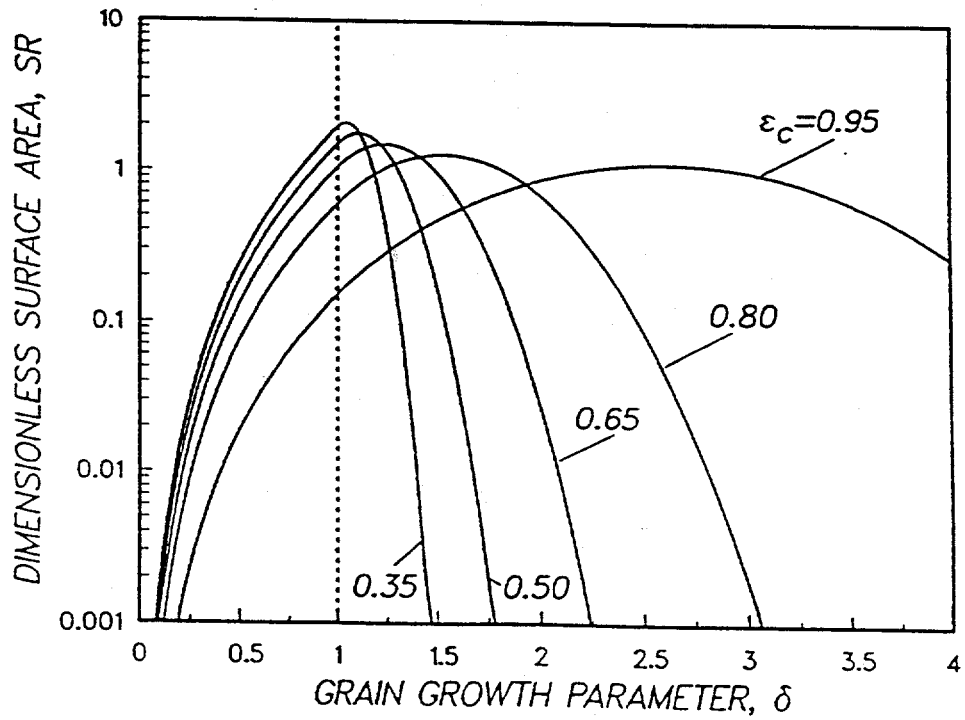

Figure 8.2. Variation of the dimensionless surface area, SR, with the the grain growth variable (ratio of grain to hard core radius), δ, for several values of hard core porosity, ε_c.

Reaction and Structure Evolution Equations

We are now ready to proceed with the development of the structure evolution model for gas-solid reactions with solid product. We will consider the general gas-solid reaction

$$S\ (\text{solid}) + \nu_A A(gas) + \cdots \rightarrow \nu_P P\ (\text{solid}) + \cdots \tag{8.9}$$

with $\cdots$ denoting other gases participating in the chemical reaction. The stoichiometrically equivalent molar volume of the solid product, $\nu_P v_P$, may be larger or smaller than the molar volume of the gaseous reactant, v_S, leading to decrease or increase, respectively, of the porosity of the reacting porous medium. Sulfidation and sulfation of metal oxides are typical examples of reactions accompanied by decrease in the porosity, while the oxidation of metal sulfides exemplifies reactions producing more open pore structures. An extreme example of the latter type of reactions is the class of gasification reactions, which is also covered by Eq. (8.9) for ν_P equal to zero.

We define the stoichiometric volume ratio of the (solid reactant, solid product) pair, Z, as the ratio of stoichiometrically equivalent volumes of solid product and solid reactant ($Z = \nu_P v_P / v_S$). Z is in general different from unity or zero, and as a result, the internal structure of the reacting porous medium is characterized by two evolving interfaces, defining the reaction and pore surfaces of the solid. Each point of the reaction or pore surface moves with velocity proportional to the local reaction in the direction of the unit vector that is normal to the surface there. Therefore, each of these two surfaces can be represented by a population of grains that are concentric to those forming the initial structure and, hence, have the same hard core radius and hard core porosity.

Let R_0 be the initial grain radius, R_r the radius of the grains forming the reaction surface, and R_p the radius of the grains forming the pore surface. We express the intrinsic rate of the reaction, $\mathcal{R}_s$, in terms of the change in R_r as

$$\frac{dR_r}{dt} = -v_S \mathcal{R}_s(c_r, T) \tag{8.10}$$

where c_r is the concentration of the gaseous species at the reaction surface. Assuming that the concentration of the gaseous reactant is the same at all points of the product layer, between R_r and R_p, that are at the same distance in the radial direction from the pore or

reaction surface and solving the diffusion equation in the product layer, we find that

$$c_p - c_r = \frac{\nu_A}{D_P}\mathcal{R}_s(c_r, T)S_r \int_{R_r}^{R_p} \frac{dR}{S(R)} \tag{8.11}$$

c_p is the concentration of the gas in the pores, $S_{r,p}$ is the reaction or pore surface area, D_P is the diffusion coefficient of the gas in the product layer, and $S(R)$ is the surface area of the grain structure when the grain radius is R. Obviously, $S(R_{r,p}) \equiv S_{r,p}$. For a first-order reaction, combining Eqs. (8.10) and (8.11) gives

$$\frac{dR_r}{dt} = -\frac{v_S k_s c_p}{1 + \frac{\nu_A k_s}{D_P} S_r \int_{R_r}^{R_p} \frac{dR}{S(R)}} \tag{8.12}$$

The equation for the change of R_p results from a balance on the solid. We have that

$$\frac{dR_p}{dt} = -\frac{dR_r}{dt}[(Z-1)\frac{S_r}{S_p}] \tag{8.13}$$

The initial conditions for Eqs. (8.12) and (8.13) obviously have the form:

$$R_r(0) = R_p(0) = R_0 \tag{8.14}$$

In dimensionless form, Eqs. (8.12)-(8.14) may be written as

$$\frac{dy_r}{d\tau} = -\frac{1}{1 + \beta(S_r/S_0)\int_{y_r}^{y_p} \frac{dy}{(S(R)/S_0)}} \tag{8.15}$$

$$\frac{dy_p}{d\tau} = -\frac{dy_r}{d\tau}[(Z-1)\frac{(S_r/S_0)}{(S_p/S_0)}] \tag{8.16}$$

$$y_r(0) = y_p(0) = R_0 S_0 \tag{8.17}$$

with

$$y_{r,p} = R_{r,p}S_0; \quad \beta = \frac{\nu_A k_s}{D_P S_0} \tag{8.18a,b}$$

$$\tau = v_S k_s S_0 \int_{t_0}^{t} c_p dt' \tag{8.19}$$

The dimensionless structural model is independent of the reactive gas concentration and its variation with time, the initial internal surface area of the grain structure, and the molar volume of the solid reactant. The reaction rate constant, product layer diffusivity, and initial internal surface area have been grouped into the dimensionless parameter β, which can be viewed as a measure of the ratio of the magnitudes of the relative rates of reaction at the solid-solid interface and mass transport in the product layer. For $\beta = 0$, the rate of mass transport in the product layer is infinitely fast relative to the rate of reaction, and as a result, reaction occurs in the kinetically controlled regime. On the other hand, as $\beta \rightarrow \infty$, the overall rate of reaction becomes controlled by diffusion in the product layer.

With the initial porosity and internal surface area of the solid known, possibly from physical adsorption or mercury porosimetry measurements, δ_0 $(= R_0/R_c)$ has to be specified to complete the description of the system, provided, of course, that values from the various kinetic and transport parameters are available. Using Eqs. (8.5) and (8.6) (for $\delta_0 > 1$) or eqs. (8.7) and (8.8) (for $\delta_0 < 1$, i.e., an initial structure of unconsolidated grains), we can compute the values of hard core porosity, ϵ_c, and initial grain radius, R_0, for the chosen set of ϵ_0, S_0, and δ_0 values. Another option is to specify ϵ_c and solve the equations for δ_0 and R_0. The evolution of the properties of the reaction surface and pore surface structures, subscripts r and p, respectively, are also followed using Eqs. (8.5) and (8.6) or (8.7) and (8.8). Since the grains representing the reaction and pore surface structure are concentric to those of the original structure, their hard core porosity and hard core radius are the same. The grain growth variable, $\delta_{r,p}$ that must be used in equations (8.5) and (8.6) or (8.7) and (8.8) to obtain the porosity and internal surface area is given by

$$\delta_{r,p} = \frac{R_{r,p}}{R_0} = \frac{y_{r,p}}{S_0 R_0} \tag{8.20}$$

For the dimensionless form of the model, it is necessary to define only the values of ϵ_0 and δ_0 in order to obtain a completely described structure. However, it should be kept in mind that the dimensionless reaction times can be compared to each other only for solids of the same initial internal surface area.

The mathematical model of Eqs. (8.15) and (8.16) is solved as an initial value problem consisting of three ordinary differential equations, the third differential equation obtained

by setting the integral appearing in the denominator of the right-hand side of Eq. (8.15) equal to an auxiliary variable g, i.e., by setting $g = \int_{y_r}^{y_p} \frac{dy}{S(R)/S_0}$. More details on the solution procedure may be found in the paper by Sotirchos and Yu (1988). Notice that by eliminating $d\tau$ from Eq. (8.16), a differential equation between y_r and y_p is obtained, which can be solved independently of Eq. (8.15), that is, independently of the processes of diffusion in the product layer and chemical reaction. The fractional conversion, ξ, of the solid is obtained from the porosity, ϵ_p, or the 'porosity' of the reaction surface structure, ϵ_r, by using the relationship

$$\xi = \frac{\epsilon_r - \epsilon_0}{\epsilon_0} = \frac{\epsilon_0 - \epsilon_p}{(Z-1)(1-\epsilon_0)} \qquad (8.21a,b)$$

which results from an overall mass balance in the solid reactant and solid product. According to Eq. (8.21b), complete pore closure ($\epsilon_p = 0$) for conversions less than unity may take place for initial porosities smaller than $(Z-1)/Z$ (obviously, for $Z > 1$).

8.2. Structural Model Results

The local reaction and structure evolution model developed in the preceding section suffices for the description of the behavior of a gas-solid reaction process under reaction conditions controlled by intrinsic kinetics and diffusion in the product layer, that is, in the absence of significant concentration gradients in the intraparticle space. Four parameters are involved in the dimensionless form of the structural model (see Eqs. (8.13)-(8.21)): ϵ_0, extent of grain overlapping (quantified by ϵ_c or δ_0 for partially overlapping grains), β, and Z. Before proceeding with the presentation and discussion of our numerical results, we will briefly discuss our choices for the values of these parameters.

The initial porosity of porous media encountered in practical applications usually varies in the range [0.4, 0.6]. In order to simplify the investigation of the parametric sensitivity of the problem, the initial porosity will be fixed at 0.5 in all the numerical results that will be presented in our study. Four grain overlapping patterns will be employed in our analysis: i) the well-known nonoverlapping grain model (NOGM) in which the area and porosities of the pore and reaction surface structures are given at all porosity (or conversion) levels by Eqs. (8.1) and (8.2); ii) the randomly overlapping grain model (ROGM)

of Sotirchos and Yu (1988) in which the porosities and areas are given by Eqs. (8.3) and (8.4); iii) the partially overlapping grain model (POGM) with initially nonoverlapping grains ($\delta_0 = 1$); and iv) the partially overlapping grain model with $\delta_0 = 1.2$.

The stoichiometric volume ratio, Z, is zero for gasification reactions ($\nu_P = 0$ in Eq. (8.9)), but for gas-solid reactions with solid product formation, its value varies widely depending on the (solid reactant, solid product) pair; for example, $Z = 1.62$ for (ZnO, ZnS), $Z = 0.62$ for (ZnS, ZnO), $Z = 3.09$ for (CaO, $CaSO_4$), and $Z = 4.01$ for (MgO, $MgSO_4$). In our analysis for the parametric sensitivity of the problem, we will work with $Z = 2$, the largest Z value that permits complete conversion of the solid reactant for 0.5 initial porosity before complete pore plugging takes place, and $Z = 3$, a value characteristic of the sulfation of calcined limestones (see above), a gas-solid reaction of much importance in the control of SO_2 emissions from coal-fired power plants. Parameter β, which expresses how fast the intrinsic reaction is relative to the diffusion of the gaseous reactant through the product layer, can take any value between zero and infinity depending on the reaction conditions. We will present results for the two extremes of intrinsic reaction control and product layer diffusion control ($\beta = 0$ and $\beta = \infty$) and for an intermediate case ($\beta = 1$) where both the resistance for reaction and that for diffusion through the solid product are important.

Fig. 8.3 presents the variation of the internal surface area, normalized with respect to its initial value, with the porosity for a solid with 0.5 initial porosity for the four patterns of grain overlapping considered in our study. Internal surface area (normalized) vs. porosity curves for other initial porosities are shown in Fig. 8.4 for the case of partially overlapping grains with $\delta_0 = 1$. As it is indicated in Fig. 8.3, the surface areas for porosities less than the initial correspond to the pore surface areas (S_p) for gas-solid reactions with $Z > 1$, while those for porosities greater than the initial describe the evolution of the reaction surface area (S_r) or of the pore surface area for $Z < 1$. The surface area of the nonoverlapping grain model increases monotonically with decreasing porosity since the grains are assumed to react independently of each other (i.e., not to overlap) even for porosities smaller than the porosity corresponding to the densest ordered close packing of hard spheres, viz. 0.2595. All other patterns of grain overlapping give zero internal surface

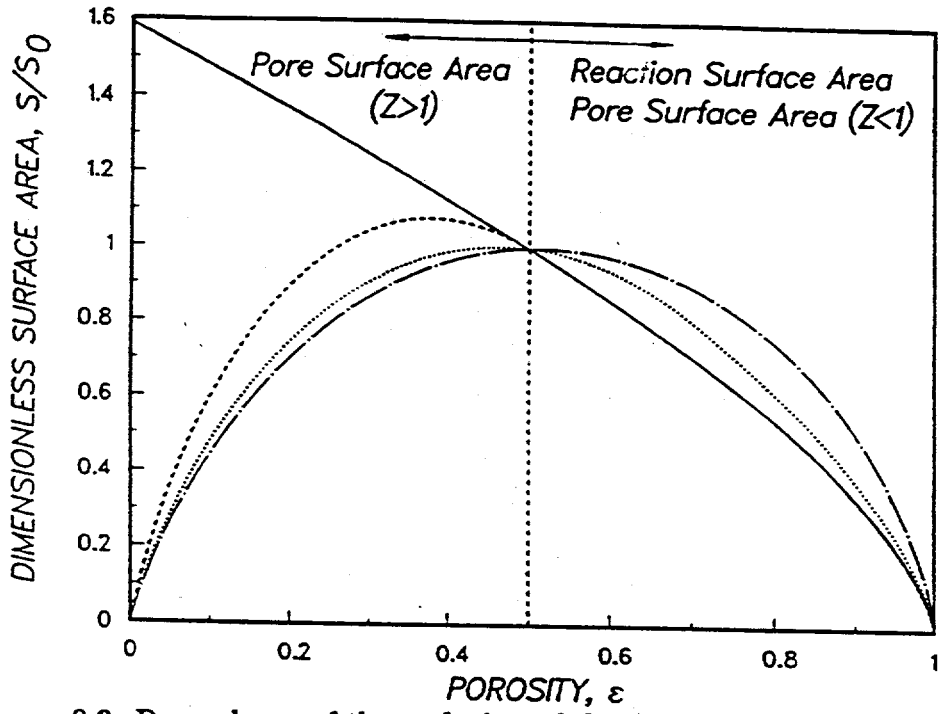

Figure 8.3. Dependence of the evolution of the dimensionless internal surface area, S/S_0, with the porosity of a grain structure with ε_0=0.5 on the extent of grain overlapping. ———: nonoverlapping grains (NOGM); – – –: partially overlapping grains (POGM) with δ_0=1; ·····: partially overlapping grains (POGM) with δ=1.2; – · –: randomly overlapping grains (ROGM).

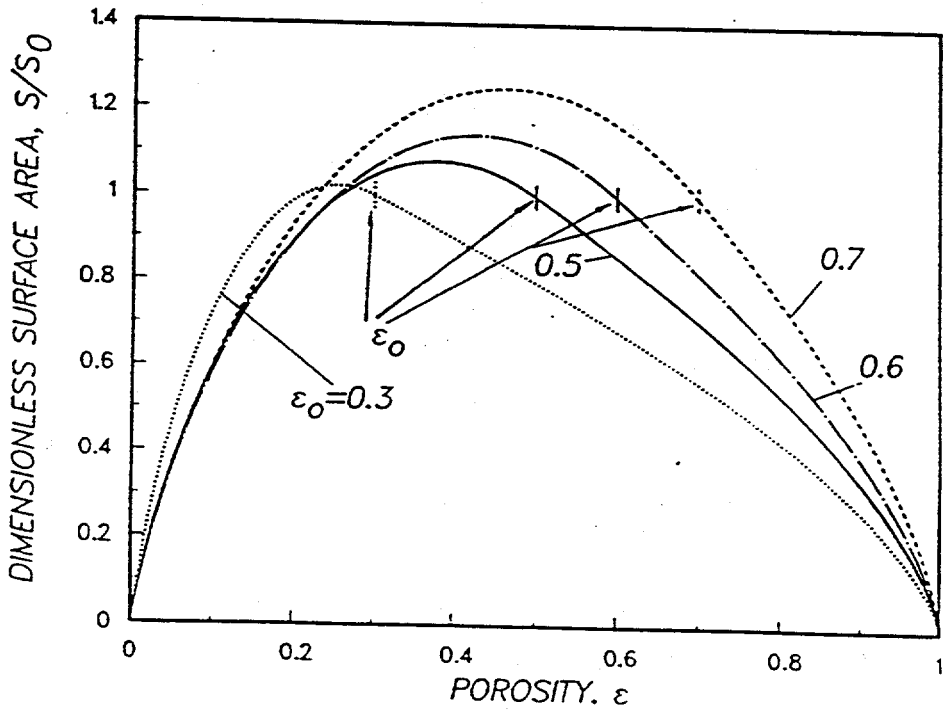

Figure 8.4. Evolution of the dimensionless internal surface area, S/S_0, with the porosity of a grain structure with δ_0=1 (i.e., $\varepsilon_c = \varepsilon_0$) for several values of initial porosity.

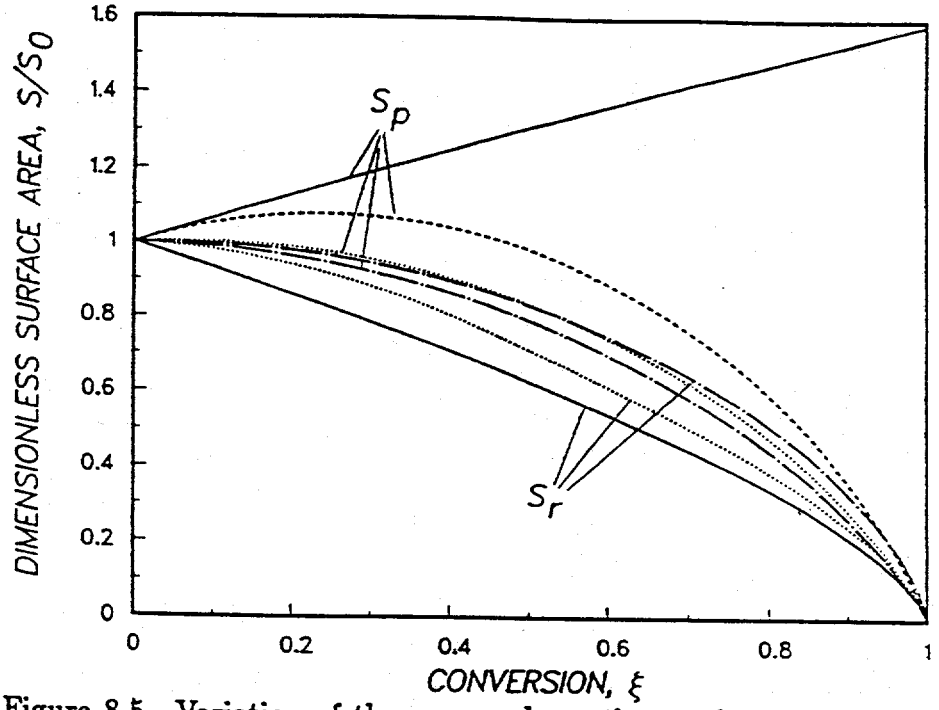

Figure 8.5. Variation of the pore and reaction surface areas with the conversion for $Z = 2$. The reaction surface area of partially overlapping grains with δ_0=1 evolves in the same way as that of nonoverlapping grains. ———: nonoverlapping grains (NOGM); – – –: partially overlapping grains (POGM) with δ_0=1; ·····: partially overlapping grains (POGM) with δ=1.2; – · –: randomly overlapping grains (ROGM).

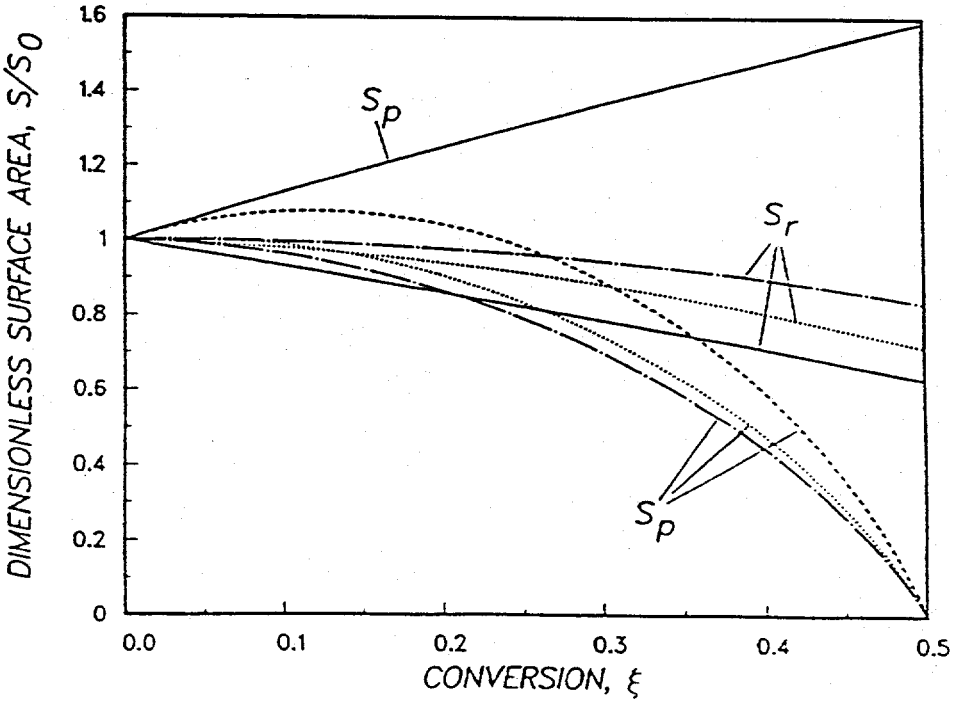

Figure 8.6. Variation of the pore and reaction surface areas with the conversion for $Z = 3$. The reaction surface area of partially overlapping grains with δ_0=1 evolves in the same way as that of nonoverlapping grains. ———: nonoverlapping grains (NOGM); – – –: partially overlapping grains (POGM) with δ_0=1; ·····: partially overlapping grains (POGM) with δ=1.2; – · –: randomly overlapping grain model (ROGM).

area for zero and unity porosity, and therefore, they are consistent with the physics of the problem. It can be shown using Eqs. (8.3) and (8.4) that the maximum surface area for randomly overlapping grains occurs at $\epsilon = e^{-(2/3)} \cong 0.51$. In the partially overlapping grain model, the maximum surface area occurs at porosities smaller than the initial for $\delta_0 \leq 1$ (see Figs. 8.2 and 8.4) while for initially overlapping grain structures ($\delta_0 > 1$), the position of the maximum relative to the initial porosity depends on ϵ_0 and δ_0.

The results of Figs. 8.3 and 8.4 are valid for any value of Z, but in order to follow the evolution of the pore and reaction surface areas with the conversion, these results must be used in conjunction with Eq. (8.21). Surface area vs. conversion curves for gas-solid reactions with $Z = 2$ and $Z = 3$ (i.e., the values that we will use in this study), constructed using Fig. 8.3 and Eq. (8.21), are shown in Figs. 8.5 and 8.6, respectively. For $Z = 2$, the porosity becomes exactly zero when complete conversion of the solid takes place, and as a result, both the pore and reaction surface areas of structures with overlapping grains (ROGM and POGM) are zero (Fig. 8.5). The maximum conversion that can be reached before complete pore plugging takes place ($\epsilon_p = 0$) for $\epsilon_0 = 0.5$ and $Z = 3$ (Fig. 8.6) is equal of 0.5 ($\xi_{max} = \dfrac{\epsilon_0}{(1-\epsilon_0)(Z-1)}$, see Eq. (8.21b)). For $Z = 3$, the pore surface area of structures with overlapping grains is zero at the maximum conversion, as in the case with $Z = 2$, but the reaction surface area is finite because of the presence of unreacted solid in the particles. For obvious reasons, the reaction surface area of partially overlapping grains with $\delta_0 = 1$ evolves in the same fashion as that of nonoverlapping grains.

Gas-solid reactions with $Z > \frac{1}{1-\epsilon_0}$ will have surface area evolution histories similar, qualitatively, to those for $Z = 3$ (Fig. 8.6). The reaction surface areas of system, with $Z \leq \frac{1}{1-\epsilon_0}$ will vary in a similar fashion as the corresponding curves of Fig. 8.2, while the qualitative variation of their pore surface areas – which will be finite at $\xi = 1$ – will depend on whether Z is greater or less than unity (see Fig. 8.3). The most interesting observation from the results shown in Figs. 8.3, 8.5 and 8.6 is that the reaction surface area at a certain conversion increases with increasing grain overlapping, while the opposite trend holds for the pore surface areas for gas-solid reactions with $Z > 1$. This behavior will be used later to explain the differences in the reaction vs. time histories of solids with different patterns of grain overlapping.

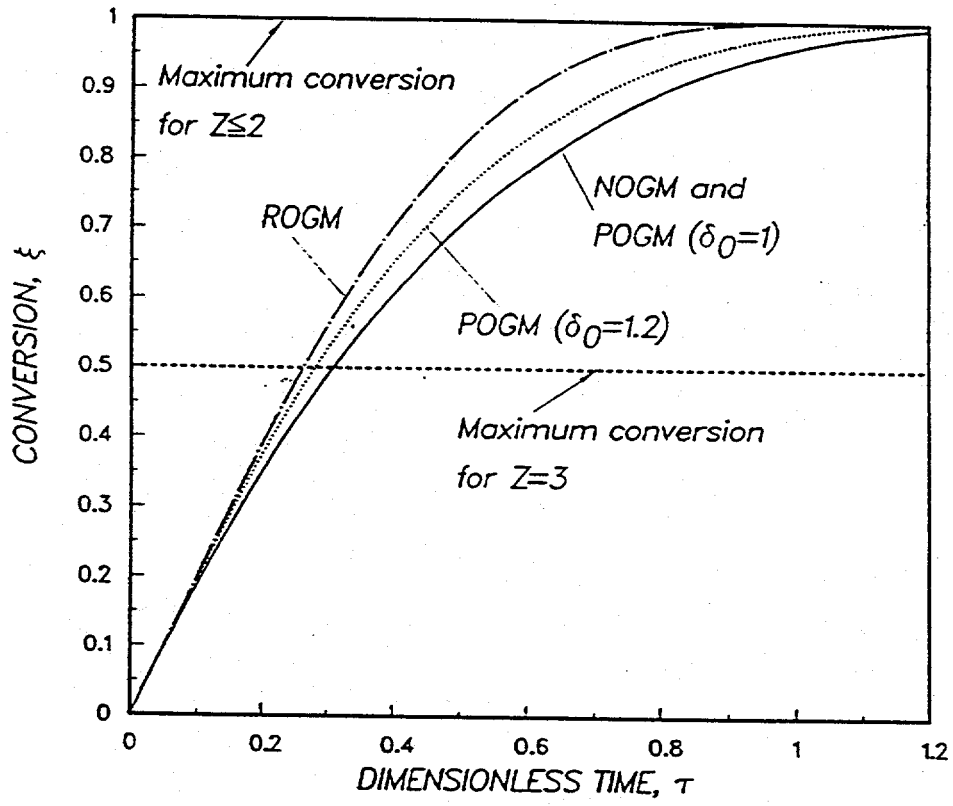

Figure 8.7. Conversion vs. time curves for insignificant diffusional limitations in the product layer ($\beta = 0$). The conversion evolution curves of nonoverlapping grains and partially overlapping grains with δ_0=1 are the same. NOGM: nonoverlapping grains; POGM: partially overlapping grains; ROGM: randomly overlapping grains.

Conversion vs. time results for reaction conditions controlled by intrinsic kinetics ($\beta = 0$) are shown in Fig. 8.7. Since nonoverlapping grains (NOGM) and partially overlapping grains (POGM) with $\delta_0 = 1$, have the same reaction surface area (see Figs. 8.3, 8.5, and 8.6) and the resistance for diffusion through the product plays no role in the process, the conversion vs. time curves for these two patterns of structure evolution are identical. For the same reason, the conversion evolution results are independent of the value of the stoichiometric volume ratio (Z), although the latter still determines the maximum allowable conversion, as it is indicated in Fig. 8.7 for $Z = 3$. Since the local reaction rate is proportional to the internal reaction surface area (S_r) and the concentration at the reaction interface is the same as that in the pores, the reaction rate and, hence, the conversion of the solid follow the same trend as S_r with increasing overlapping, that is, they also increase.

Figs. 8.8 and 8.9 present conversion evolution histories for $\beta = \infty$, that is, under reaction conditions controlled by diffusion in the product layer. Since $\beta \to \infty$ is equivalent to letting the reaction occur infinitely fast relative to the diffusion of the gaseous reactant in the product layer (i.e., $k_s \to \infty$), it is necessary to redefine the dimensionless time as

$$\tau' = \lim_{k_s \to \infty} \frac{\tau}{\beta} = (v_S/\nu_A) D_P S_0^2 \int_0^t c_p dt' \tag{8.22}$$

Comparison of Figs. 8.8 and 8.9 reveals that the effects of grain overlapping on the conversion trajectories become stronger as the stoichiometric volume ratio (Z) increases. Moreover, the relative positions of the various conversion vs. time curves appear to be influenced by the Z value. In particular, it is interesting to observe that for $Z = 3$, the order of the four conversion vs. time curves is reversed relative to that seen in Fig. 8.7 for $\beta = 0$, that is, the conversion reached after some reaction time now decreases with increasing grain overlapping. These results can be explained with the aid of Figs. 8.5 and 8.6 for the variation of the surface areas with the conversion. As shown there, the pore surface area increases with decreasing grain overlapping (ROGM $\to$ POGM $\to$ NOGM), and therefore, more surface area is available for diffusion through the product layer for $R > R_0$, and the thickness of the product layer is smaller. These two factors gain importance as

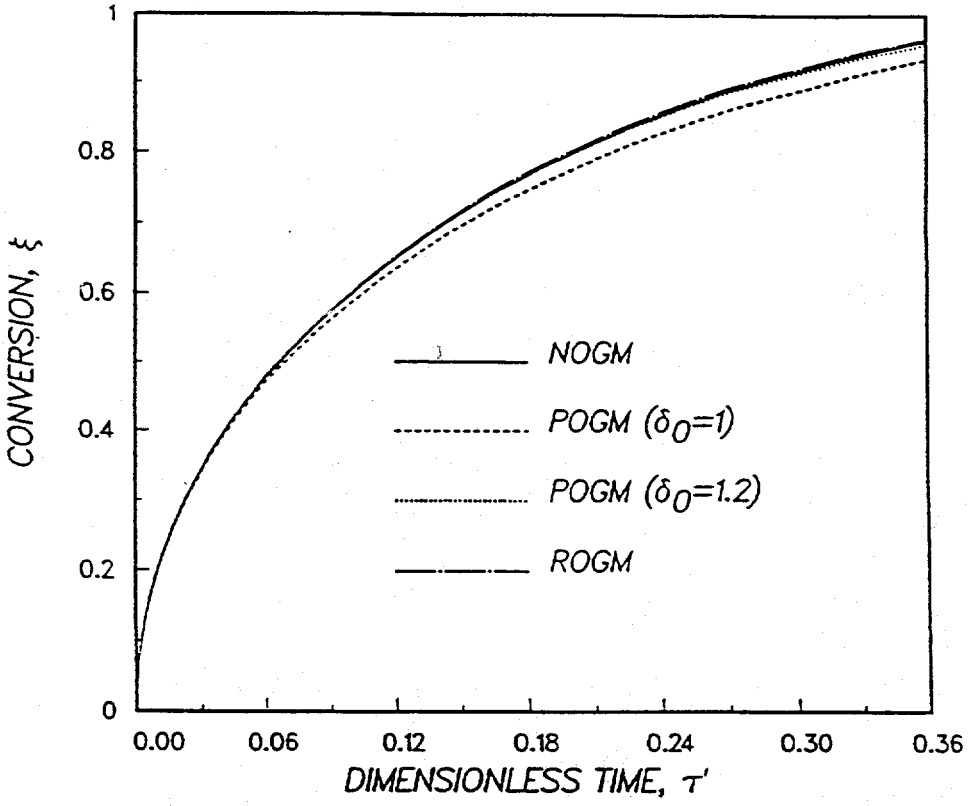

Figure 8.8. Conversion vs. time curves under reaction conditions controlled by diffusion in the product layer ($\beta = \infty$) for $Z = 2$. NOGM: nonoverlapping grains; POGM: partially overlapping grains; ROGM: randomly overlapping grains.

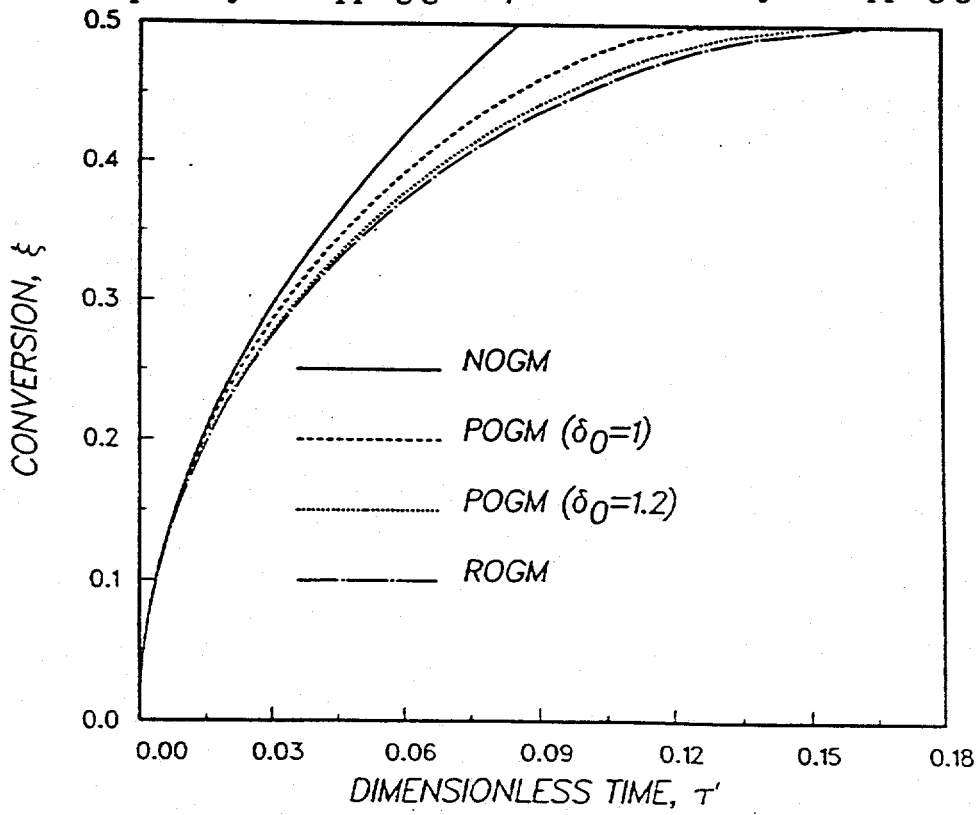

Figure 8.9. Conversion vs. time curves under reaction conditions controlled by diffusion in the product layer ($\beta = \infty$) for $Z = 3$. NOGM: nonoverlapping grains; POGM: partially overlapping grains; ROGM: randomly overlapping grains.

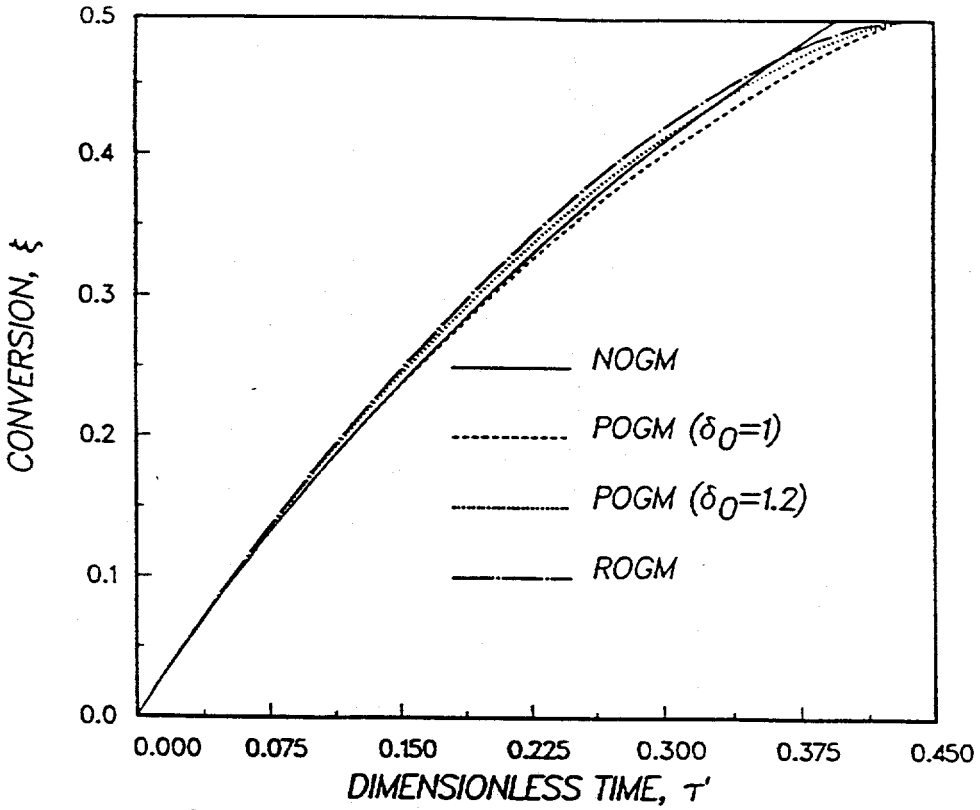

Figure 8.10. Conversion vs. time curves under reaction conditions where both kinetics and diffusion in the product layer are important ($\beta = 1$) for $Z = 3$. NOGM: nonoverlapping grains; POGM: partially overlapping grains; ROGM: randomly overlapping grains.

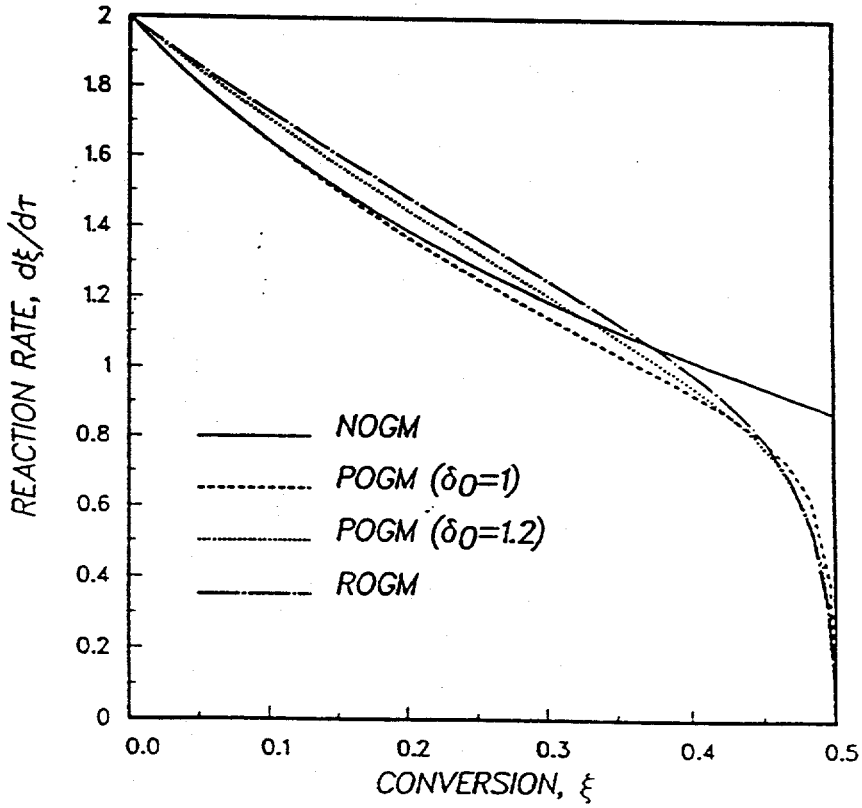

Figure 8.11. Variation of the reaction rate $(\frac{d\xi}{d\tau})$ with the concentration for the cases of Fig. 8.10.

Z increases and the product layer becomes thicker, eventually offsetting the effect of the smaller reaction surface areas. The results of Fig. 8.9 for the NOGM and ROGM cases are qualitatively similar to those presented by Sotirchos and Yu (1988) for the CaO-SO_2 reaction. Introducing the values used by Sotirchos and Yu for the CaO-SO_2 reaction in the definition of β (Eq. (8.18b)), we find that in their computations β was equal to 141.

Results for a case in which both intrinsic kinetics and diffusion through the product layer are important are shown in Fig. 8.10 for $\beta = 1$ and $Z = 3$. Both S_r and S_p are important in this case, and as a result, the conversion vs. time trajectories for the various patterns of grain overlapping differ less than the corresponding curves in Figs. 8.7 and 8.9. The evolution of the conversion in Fig. 8.10 may be more easily followed and better understood by examining the variation of the reaction rate $(d\xi/d\tau)$ with the conversion, shown in Fig. 8.11. Since nonoverlapping grains and partially overlapping grains with $\delta_0 = 1$ have the same and the smallest reaction surface area at all conversions, their reaction rates and, hence, conversions are smaller than those of the others and practically indistinguishable of each other at low conversions. As the conversion increases and the product layer thickens, diffusion in the product layer plays a more important role. Thus, the model of nonoverlapping grains (NOGM) that has the largest pore surface area starts to react faster and eventually reaches higher conversions than the other models.

8.3. Results Under Internal Diffusional Limitations

A model for intraparticle diffusion and reaction is needed in addition to the structural model if the gas-solid reaction occurs in the presence of significant concentration gradients. For small concentration of gaseous reactant and under isothermal conditions, the intraparticle diffusion and reaction model can be written, in dimensionless quantities and for spherical particles, in the following form:

$$\frac{\omega \partial(\epsilon_p x)}{\partial \tau} = \frac{1}{\Phi^2}\frac{1}{\rho^2}\frac{\partial}{\partial \rho}\left(\rho^2 \frac{\partial}{\partial \rho}(\delta^e x)\right) - \nu_A \kappa_v x \tag{8.23}$$

$$\frac{\partial \xi}{\partial \tau} = \frac{1}{(1-\epsilon_0)}\kappa_v x \tag{8.24}$$

$$\frac{\partial x}{\partial \rho} = 0|_{\rho=0};\ \frac{Sh^e}{\delta^e}(1-x) = \frac{\partial x}{\partial \rho}|_{\rho=1} \qquad (8.25a,b)$$

$$\rho = \frac{r}{a};\ x = \frac{c_p}{c_f};\ \delta^e = \frac{D^e}{D_0^e};\ \kappa_v = \frac{k_v}{k_{v0}};\ \omega = v_S c_f; \qquad (8.26a-e)$$

$$\tau = v_S k_s S_0 \int_0^t c_f dt';\ \Phi^2 = a^2 \frac{k_s S_0}{D_0^e};\ Sh^e = \frac{k_g a}{D_0^e} \qquad (8.27a-c)$$

c_f is the concentration in the bulk of the gas phase, a is the radius of the particle, r is the distance from the center of the particle, and k_g is the mass transfer coefficient.

The intraparticle effective diffusivity, D^e, and the volume-based reaction rate constant, k_v, are functions of the local conversion. It follows from Eqs. (8.12) and (8.15) that κ_v $(= k_v/k_{v0})$ is given by the equation

$$\kappa_v = \frac{S_r/S_0}{1+\beta(S_r/S_0)} \int_{y_r}^{y_p} \frac{dy}{S(R)/S_0} \qquad (8.28)$$

The effective diffusion coefficient is obtained from the well-known additivity-of-resistances (Bosanquet) formula, i.e.,

$$\frac{1}{D^e} = \frac{1}{D_K^e} + \frac{1}{D_B^e} \qquad (8.29)$$

Recent Monte Carlo computations of effective diffusivities in fibrous media by Tomadakis and Sotirchos (1991b) have shown that Eq. (8.29) provides an excellent approximation to D^e over the whole diffusion regime. The Knudsen, D_K^e, and bulk, D_B^e, effective diffusivities are given by the equations

$$D_B^e = \frac{\epsilon}{\eta_B}\mathcal{D};\ D_K^e = \frac{\epsilon}{\eta_K} D_K(2\epsilon_p/S_p) \qquad (8.30a,b)$$

$D_K(2\epsilon_p/S_p)$ is the Knudsen diffusivity in a cylindrical capillary of radius $(2\epsilon_p/S_p)$. In order to simplify the analysis of the results, it will be assumed that the tortuosity factors, η_B and η_K, are the same and independent of the porosity. The consequences of this assumption will be discussed later during the presentation of some numerical results for the ZnO-H_2S reaction.

Eqs. (8.28)-(8.30) and the solution of the structural model can be used to determine the variation of κ_v and δ^e $(= D^e/D_0^e)$ with the local conversion, ξ. With the functional dependence of these two parameters of the conversion known, the equations of the intraparticle diffusion and reaction model (Eqs. (8.23)-(8.25)) can be solved by using some discretization scheme to convert them into a system of ordinary differential equations and subsequent integration in time. For the results presented in this study, discretization was carried out using B-spline interpolation and collations (De Boor, 1978) and the resulting set of ordinary differential equations was integrated using a Gear-type solver (Gear, 1971).

With the initial bulk to Knudsen diffusivity ratio fixed, three additional parameters are involved in the diffusion and reaction model: Φ^2, Sh^e, and ω. Since the diffusion coefficient in the intraparticle space much smaller than that in the bulk, the Sherwood number (see Eq. (8.27c)) is usually a very large number, and as a result, the concentration at the surface of the particles is equal to that in the bulk, i.e., $x|_{\rho=1} = 1$. Under the typical operating conditions encountered in most gas-solid reaction (e.g., hot gas and flue gas desulfurization) the value of ω varies in the range of $10^{-6} - 10^{-8}$. The time constant for diffusion in the intraparticle space (Eq. (8.23)) is thus much smaller than that associated with structural changes in the reacting solid (Eq. (8.24)), and consequently, the exact value of ω has practically no effect on the results of the diffusion and reaction model (pseudosteady-state approximation). It can be argued, therefore, that the initial Thiele modulus is the only parameter of practical significance encountered in the dimensionless form of the intraparticle model.

Fig. 8.12 presents the effects of intraparticle diffusion on the conversion vs. time results for a solid reacting in the Knudsen diffusion regime ($D_K^e << D_B^e$) with $\beta = 1$ and $Z = 3$, whose corresponding conversion evolution curves in the absence of intraparticle diffusion resistance are given in Fig. 8.10. The analogous results for the case with $\beta = \infty$ (Fig. 8.9), where local reaction and structure evolution is controlled by diffusion in the product layer, are shown in Fig. 8.13. Since $\beta \to \infty$ implies that $k_s \to \infty$, it is again necessary to modify the definition of all dimensionless parameters and variables (namely, τ, Φ^2, and k_v) that involve k_s. This is done using the equation $Q' = \lim_{k_s \to \infty} \frac{Q}{\beta}$, with Q representing τ, Φ^2, or κ_v. Thus, τ' is given by Eq. (8.22), with c_f in the place of c_p, and

$\Phi'^2 = a^2 \frac{D_P S_0^2}{\nu_A D_0^e}$. The average conversion, $\bar{\xi}$, of Figs. 8.12 and 8.13 is defined as

$$\bar{\xi} = \int_0^1 \xi d\rho^3 \tag{8.31}$$

The results of Figs. 8.12 and 8.13 were obtained by assuming that complete pore closure at the external surface takes place when the local conversion becomes equal to 0.49 – the maximum conversion possible is 0.50. Thus, notice that no reaction takes place in Figs. 8.12 and 8.13, that is, the conversion remains unchanged, after the time that corresponds to 0.49 conversion, for each case, in Figs. 8.10 and 8.9, respectively.

Comparison of the conversion trajectories of Fig. 8.12 with those of Fig. 8.10 shows that the effects of grain overlapping on the predictions of the overall model (structure evolution and diffusion and reaction) become stronger as the Thiele modulus increases and the intraparticle diffusional limitations intensify. Similar conclusions are reached by comparing the various conversion vs. time curves in Figs. 8.13 and 8.9. The most noteworthy observation from the results of Figs. 8.12 and 8.13 is that in the presence of intraparticle diffusional limitations the maximum conversion reached by the reacting particles decreases with decreasing grain overlapping although the observed behavior in the kinetically controlled regime is different and in the case of $Z = 3$ exactly the opposite. This behavior can be explained with the help of Fig. 8.14 which presents the variation of the effective Knudsen diffusivity with the conversion for the four patterns of grain overlapping. It is seen that the effective diffusion coefficient decreases with increasing grain overlapping – since D_K^e is proportional to $(1/S_p)$ and S_p increases with increasing overlapping (see Figs. 8.4 and 8.6). The intraparticle concentration and, hence, conversion gradients become larger as the grains are permitted to overlap more, and therefore, smaller average conversion is reached by the particles when plugging of the opening at their external surface takes place. Under strong internal diffusional limitations (*e.g.*, $\Phi^2 = 10$), the average conversion decreases with increasing grain overlapping at all reaction times. If diffusion takes place in the bulk diffusion regime at all conversion levels, the effective diffusion coefficient will be independent of the extent of grain overlapping (for tortuosity factors depending on the porosity only), and consequently, the effects of the intraparticle diffusional limitations on

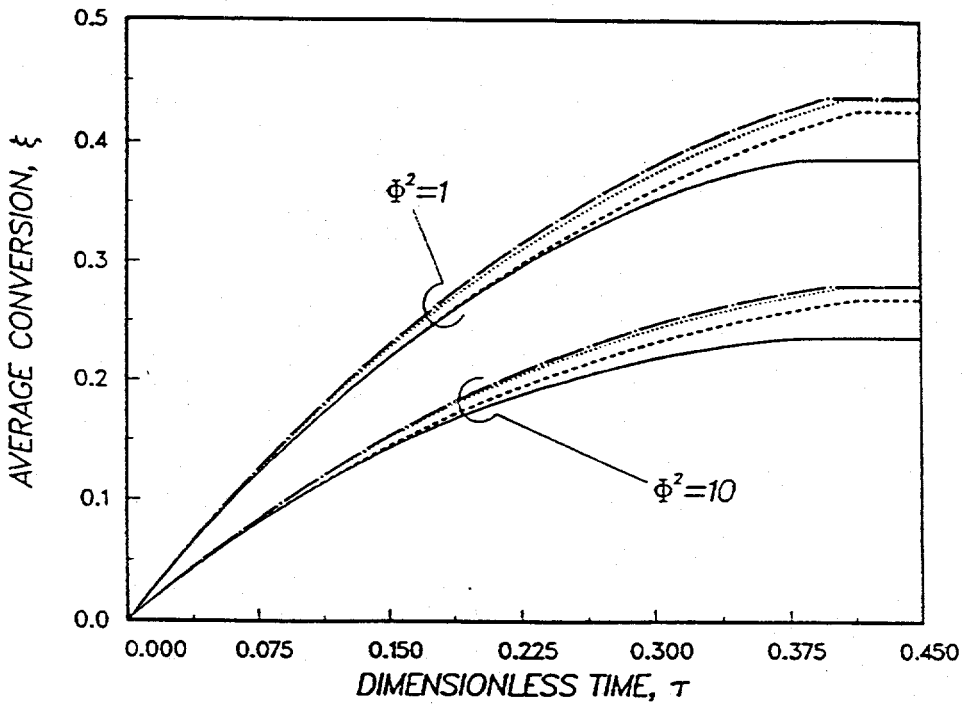

Figure 8.12. Average conversion vs. time curves under diffusional limitations in the intraparticle space for $\beta = 1$ and $Z = 3$ (see Fig. 8.10). $\omega = 10^{-7}$; $Sh^e = \infty$. ———: nonoverlapping grains (NOGM); – – –: partially overlapping grains (POGM) with δ_0=1; ·····: partially overlapping grains (POGM) with δ=1.2; –·–: randomly overlapping grains (ROGM).

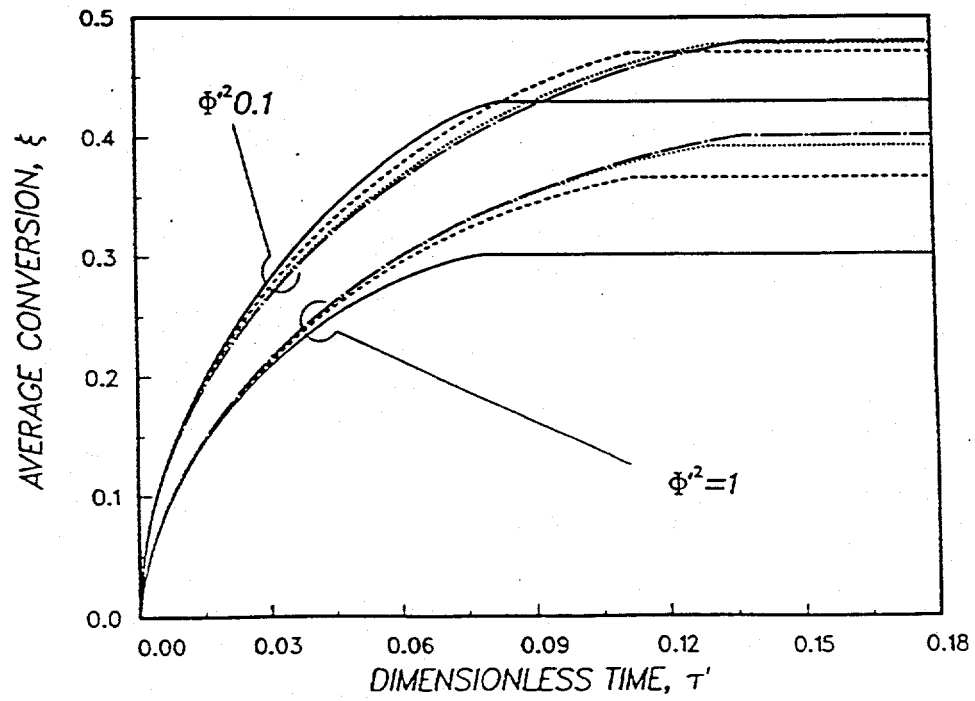

Figure 8.13. Average conversion vs. time curves under diffusional limitations in the intraparticle space for ($\beta = \infty$) and $Z = 3$ (see Fig. 8.9). $\omega = 10^{-7}$; $Sh^e = \infty$. ———: nonoverlapping grains (NOGM); – · – –: partially overlapping grains (POGM) with δ_0=1; ·····: partially overlapping grains (POGM) with δ=1.2; –·–: randomly overlapping grains (ROGM).

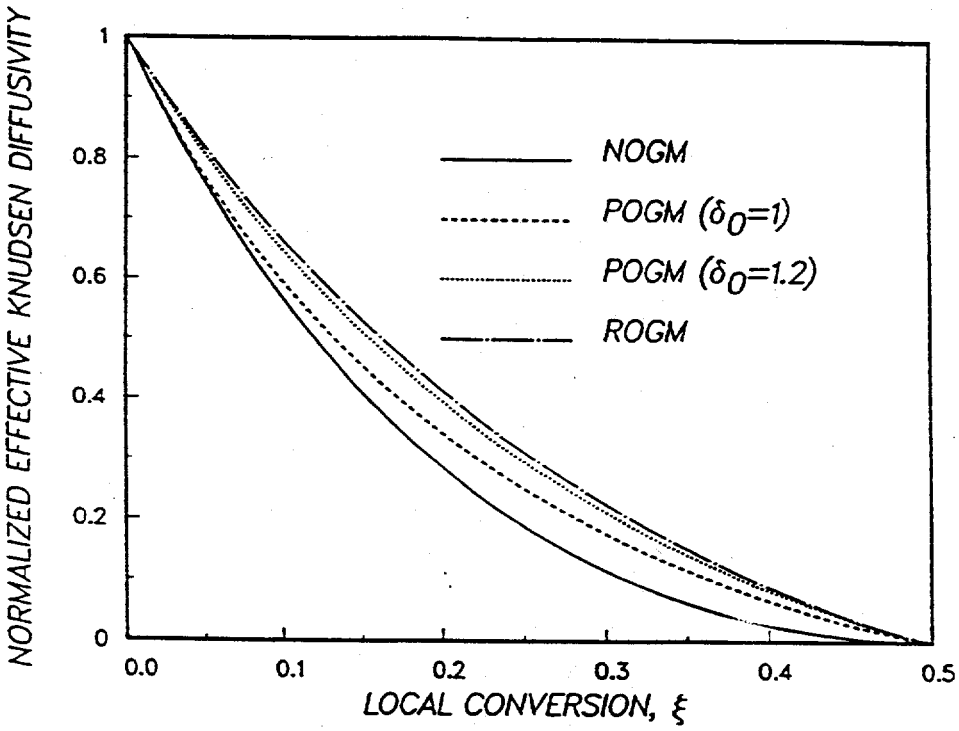

Figure 8.14. Variation of the normalized effective Knudsen diffusivity (D^e/D_0^e) with the conversion for $Z = 3$.

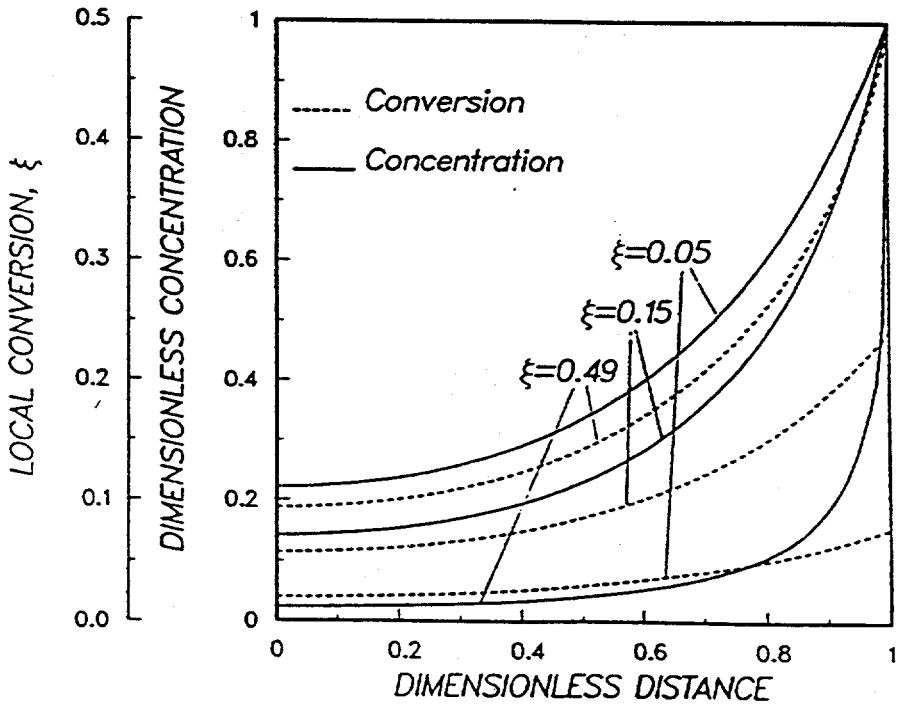

Figure 8.15. Typical concentration and conversion profiles in the interior of the particles. $\beta = 1$; Z=3; $\delta_0 = 1$; $\Phi^2 = 10$.

the conversion vs. time curves will be qualitative different from those of Figs. 8.12 and 8.13. However, actual processes are expected to behave more like the cases of Figs. 8.12 and 8.13 since even if diffusion initially occurs in the bulk diffusion regime, the decreasing average pore opening ($\frac{4\epsilon_p}{S_p}$) will eventually bring it under Knudsen diffusion control.

Typical conversion and gaseous reactant concentration profiles in the interior of the reacting particles are shown in Fig. 8.15 for the case of Fig. 8.12 with $\delta_0 = 1$ (partially overlapping grains) and $\Phi^2 = 10$. It is seen that because of the decreasing intraparticle effective diffusivity with the local conversion, both profiles become steeper with the progress of the reaction. The evolution of the conversion and concentration profiles for the other cases of Fig. 8.12 and 8.13 is qualitatively similar to that shown in Fig. 8.15.

8.4. Application to the Reaction of ZnO Sorbents with H_2S

In order to demonstrate the flexibility of the partially overlapping grain model, in comparison to that of the two extremes of non- and randomly overlapping grains, we apply in this section the model to some experimental reactivity evolution data for the reaction of a zinc oxide sorbent (sorbent G-72D of United Ctalysts) with H_2S. The physical structure of the solid was characterized by mercury porosimetry, gas adsorption, and nitrogen pycnometry. The sorbent has $\epsilon_0 = 0.51$, $v_s = 17\ cm^3/gmol$, $Z = 1.56$ and $S_0 = 27\ m^2/g$. (The v_s and Z values were estimated using the composition of the sorbent.)

The predictions of the diffusion, reaction, and structure evolution model of this study for nonoverlapping (NOGM) and partially overlapping (POGM) with $\delta_0 = 1$ grains are compared in Fig. 8.16 with experimental data for the reaction of ZnO particles (four size ranges) with 0.5% H_2S in N_2 at $600°C$ (see Fig. 4.15). The arithmetic mean of the two limits of the particle size range was used as particle size in our computations, and the effective diffusivity was computed using Eqs. (8.29) and (8.30) with $\eta_B = \eta_K = 3$. On the basis of the results from the analysis of the experimental data using the generalized random pore model, the product layer diffusivity (D_P) and the reaction rate constant (k_s) were set equal to $10^{-8}\ cm^2/s$ and $4.3 \times 10^{-3}\ cm/s$, respectively. The Sherwood number ($k_g a/\mathcal{D}$) was estimated using correlations for flow past spherical particles, and it was found to be almost unity for all particle sizes. In agreement with the general results of Fig. 8.12

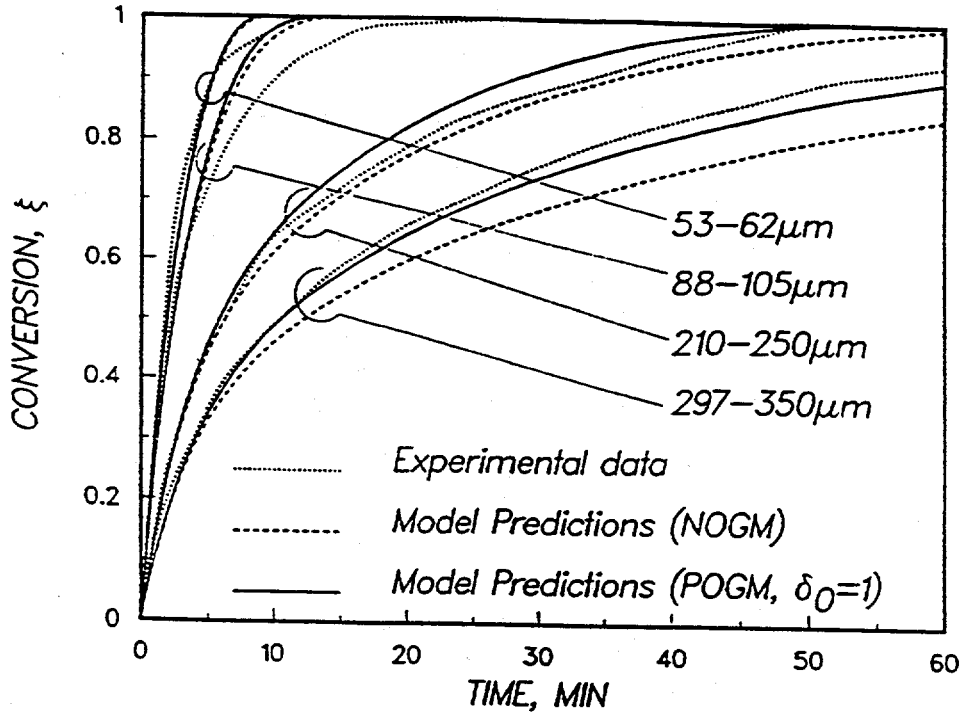

Figure 8.16. Comparison of experimental conversion vs. time curves for ZnO sulfidation with results predicted by the mathematical model. 600°C; 5000 ppm H_2S in N_2.

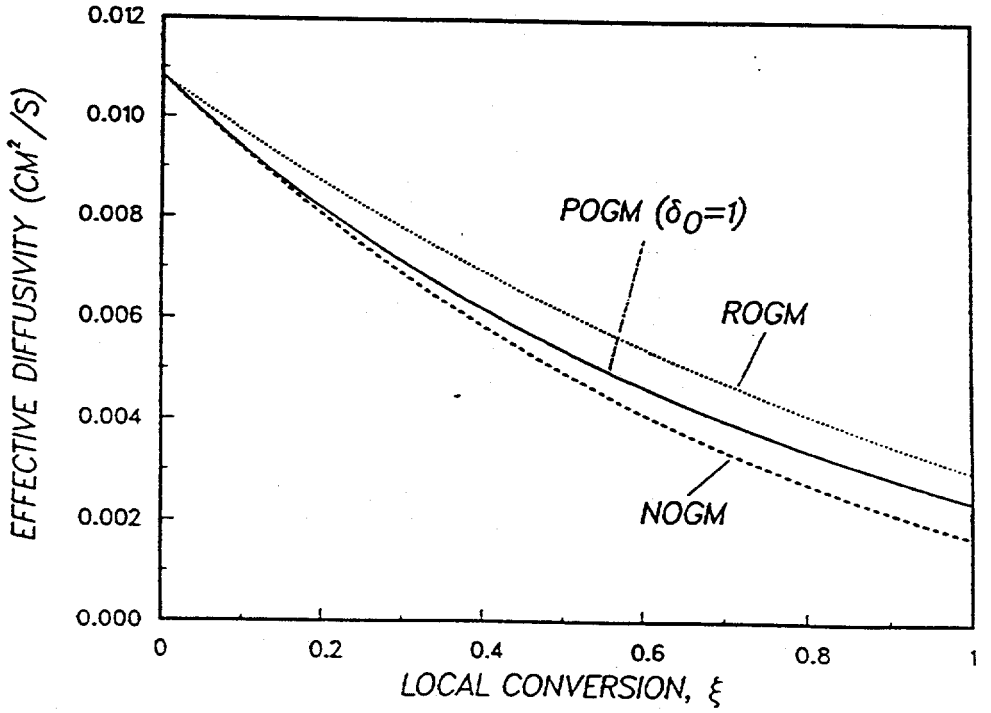

Figure 8.17. Effects of the extent of grain overlapping on the variation of the effective diffusion coefficient with the conversion of the zinc oxide sorbent of Fig. 8.16.

and 8.13, the nonoverlapping grain model is more strongly influenced by the existence of intraparticle diffusional limitations, and thus tends to underestimate the average conversion of the large particles. The main reason for this kind of behavior lies again in the variation of the effective diffusion coefficient with the conversion, shown in Fig. 8.17. Diffusion in the intraparticle space practically takes place in the Knudsen diffusion regime – the initial value of $2\epsilon_p/S_p$ is 200 Å – and therefore, the effective diffusivity at nonzero conversions increases significantly with decreasing grain overlapping.

Since the variation of the effective diffusivity with the conversion turns out to be the most important of the factors that influence the predictions of the overall model in the presence of internal diffusional limitations, the theoretical results of Fig. 8.16 are strongly affected by the formula used to follow the dependence of the effective diffusivity in the structure of the solid. A constant tortuosity factor was used to obtain the results of Fig. 8.16, but since the structure of the solid becomes more tortuous as the porosity decreases, the tortuosity factor is in general an increasing function of the porosity (Tomadakis and Sotirchos, 1991a). Use of variable (and possibly different) tortuosity factors for the Knudsen and bulk diffusion regimes is not expected to change the qualitative trend seen in Fig. 8.17 although the δ_0 value that gives the best agreement between model and experiment will most probably be different.

8.5. Summary and Further Remarks

A mathematical model was developed for gas-solid reaction occurring in porous media whose structure can be visualized as an assemblage of partially overlapping (penetrable) spherical grains of uniform radius, each consisting of a spherical hard core, of the same radius for all grains, and a soft penetrable shell. The development of the diffusion, reaction, and structure evolution model was based on the randomly overlapping grain model of Sotirchos and Yu (1988) and the expressions derived by Rikvold and Stell (1985a) – on the basis of the scaled-particle theory of hard sphere fluids of Reiss et al. (1959) – for the porosities and surface areas of partially penetrable spheres. The partially overlapping grain model is considerably more flexible than the structural models that correspond to the extreme cases of nonoverlapping and partially overlapping grains. By varying the hard

core to grain radius ratio, it is possible to cover the whole space between these two extremes for a solid of given porosity and internal surface area.

A detailed parametric sensitivity analysis of the mathematical model, in terms of the various dimensionless parameters encountered in, was carried out for the case of gas-solid reactions with solid product. The flexibility of the mathematical model was demonstrated by applying it to a set of experimental data for the ZnO-H_2O reaction. Our results showed that the effects of the extent of grain overlapping on the evolution of the overall reactivity of the solid with time are influenced in a rather complex fashion by the diffusional limitations in the product layer and in the intraparticle space. For fixed values of initial porosity and internal surface area, the conversion reached by the reacting solid increases with increasing grain overlapping in the absence of diffusion limitations, because of increasing reaction surface area. However, as the grains are permitted to overlap more, the pore surface area decreases, and this can lead to lower local reaction rates under strong diffusional limitations in the product layer. Smaller pore surface areas usually imply larger effective diffusion coefficients in the Knudsen regime, and a result, the conversion reached by the reacting solid particles in the presence of strong intraparticle diffusional limitations decreases, in general, with decreasing grain overlapping.

We mentioned in the introductory section of our paper that a partially overlapping ('sintered') sphere model was developed by Lindner and Simonsson (1981) (PSSM model). The development of this model was based on the assumption that the structure of the unreacted solid could be represented by an aggregate of spherical grains in which each grain is in contact with n, on the average, other grains of the same initial radius, r_0. The 'degree of sintering' was given by the distance d from the center to the plane of contact. For a given d/r_0 and ϵ_0, n was determined by requiring that the model be consistent with the physical constraint of having zero surface area at zero porosity. Fig. 8.18 compares the variation of the internal surface area with the porosity of a structure of initial nonoverlapping grains with $\epsilon_0 = 0.5$ predicted by the Lindner and Simonsson model ($d/r_0 = 1$; $n = 5.57$) and the partially overlapping grain model ($\delta_0 = 1$). Since both models start with a structure of unconsolidated grains, the internal surface areas they predict for $\epsilon > \epsilon_0$ are identical, but significant differences are observed between the surface areas predicted by the two models

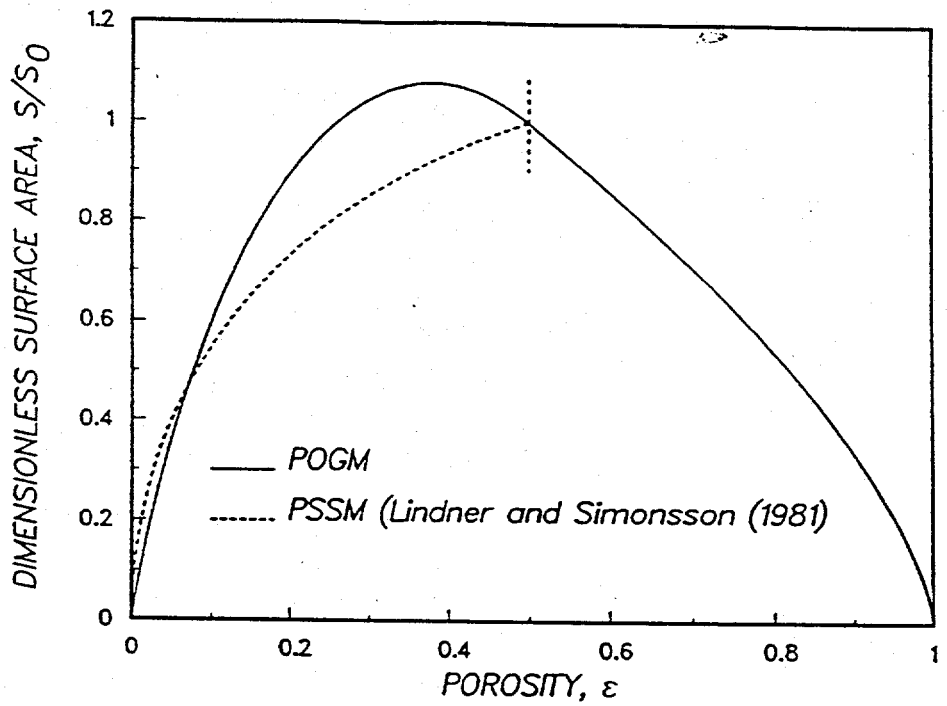

Figure 8.18. Comparison of the surface area vs. conversion curve predicted by the partially overlapping grain model (POGM) developed in this study for ε_0=0.5 and δ_0=1 with that given by the partially sintered sphere model (PSSM) of Lindner and Simonsson (1981) for the equivalent values of ε_0=0.5 and d/r_0=1. Both models predict the same evolution of S for $\varepsilon > \varepsilon_0$.

below ϵ_0. Since these surface areas are the pore surface areas for $Z > 1$, the conversion vs. time results of t two model: n the presence of diffusional limitations (in the product layer or in the intra rticle space, are expected to differ significantly.

It can be shown using Eqs. (8.19), (8.21), and (8.23) in the paper by Lindner and Simonsson that the internal surface area for $d/r_0 = 1$ decreases with decreasing porosity for $n > 4$, which corresponds to $\epsilon_0 > 2/3$. On the other hand, the internal surface area given by Eq. (8.6) (in our study) for partially overlapping grains with $\delta_0 = 1$ goes through a maximum for all ϵ_0. Thus, the only way to make the internal surface area vs. conversion curve of the PSSM model get closer to that of the POGM model for $\epsilon < \epsilon_0$ in Fig. 8.18 is to use in the PSSM model $d/r_0 > 1$. The pore surface of the PSSM model will then evolve as that of nonoverlapping grains until the point $d/r = 1$. (At $d/r = 1$ the derivative of the surface area vs. porosity curve is discontinuous because at this point each grain in the PSSM model comes in contact with a finite number of grains.)

8.6. Notation

Symbols that do not appear here are defined in the text.

a radius of the particle, cm

c_f gas concentration in the bulk, mol/cm^3

c_p gas concentration in the pores, mol/cm^3

c_r gas concentration at the reaction surface, mol/cm^3

$\mathcal{D}$ bulk diffusion coefficient, cm^2/s

D^e effective diffusion coefficient, cm^2/s

D_B^e effective bulk diffusion coefficient, cm^2/s

D_K Knudsen diffusion coefficient in a pore, cm^2/s

D_K^e effective Knudsen diffusion coefficient, cm^2/s

D_P diffusion coefficient in the product layer, cm^2/s

k_s reaction rate constant, cm/s

k_g mass transfer coefficient, cm/s

k_v local volume-based reaction rate constant, s^{-1}

n number of grains per unit volume

r radial distance in a particle, cm

R grain radius, cm

R_c hard core radius, cm

$\mathcal{R}_s$ reaction rate per unit surface, $mol/cm^2/s$

S internal surface area of a two-phase structure, cm^2/cm^3

Sh^e Sherwood number (see Eq. (8.27c))

t time, s

T temperature, K

v_i specific molar volume of solid i, cm^3/mol

x dimensionless concentration in the particle

y dimensionless radial distance in the grains

Z stoichiometric volume ratio ($\nu_P v_P / v_S$)

Greek Letters

β dimensionless parameter (Eq. 8.18b)

δ grain growth variable

δ^e dimensionless effective diffusivity

ϵ porosity of a grain structure

ϵ_c hard core porosity

η_B tortuosity factor for bulk diffusion

η_K tortuosity factor for Knudsen diffusion

κ_v dimensionless reaction rate constant ($= k_v/k_{v0}$)

ν_A stoichiometric coefficient of the reactive gas

ν_P stoichiometric coefficient of the solid reactant

ξ local solid conversion

$\bar{\xi}$ average solid conversion in a particle

ρ dimensionless distance in a particle

τ dimensionless time ($= v_S k_s S_0^2 \int_0^t (c_f \text{ or } c_p) dt'$)

τ' dimensionless time ($= (v_S/\nu_A) D_P S_0^2 \int_0^t (c_f \text{ or } c_p) dt'$)

Φ^2 initial Thiele modulus ($= a^2 k_s S_0 / D_0^e$)

$\Phi^{2'}$ modified initial Thiele modulus ($= a^2 D_P S_0^2 / (\nu_A D_0^e)$)

ω dimensionless parameter ($= c_f v_S$)

Subscripts

0 refers to t = 0 or to properties of the unreacted grain structure

f refers to the bulk gas phase

p refers to the pore surface or to the grains forming the pore surface

r refers to the reaction surface or to the grains forming the reaction surface

P refers to the solid product

S refers to the solid reactant

8.7. Literature References

Alvfors, P., Svedberg G., "Modelling of the Sulfation of Calcined Limestone and Dolomite – a Gas-Solid Reaction with Structural Changes in the Presence of Inert Solids," Chem. Eng. Sci., **43**, 1183-1193 (1988).

Barner, H.E., Mantel, C.L., "Kinetics of Hydrogen Reduction of Manganese Dioxide," Ind. Eng. Chem. Process Des. Dev., **7**, 285-294 (1968).

Bhatia, S.K., "Modeling the Pore Structure of Coal," AIChE J., **33**, 1707-1718 (1987).

De Boor, C., *A Practical Guide to Splines*, Springer-Verlag, New York (1978).

Gear, C.W., *Numerical Initial Value Problems in Ordinary Differential Equations*, Prentice Hall, Englewood Cliffs, NJ (1971).

Georgakis, C., Chang, C.W., Szekely, J., "A Changing Grain Size Model for Gas-Solid Reactions," Chem. Eng. Sci., 1072-1075 (1979).

Lindner, B., Simonsson, D., "Comparison of Structural Models for Gas-Solid Reactions in Porous Solids Undergoing Structural Changes," Chem. Eng. Sci., **36**, 1519-1527 (1981).

Ramachandran, P.A., Doraiswamy, L.K., "Modeling of Noncatalytic Gas-Solid Reactions," AIChE J., **28**, 881-900 (1982).

Ranade, P.V., Harrison, D.P., "The Variable Property Grain Model Applied to the Zinc Oxide-Hydrogen Sulfide Reaction," Chem. Eng. Sci., **36**, 1079-1089 (1981).

Reiss, H., Frisch, H.L., Lebowitz, J.L., "Statistical Mechanics of Rigid Spheres, J. Chem. Phys.," **31**, 369-380 (1959).

Rikvold, P.A., Stell, G., "Porosity and Specific Surface for Interpenetrable-Sphere Models of Two-Phase Random Media," J. Chem. Phys., **82**, 1014-1020 (1985a).

Rikvold, P.A., Stell, G., "D-Dimensional Interpenetrable-Sphere Models of Random Two-Phase Media: Microstructure and an Application to Chromatography," J. Colloid Interface Sci., **108**, 158-173 (1985b).

Sotirchos, S.V., "On a Class of Random Pore and Grain Models for Gas-Solid Reactions," Chem. Eng. Sci., **42**, 1262-1265 (1987).

Sotirchos, S.V., Yu, H.C., "Mathematical Modelling of Gas-Solid Reactions with Solid Product," Chem. Eng. Sci., **40**, 2039-2052 (1985).

Sotirchos, S.V., Yu, H.C., "Overlapping Grain Models for Gas-Solid Systems with Solid Product," Ind. Eng. Chem. Res., **27**, 836-845 (1988).

Sotirchos, S.V., Zarkanitis, S., "Pellet-Model Effects on Simulation Models for Fixed-Bed Desulfurization Reactors," AIChE J., **35**, 1137-1147 (1989).

Szekely, J., Evans, J.W., "A Structural Model for Gas-Solid Reactions with a Moving Boundary," Chem. Eng. Sci., **25**, 1091-1107 (1970).

Szekely, J., Propster, M., "A Structural Model for Gas-Solid Reactions with a Moving Boundary-V," Chem. Eng. Sci., **30**, 1049-1055 (1975).

Szekely, J., Evans, J.W., Sohn, H.Y, *Gas-Solid Reactions*, Academic Press, New York (1976).

Tomadakis, M.M., Sotirchos, S.V., "Properties and Knudsen Diffusivities of Structures of Unidirectional Fibers," AIChE J., **37** 1175-1186 (1991).

Tomadakis, M.M., Sotirchos, S.V., "Bulk and Transition Regime Diffusion in Random Fiber Structures," AIChE J., **39** (1993).

9. STEADY-STATE VS. TRANSIENT MEASUREMENT OF EFFECTIVE DIFFUSIVITIES IN POROUS MEDIA USING THE DIFFUSION-CELL METHOD

9.1. Introduction

The effective diffusivities of gases in porous media participating in gas-solid reactions, as well as their variation with the extent of the conversion of the solid for noncatalytic reactions, are among the most important parameters needed for the description of such processes. Knowledge of the effective diffusivity and its dependence on pore structure is also required in the analysis of experimental reactivity data for reactions between gases and porous solids obtained under significant diffusional limitations in the pore space. The particle-bed and the diffusion-cell method are most commonly used for the measurement of effective diffusion coefficients in porous media. In the particle-bed (or pulse-chromatographic) method, the effective diffusivity is extracted from the response of the exit concentration of a tracer gas in a packed bed of particles of the porous solid to a pulse change in the inlet concentration (Kucera, 1965; Schneider and Smith, 1968; Shah and Ruthven, 1977). Among the most important advantages of the particle-bed method over the diffusion cell method is that it can also be employed for porous media available in particle form only. Moment analysis of the response of the packed bed is the preferred method in the literature for estimation of the effective diffusivity from pulse-chromatographic data inasmuch as analytical expressions for the dependence of the moments of the response on the parameters of process can be derived if a linear convection and diffusion mathematical model is used for the bed – a reasonable approximation for low concentrations of diffusing gas.

Despite its appealing simplicity, the moments method may lead to inaccurate estimates of the effective diffusion coefficient because of the strong effect of experimental errors in the response curve (especially for large values of time) on the computed moments, and in particular on the second central moment that is usually used to estimate the effective diffusion coeffficient. An alternative method of response analysis which does not present this disadvantage is the time-domain method, in which the effective diffusion coefficient and other transport parameters of the system (the axial dispersion coefficient,

for instance) are estimated by minimizing the difference between the experimental response and the response predicted by the mathematical model, usually, the integral square error (Boersma-Klein and Moulijn, 1979). Some of the problems met in the moments method can be avoided in the time-domain method by using only the part of the response that is free of large relative experimental errors.

In the diffusion-cell method, first proposed by Wicke and Kallenbach, 1941), streams of a binary mixture of a carrier gas and of the species whose diffusion coefficient we seek to determine are flown over the two sides of a pellet (slab-shaped sample) of the porous medium. The experiment is carried out under isobaric conditions because, otherwise, a flux model for simultaneous convection and diffusion in porous media has to be used to analyze the experimental data and isolate the diffusive contribution to the total mass transport flux. In contrast to the particle-bed method, diffusion-cell measurements can be carried out both under steady-state and transient conditions (Smith, 1981). In the steady-state version of the experiment, the mass transport flux is determined by measuring the concentration of the streams leaving the two sides of the diffusion cell and performing a simple mass balance on the tracer gas. When transient operation of the diffusion cell is employed, a concentration pulse is introduced in the stream that flows over one side of the porous sample, and the response of the concentration of the tracer gas in the exit stream of the other side is monitored, as in the case of the particle-bed method (Suzuki and Smith, 1972); Dogu and Smith, 1975); Baiker et al., 1982). Because of its simplicity, the moments method is again the preferred method of data analysis for transient diffusion-cell experiments. The sensitivity of the moments method to experimental errors in the response (noise, baseline shift, etc.) is not as large as that of particle-bed data because only the zero and first moments are now needed to get the effective diffusivity. Nevertheless, a time-domain method should again be preferred. Since only the zero and first moments of the experimental and theoretical responses are matched, the response curves in the time domain can be considerably different from each other.

It has been reported in the literature that effective diffusivities extracted from steady-state experiments in a diffusion cell may differ significantly from the values obtained from the analysis of pulse response data from particle-bed or diffusion-cell arrangements, even if

the same unit (i.e., diffusion cell) is used to obtain the steady-state and dynamic response data (McGreavy and Siddiqui, 1980; Baiker et al., 1982). Several explanations have been proposed to account for this discrepancy. These include: the existence of dead-end pores which should participate in the diffusion process under transient conditions but not under steady-state conditions; the effects of nonequilibrium adsorption, while equilibrated adsorption is usually assumed in the construction of the transient model; the effects of surface diffusion; and the effects of the dynamics of the entry and exit sections of the diffusion-cell or particle-bed apparatus, including those of the detectors used for concentration measurement, on the overall dynamics on the process and, hence, on the moments of the transient response to a concentration pulse. To all these explanations, one should add the possibility of erroneous determination of the moments of the response because of experimental errors.

Cui et al. (1989, 1990) recently showed that even in the absence of dead-end pores, surface diffusion and adsorption equilibration effects, and entry and exit section dynamics effects, effective diffusivities obtained from steady-state diffusion-cell experiments will always be different for solids with a distribution of pore size from those obtained from pulse-chromatographic (particle-bed) data through moments matching. The main reason for this difference is the use of a pseudohomogeneous model, that is, the use of a single effective diffusion coefficient to describe diffusion in an intrinsically inhomogeneous system which comprises subsystems (pores) of different diffusional resistances. For a simple pore structure consisting of parallel, noninteracting pores, Cui et al. showed that experiments under steady-state conditions yield, for diffusion parallel to the pores and in the absence of adsorption, the Johnson and Stewart, 1965) effective diffusivity, viz.,

$$D_s^e = \varepsilon \int_R D(R)\gamma(R)dR \tag{9.1}$$

$D(R)$ is the diffusivity in pores of radius R, ε is the porosity, and $\gamma(R)$ is the normalized porosity density function, that is, $\gamma(R)dR$ is the porosity fraction that belongs to pores with radius in the range $[R, R+dR]$. Matching of the moments of the transient responses of the inhomogeneous and homogeneous models, on the other hand, yields an effective

diffusivity given by

$$D_i^e = \varepsilon[\int_R \frac{1}{D(R)}\gamma(R)dR]^{-1} \tag{9.2}$$

Eqs. (9.1) and (9.2) give the same effective diffusivity only for solids with pores of uniform size. For solids with distributed pore size, the effective diffusivity of Eq. (9.2) is always smaller than that given by Eq. (9.1), by more than an order of magnitude for broad pore size distributions. Cui et al. (1989) postulated that for pore network models more complex than the parallel, noninteracting pore network, the differences between the steady-state (diffusion-cell) and transient (particle-bed) diffusivities for distributed pore size solids would undoubtedly be larger than those between the predictions of Eqs. (9.1) and (9.2).

The measurement of effective diffusivities using the diffusion-cell method under stationary and nonstationary conditions was examined by Burghardt et al. (1988) for bidisperse porous structures consisting of through macropores and dead-end micropores. Three different pore structures were considered in their analysis: a globural structure consisting of compacted microporous particles, a capillary structure with dead-end micropores emanating from the surface of a macroporous network, and a structure with dead-end micropores situated parallel to through macropores. It was found that the diffusion process in the dead-end micropores has no effect on the zero and first moments of the response of the diffusion cell, and as a result, matching of the first two moments yields the steady-state effective diffusivity. The micropore effective diffusivity appears in the second moment of the response, and the effective diffusivities obtained by second moment matching are lower than the value obtained from the stationary experiment. The theoretical conclusions of Burghardt et al. were in excellent agreement with their own experimental data for five different porous pellets.

An analysis of the relation between the effective diffusivities obtained from transient and steady-state mass transport experiments for solids with a pore size distribution using the diffusion-cell method is presented in this paper. The simple network of parallel (through) pores that was employed by Cui et al. (1989, 1990) in their study of the particle-bed method is used to represent the structure of the solid, and two models, differing in the complexity of the boundary conditions, are used to describe the diffusion-cell process. It is shown that in the case of transient diffusion-cell experiments, moment analysis of the tran-

sient responses (i.e., zero or first moment matching) yields the same result as steady-state diffusion-cell experiments. Despite having the same zero and first moments, the impulse responses of the inhomogeneous and pseudohomogeneous models differ significantly, but if a time-domain parameter estimation procedure is employed, the obtained effective diffusivity is, in general, larger than that resulting from steady-state experiments. It is finally shown that for more realistic pore structures, that is, pore structures exhibiting pore interlinking between the two sides of the solid sample, the difference between the responses of the homogeneous and inhomogeneous model, for the same zero and first moments, is smaller and approaches zero as the extent of pore communication is increased.

9.2. Description of the Diffusion-Cell System

A schematic diagram of a diffusion-cell arrangement is shown in Fig. 9.1. F_i are the flow rates of the gaseous streams that flow over the two sides of the porous slab, c_i are the concentrations of the diffusing species (solute) in the solute-carrier mixtures, V_i are the volumes of the dead-space regions ('mixing' chambers) next to the two faces of the porous slab, l is the slab thickness, and A is the cross-sectional area of the slab perpendicularly to the direction of diffusion, viz., the x-direction. In order to facilitate the analysis and interpretation of the results and avoid the use of a tortuosity factor, it is assumed that the pore space of the solid can be represented by an assemblage of cylindrical pores, arranged parallel to the direction of diffusion. The population of pores is described using the distribution density $\varepsilon(R)$, with $\varepsilon(R)dR$ being the porosity due to pores with size in the range $[R, R+dR]$. The normalized form of $\varepsilon(R)$ is denoted by $\gamma(R)$.

If a homogeneous model is used to describe the diffusion process in the porous medium, the mass balance for the solute in the solid in the absence of chemical reaction takes the form

$$\varepsilon \frac{\partial c_h}{\partial t} + \frac{\partial N_h}{\partial x} = 0 \tag{9.3}$$

where c and N are the concentration and flux of the solute, respectively, and subscript h is used to indicate that they refer to a homogeneous model. For a single pore of radius R,

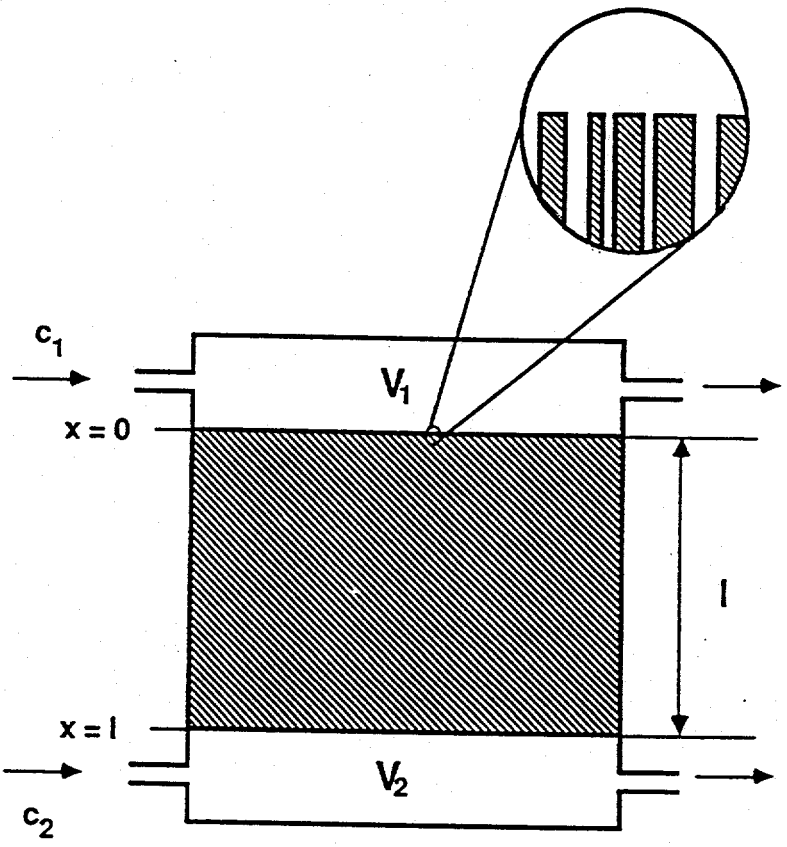

Figure 9.1: Schematic diagram of a diffusion-cell arrangement. The circled graph shows the local pore structure in enlargement.

on the other hand, the mass balance for the solute is written

$$\frac{\partial c(R)}{\partial t} + \frac{\partial N(R)}{\partial x} = 0 \tag{9.4}$$

with $c(R)$ and $N(R)$ being the concentration and flux of the solute in a pore of radius R. For small concentrations of solute and isobaric conditions, the fluxes (N_h and $N(R)$) can be related to the concentration gradients using the relations

$$N_h = -D^e \frac{\partial c_h}{\partial x}; \quad N(R) = -D(R)\frac{\partial c(R)}{\partial x} \tag{9.5a, b}$$

D^e and $D(R)$ are the diffusion coefficients of the solute in the porous medium (effective) and in a pore of radius R, respectively, both assumed independent of the concentration of the solute. Introducing Eqs. (9.5a,b) in Eqs. (9.3) and (9.4), the mass balance equations in the porous medium and in an individual pore become

$$\frac{\varepsilon \partial c_h}{\partial t} - D^e \frac{\partial^2 c_h}{\partial x^2} = 0 \tag{9.6}$$

$$\frac{\partial c(R)}{\partial t} - D(R)\frac{\partial^2 c(R)}{\partial x^2} = 0 \tag{9.7}$$

The average molar flux for the inhomogeneous system at some position x in the porous slab is obtained by averaging the flux for a single pore the same position over the pore size distribution, that is, we set

$$N_n = \int_R N(R)\varepsilon(R)dR \tag{9.8}$$

(Subscipt n is used to indicate quantities that refer to the inhomogeneous system or model.) Under steady-state conditions, we have that

$$\frac{\partial c_h}{\partial x} = \frac{\partial c(R)}{\partial x} = \frac{c_l - c_0}{l} \tag{9.9}$$

where c_0 and c_l are the concentrations of the solute at $x = 0$ and $x = l$. Equating the homogeneous and inhomogeneous model fluxes (Eqs. (9.5) and (9.8)) and using Eq. (9.9), we find that the steady-state effective diffusivity is given by

$$D_s^e = \varepsilon \int_R D(R)\gamma(R)dR \tag{9.10}$$

that is, Eq. (9.1).

9.3. Effective Diffusivities From Transient Experiments Using Moments Matching

In order to be able to extract effective diffusion coefficients from experimental data of transient experiments, a set of boundary conditions is needed to complete the mathematical model. The simplest set of boundary conditions is obtained by assuming that the volumes of the mixing chambers are negligibly small in comparison to that of the porous slab and that no flow takes place over the face of the slab at $x = l$, where measurement of the concentration response takes place. For an actual experimental arrangement, this situation corresponds to the case where a diffusion cell with a closed end is employed, the carrier-solute mixture is flown over the open end of the cell at a very high flow rate, and some concentration sensor is used to measure the concentration of the solute at the closed end (Suzuki and Smith, 1972). With these assumptions the boundary conditions take the form

$$c_h = c_0 = c_1; \quad c(R) = c_0 = c_1 \quad (\text{at } x = 0) \tag{9.11a,b}$$

$$N_h = 0; \quad N_n = 0 \quad (\text{at } x = l) \tag{9.12a,b}$$

$$c(R) = c_l, \quad \text{for all } R \quad (\text{at } x = l) \tag{9.13}$$

Eq. (9.13) states that the solute has the same concentration in all pores at the closed end of the diffusion cell. Using Eqs. (9.5) and (9.8), Eqs. (9.12) may be written in the equivalent form

$$\frac{\partial c_h}{\partial x} = 0; \quad \int_R D(R) \frac{\partial c(R)}{\partial x} \varepsilon(R) dR = 0 \tag{9.14a,b}$$

In the application of the moments method, the moments of the experimental response of a system (diffusion cell or particle bed) to some form of concentration input are set equal to those predicted by a homogeneous model for the system, and the resulting equations are used to estimate the unknown effective transport properties of the model. For the ideal case of a unit impulse (Dirac delta function) input, the moments of the response of the output, m_i, can be found from the transfer function between imput and output, $G(s)$,

using the equation

$$m_i = (-1)^i lim_{s\to 0} \frac{d^i G(s)}{ds^i} \tag{9.15}$$

It can easily be shown by taking the Laplace transform of Eqs. (9.6), (9.11a), and (9.14a) and solving the resulting equations that the transfer function for the homogeneneous model is

$$G_h(s) = \frac{1}{cosh(\sqrt{\frac{\varepsilon s}{D^e}} l)} \tag{9.16}$$

Using Eq. (9.16), we find that the zero moment of the impulse response is unity and that the first moment is given by

$$m_{1h} = \frac{\varepsilon l^2}{2D^e} \tag{9.17}$$

Similarly, solving Eqs. (9.7), (9.11b), (9.13), and (9.14b) in the s-domain we find that the transfer function for the inhomogeneous model has the form

$$G_n(s) = \frac{\int_R D(R)\sqrt{\frac{s}{D(R)}} \frac{1}{sinh(\sqrt{\frac{s}{D(R)}} l)} \varepsilon(R) dR}{\int_R D(R)\sqrt{\frac{s}{D(R)}} \frac{cosh(\sqrt{\frac{s}{D(R)}} l)}{sinh(\sqrt{\frac{s}{D(R)}} l)} \varepsilon(R) dR} \tag{9.18}$$

Using Eq. (9.16), we find that the zero moment of the impulse response of the inhomogeneous system is unity, as in the case of the homogeneous model, and that the first moment is given by the expression

$$m_{1n} = \frac{l^2}{2\int_R D(R)\gamma(R) dR} \tag{9.19}$$

Matching the first moments of the inhomogeneous ('experimental') and homogeneous model responses, i.e., setting $m_{1h} = m_{1n}$, we get

$$D_t^e = \varepsilon \int_R D(R)\gamma(R) dR \tag{9.20}$$

with subscipt t used to denote effective diffusivities estimated from dynamic data. Eq. (9.20) clearly states that the effective diffusivity obtained using the moments method is identical to that obtained from steady-state experiments.

A question that naturally arises at this point is whether this conclusion is specific to the limiting case described by the boundary conditions given by Eqs. (9.11)-(9.14) or it also applies to the more general problem depicted in Fig. 9.1. If perfect mxing is assumed

in the dead-space regions adjacent to the porous slab, the boundary conditions for the homogeneous and inhomogeneous diffusion-cell models become of the form (Burghardt and Smith, 1979)

$$V_1 \frac{\partial c_0}{\partial t} = F_1(c_1 - c_0) - AN \tag{9.21}$$

$$c_h = c_0; \quad c(R) = c_0 \quad (\text{at } x = 0) \tag{9.22a, b}$$

$$V_2 \frac{\partial c_l}{\partial t} = F_1(c_2 - c_l) + AN \tag{9.23}$$

$$c_h = c_l; \quad c(R) = c_l \quad (\text{at } x = l) \tag{9.24a, b}$$

Eqs. (9.22b) and (9.23b) state that the concentrations of the solute in all pores at $x = 0$ and $x = l$, respectively, are the same. The flux N used in Eqs. (9.21) and (9.23) is given by Eq. (9.5a) for the homogeneous model and (9.8) and (9.5b) for the inhomogeneous model.

Assuming that the same concentration of solute is present initially in both streams, solution of Eqs. (9.6), (9.21), (9.22a), (9.23), (9.24a), and (9.5a) gives for the transfer function of the homogeneous model the result

$$G_h(s) = \frac{g_{1h}}{(1 + \tau_1 s + g_{2h})(\phi + \tau_2 s + g_{2h}) - g_{1h}^2} \tag{9.25}$$

with

$$g_{1h} = \frac{A}{F_1} D^e \sqrt{\frac{\varepsilon s}{D^e}} \frac{1}{sinh(\sqrt{\frac{\varepsilon s}{D^e}} l)} \tag{9.26}$$

$$g_{2h} = \frac{A}{F_1} D^e \sqrt{\frac{\varepsilon s}{D^e}} \frac{cosh(\sqrt{\frac{\varepsilon s}{D^e}} l)}{sinh(\sqrt{\frac{\varepsilon s}{D^e}} l)} \tag{9.27}$$

$$\phi = F_2/F_1; \quad \tau_i = V_i/F_1 \tag{9.28a, b}$$

Using Eq. (9.16), we find that the zero and first moments of the impulse response of the homogeneous model are given by the relations (see also Burghardt and Smith, 1979)

$$m_{0h} = \frac{1}{1 + \phi(1 + \frac{F_1 l}{AD_e})} \tag{9.29}$$

$$m_{1h} = m_{0h}^2 [\tau_1 (1 + \frac{\phi F_1 l}{AD_e}) + \tau_2 (1 + \frac{F_1 l}{AD_e}) + \frac{A\varepsilon l}{F_1} + (1 + \phi)\frac{\varepsilon l^2}{2D^e} + \frac{\varepsilon \phi F_1 l^3}{6A(D^e)^2}] \tag{9.30}$$

Solution of the equations of the inhomogeneous model (Eqs. (9.7), (9.21), (9.22b), (9.23), (9.24b), (9.8), and (9.5b)) leads to the following transfer function between the input (c_1) and output (c_l) concentrations:

$$G_n(s) = \frac{g_{1n}}{(1+\tau_1 s + g_{2n})(\phi + \tau_2 s + g_{2n}) - g_{1n}^2} \tag{9.31}$$

with

$$g_{1n} = \frac{A}{F_1}\int_R D(R)\sqrt{\frac{s}{D(R)}}\frac{1}{sinh(\sqrt{\frac{s}{D(R)}}l)}\varepsilon(R)dR \tag{9.32}$$

$$g_{2n} = \frac{A}{F_1}\int_R D(R)\sqrt{\frac{s}{D(R)}}\frac{cosh(\sqrt{\frac{s}{D(R)}}l)}{sinh(\sqrt{\frac{s}{D(R)}}l)}\varepsilon(R)dR \tag{9.33}$$

Differentiating Eq. (9.31) and using Eq. (9.16), we derive the following expressions for the zero and first moments of the impulse response of the inhomogeneous model:

$$m_{0n} = \frac{1}{1+\phi(1+\frac{F_1 l}{AD_t^e})} \tag{9.34}$$

$$m_{1n} = m_{0n}^2[\tau_1(1+\frac{\phi F_1 l}{AD_t^e}) + \tau_2(1+\frac{F_1 l}{AD_t^e}) + \frac{A\varepsilon l}{F_1} + (1+\phi)\frac{\varepsilon l^2}{2D_t^e} + \frac{\varepsilon\phi F_1 l^3}{6A(D_t^e)^2}] \tag{9.35}$$

where D_t^e is the effective diffusivity given Eq. (9.20).

It is seen by comparing Eqs. (9.30) and (9.35) that by setting the effective diffusivity in the homogeneous model equal to that given by Eq. (9.20), its first moment becomes identical to that of the inhomogeneous model. Therefore, even for the general form of boundary conditions (Eqs. (9.21)-(9.24)), moment analysis of transient experimental data gives the same effective diffusion coefficient as steady-state experiments. Comparison of Eqs. (9.29) and (9.34) reveals that this choice of effective diffusivity also makes the zero moments of the two responses identical. This is a very important observation since the zero moment of the impulse response is the change of the steady-state concentration of the solute at $x = l$ for a unit step change in the input concentration at $x = 0$ (c_1).

In the chomatographic (particle-bed) method, pores of different size share the same concentration at the external surface of the particle, but otherwise, diffusion occurs independently in each pore. The contribution of the intraparticle diffusion process to the second central moment of the bed's response turns out to simply be the average of the diffusion time of a single pore over the pore size distribution (Villermaux, 1987; Cui et al., 1989). (The diffusion time is proportional to $a^2/D(R)$ (cf. Eq. (9.17)), with a being the radius of the particle.) The second central moment of the chromatographic response is thus influenced more strongly by the diffusivity of the small pores, and second moment matching leads to Eq. (9.2), which predicts much smaller effective diffusivities than the value resulting from diffusion-cell experiments (Eq. (9.10) or (9.20)). In the diffusion-cell method, however, there is interaction of the fluxes in different size pores at the end of the sample (see Eqs. (9.8), (9.12b), and (9.23)), and it is actually the large pores that serve as the main transport arteries of the system even under transient conditions. This interaction is further discussed in the following section, where the time domain responses of the homogeneous and heterogeneous models are compared.

9.4. Comparison of the Homogeneous and Inhomogeneous Model Responses in the Time Domain

It was pointed out in the introduction that matching the first two moments of the experimental and theoretical responses of a system does not guarantee good agreement between the concentration vs. time curves in the time domain. It is interesting, therefore, to investigate the relationship of the time-domain responses of the inhomogeneous ('experimental') and homogeneous models after their first two moments have been matched. In order to simplify the analysis, interpretation, and presentation of the results, we will focus on solids with discrete, bimodal distribution of pore size, i.e., solids for which

$$\varepsilon(R)dR = \varepsilon_1\delta(R - R_1) + \varepsilon_2\delta(R - R_2)$$

The impulse responses of the homogeneous and inhomogeneous models for the case of simple boundary conditions (with one of the ends of the diffusion cell closed and without dead space and mass transport limitations at its exposed end, Eqs. (9.11)-(9.14)) are shown in Fig. 9.2. The corresponding curves for a diffusion-cell with both ends exposed to gaseous

streams (boundary conditions given by Eqs. (9.21)-(9.24)) are shown in Fig. 9.3. The Fast Fourier Transform (FFT) method (specifically, a routine described by Press et al. (1986)) was used to invert the transfer functions given by Eqs. (9.16), (9.18), (9.25), and (9.31) and construct the response curves in the time domain. The results shown in the figure are for diffusion in the Knudsen regime in a solid with 0.5 total porosity, equal porosities of large and small pores, and pore size ratio equal to 10. For the case with the general form of boundary conditions (Fig. 9.3), the volumes of the mixing regions next to the two faces of the slab were taken as 1/10 of the volume of the slab, and the dimensionless parameters $AD(R_2)/F_i l$ were set equal to 3. In an actual experiment, the latter value would obtain, for instance, for $A = 2$ cm^2, $D(R_2) = 0.5$ cm^2/s, $l = 0.2$ cm, and $F_i = 100$ cm^3/min.

The response curves have been rendered independent of the type of the solute, sample thickness, and pore size by using the dimensionless time $tD(R_2)/l^2$ instead of the real time. Since diffusion occurs in the Knudsen regime, the diffusivity ratio is equal to the pore size ratio, i.e., $D(R_1) = D(R_2)/10$. Using this relationship and Eq. (9.10) or (9.20), we find that the effective diffusivity of the homogeneous model that is obtained from steady-state experiments or from transient experiments through moments matching is equal to $0.275D(R_2)$. Use of the particle-bed diffusivity expression of Cui et al. (Eq. (9.2)) gives about three times smaller effective diffusivity ($D^e = 0.090909\cdots D(R_2)$). When the simple set of boundary conditions (Eqs. (9.11)-(9.14)) is employed, the first moment of the homogeneous model with effective diffusivity given by Eq. (9.2) is about three times larger than the first moment of the homogeneous model (2.75 vs. $0.90909\cdots$, in dimensionless units). Thus, it is hardly surprising that the response curves of the homogeneous model with effective diffusivity given by Eq. (9.2) (chain-dot curves in Figs. 9.2 and 9.3) have pactically no relation to the 'actual' response curves of the system, that is, the response curves of the inhomogeneous model (solid curves). It should be pointed out that the second moment of the inhomogeneous model is larger than that of the homogeneous model with D^e from Eq. (9.10) or (9.20), in agreement with the conclusions of Burghardt et al. (1988), but smaller than the value obtained when the chromatographic diffusivity (Eq. (9.2)) is employed. For instance, for the cases shown in Fig. 9.2, the second moment of the inhomogeneous model is $1.935\cdots$, while that of the homogeneous model is 1.377 for D^e

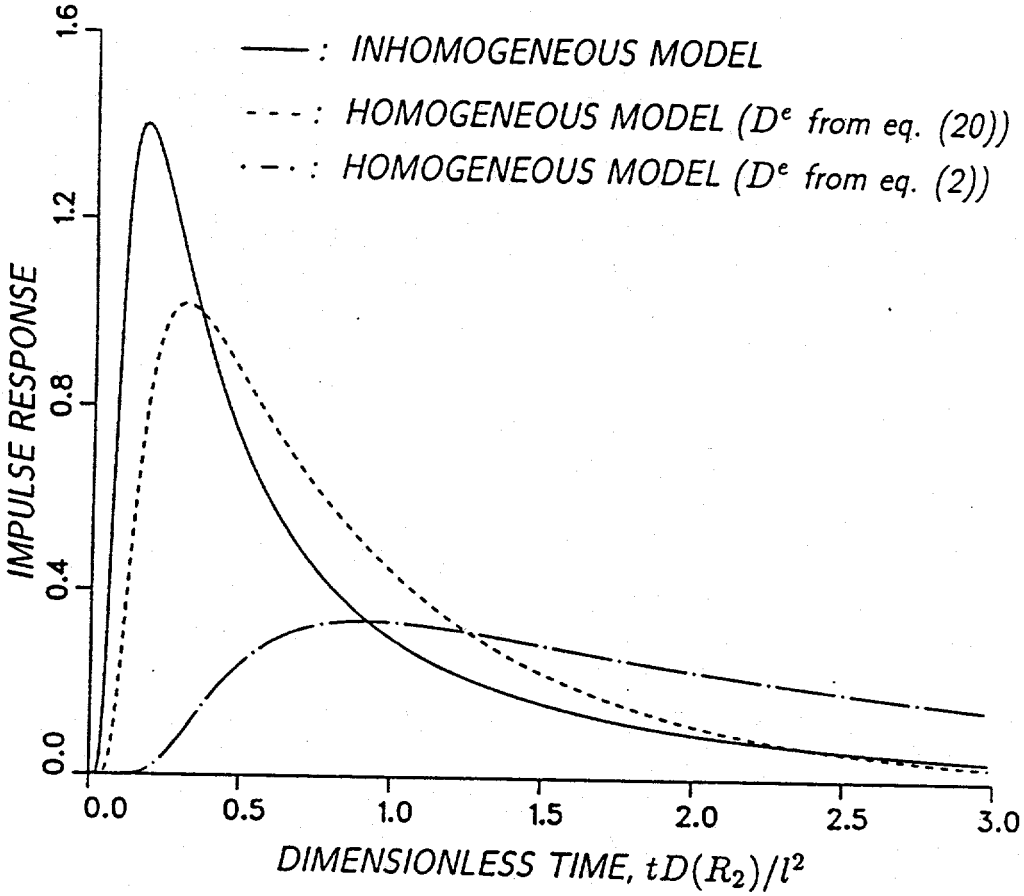

Figure 9.2: Impulse response curves of the homogeneous and inhomogeneous models for a diffusion cell with aclosed end (boundary conditions given by Eqs. (9.11)-(9.14)). $\varepsilon_1 = \varepsilon_2 = 0.25$; $R_1 = 0.1R_2$.

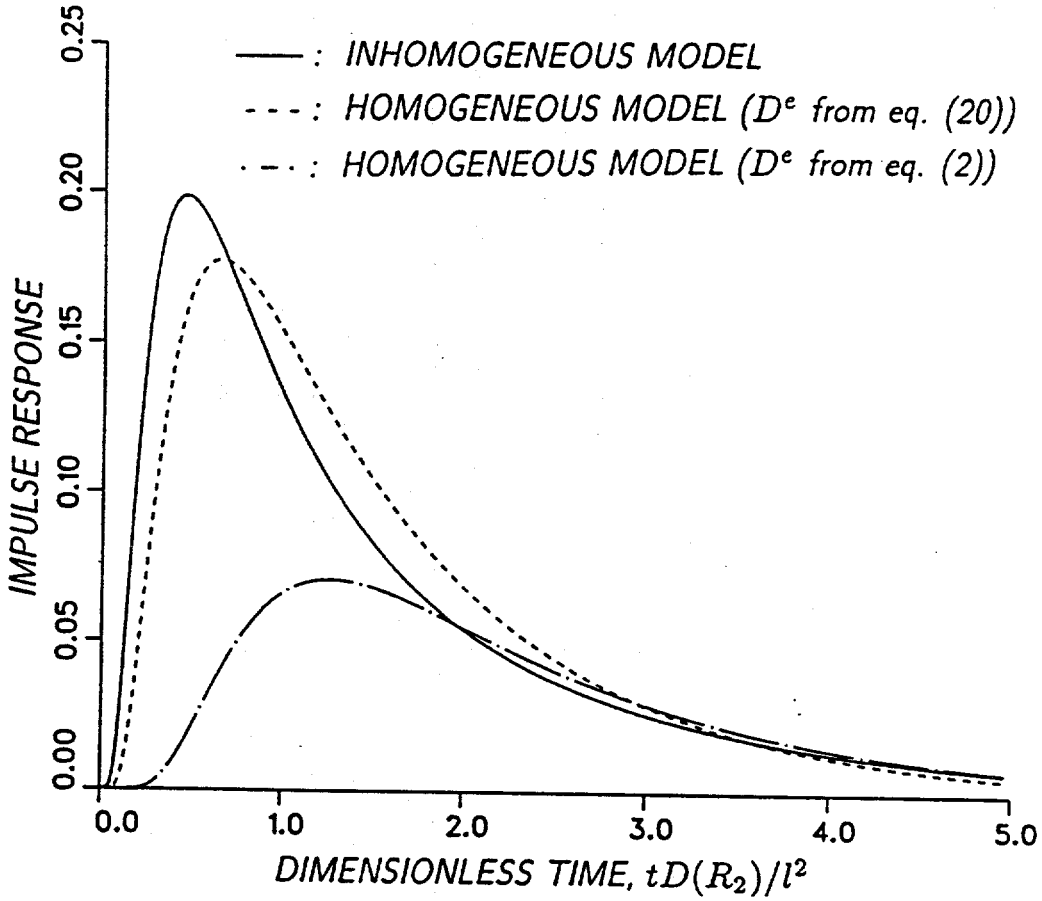

Figure 9.3: Impulse response curves of the homogeneous and inhomogeneous models for a diffusion cell with gaseous flow over both ends (boundary conditions given by Eqs. (9.21)-(9.24)). $\varepsilon_1 = \varepsilon_2 = 0.25$; $R_1 = 0.1R_2$; $\frac{V_i}{Al} = 0.1$; $\frac{AD(R_2)}{F_i l} = 3$.

from Eq. (9.20) and 12.60 for D^e from Eq. (9.2).

Although the impulse response of the homogeneous model (with D^e from Eq. (9.10) or (9.20)) has the same zero and first moments as the response of the inhomogeneous model, Figs. 9.2 and 9.3 show that there are significant differences between the response curves in the time domain. These differences are mainly due to the existence of two time constants, differing by an order of magnitude, for gaseous diffusion in the inhomogeneous (heteroporous) solid and the use of a single time constant in the homogeneous model. By using a single time constant, it is impossible to simultaneously capture the fast dynamics of the large pores and the slow response of the small pores, and as a result, the homogeneous model tends to underpredict the system's response for small and large values of time. This behavior is in qualitative agreement with some results obtained by Mo and Wei (1986) from the numerical solution of the diffusion equation on a lattice simulating the structure of a partially blocked ZSM-5 zeolite. Mo and Wei found that the steady-state effective diffusivity was the lower limit (for increasing time) of a transient effective diffusivity based on the instantaneous mass transport flux through the sample.

When only one end of the diffusion cell is exposed to a gaseous stream, the total flux at its closed end must obviously be zero at all times, and consequently, the diffusion flux in the small pores there must be the negative of the diffusion flux in the large pores. This situation is illustrated in Fig. 9.4 which presents dimensionless concentration profiles in the diffusion cell at various times following a step change (from zero) in the concentration of the tracer gas (solute) at its exposed end. The results of the figure show that the concentration gradient in the small pores at the closed end of the slab is always positive, and consequently, there is net flow of tracer gas in the small pores through both ends at all times. It is thus the large pores that serve as the transport arteries of the porous slab under unsteady conditions, and therefore, concentration equilibration in the small pores takes place much faster than it would if transport in them occurred independently of that in the large pores – as it is the case in particle-bed experiments (Eq. (9.2)).

Fig. 9.5 presents the evolution of the dimensionless concentration profiles in the two pore families following a step change (from zero) in the concentration of the tracer gas at $x = 0$ when both ends of the diffusion cell are exposed to flowing streams. Although in

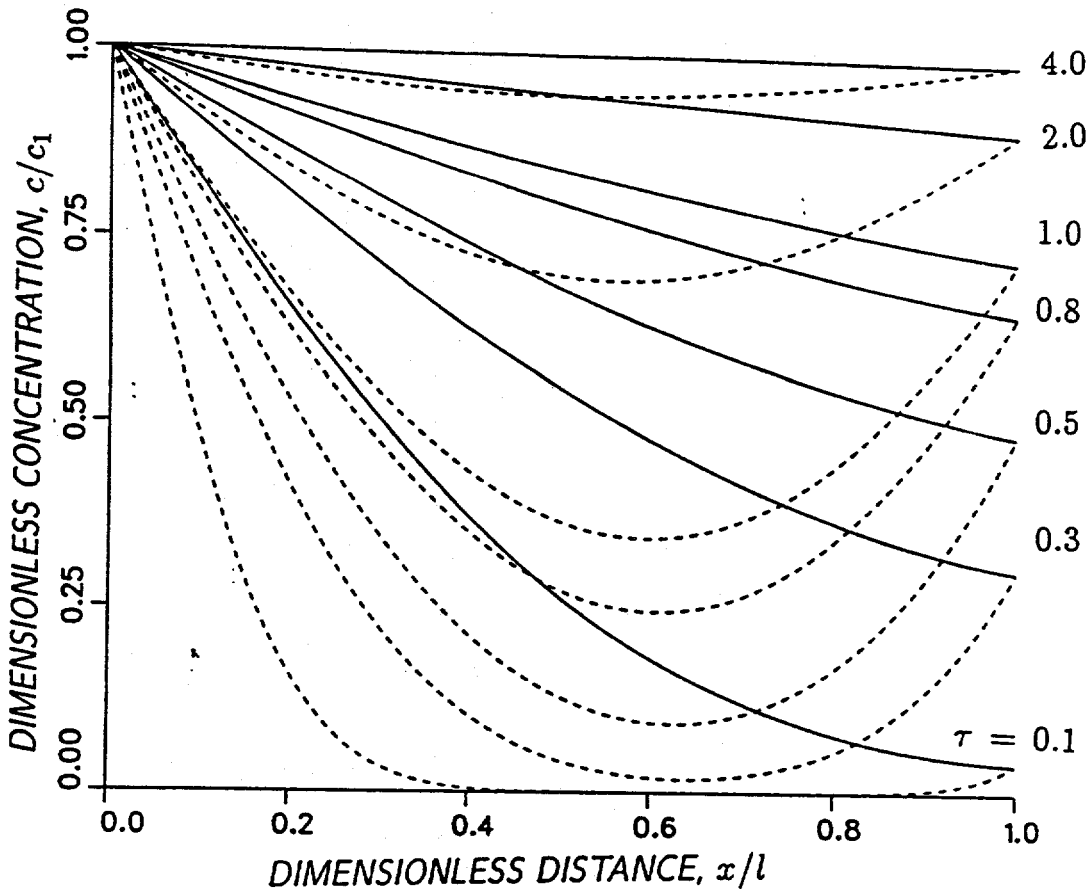

Figure 9.4: Dimensionless concentration profiles in a diffusion cell with closed end (boundary conditions given by Eqs. (9.11)-(9.14)) at various times for a step change (of magnitude c_1) in the concentration of the stream flowing over its open end. Model parameters same as in Fig. 9.2. —: concentration in pores of radius R_2; - - -: concentration in pores of radius R_1.

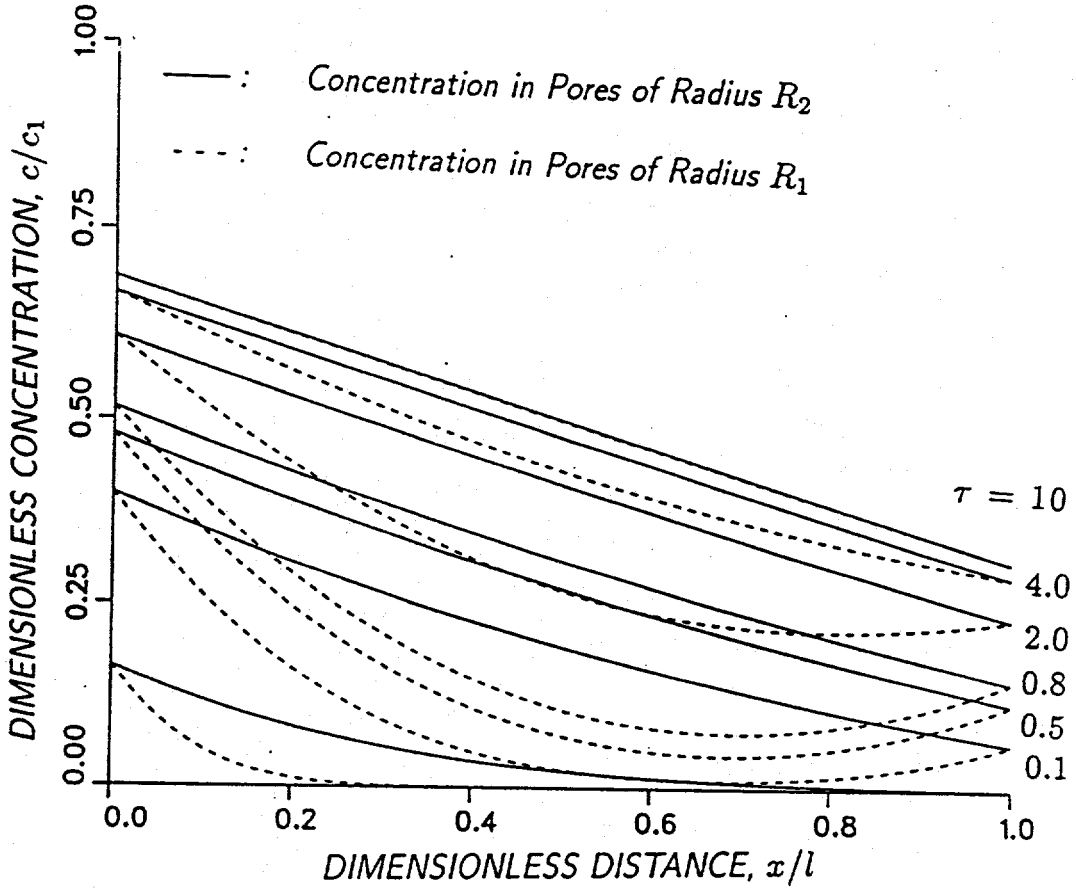

Figure 9.5: Concentration profiles in a diffusion cell with both ends exposed to gaseous streams (boundary conditions given by Eqs. (9.21)-(9.24)) at various times for a step change (of magnitude c_1) in the concentration of the stream flowing over one end. Model parameters same as in Fig. 9.3. —: concentration in pores of radius R_2; - - -: concentration in pores of radius R_1.

this case the total diffusion flux at $x = l$ is not zero, the concentration gradient in the small pores at this point is again positive during the initial stages of the transient response of the system, and therefore, mass transport from one end of the slab to the other occurs through the large pores only. Only after the concentration profile gets close to steady state, the concentration gradient in the small pores at $x = l$ becomes negative, and direct contribution of these pores to the mass transport rate through the slab starts to take place. Both in Figs. 9.4 and 9.5, the concentration profile in the large pores becomes almost linear after the initial stages of the transient process, indicating that the diffusion process in the large pores is at pseudosteady state. This situation is obviously expected since the time constant for diffusion in the pores is inversely proportional to the pore size, and hence, it is an order of magnitude smaller for the large pores.

If the Fast Fourier Transform method is used to compute the concentration profiles shown in Figs. 9.4 and 9.5, complete response curves must be constructed at various positions within the cell. This turns out to be a computationally intensive task since both a very high sampling frequency and a large interval of time must be employed to capture the slow and fast dynamics of the local responses. For this reason, the results shown in Fig. 9.4 and 9.5 were obtained using cubic B-spline collocation (De Boor, 1978) to discretize the inhomogeneous model equations (Eqs. (9.7) and (9.11)-(9.14) or (9.21)-(9.24)) and time-integration of the resulting system of algebraic and ordinary differential equations with a Gear-type solver (Gear, 1971).

We have seen in Figs. 9.2 and 9.3 that despite having the same first two moments, the impulse responses of the homogeneous and inhomogeneous model exhibit marked differences in the time domain. It was thus decided to examine how the response curves of the homogeneous model for effective diffusivities obtained through a time-domain parameter estimation compare with that of the inhomogeneous model. Effective diffusivities were thus determined by minimization of the weighted integral square difference of the impulse responses of the homogeneous and inhomogeneous model, that is, by minimization of the functional

$$f = \int_0^\infty w(t)(y_n(t) - y_h(t))^2 dt \tag{9.36}$$

where $w(t)$ is the weight function: 1, t, or t^2. The Fast Fourier Tranform method was

used to obtain the homogeneous and inhomogeneous model responses, y_h and y_n, and as a result, the equivalent finite sum form of functional f was employed in the computations. The upper limit of the time interval used in the evaluation of the functional was set equal to 8 times the first moment of the normalized impulse response of the inhomogeneous model.

Method	$D_t^e/D(R_2)$	Zero Moment	First Moment
Moments	0.275	1.0	0.9090
$w(t) = 1$	0.4046	1.0	0.6178
$w(t) = t$	0.3673	1.0	0.6805
$w(t) = t^2$	0.30862	1.0	0.8100

Table 9.1: Effective Diffusivities from Moments Matching or Time-Domain Parameter Estimation on the Diffusion-Cell with Closed End.

The obtained diffusivities through the above parameter estimation scheme for the diffusion cells used to get the results of Figs. 9.2 and 9.3 are given in Tables 9.1 and 9.2. Shown in the tables are also the values of the first and zero moments of the homogeneous model for the estimated effective diffusivity. The impulse response curves of the homogeneous model for the effective diffusivities of Tables 9.1 and 9.2 are compared with the impulse response of the inhomogeneous model in Figs. 9.6 and 9.7. Notice that when both ends of the cell are exposed to flowing streams, both the first and the zero moments of the impulse response of the homogeneous model are functions of the effective diffusivity. Therefore, in this case one has the choice of using the impulse response or its normalized form in the parameter estimation scheme.

The results of Tables 9.1 and 9.2 show that time-domain parameter estimation gives effective diffusion coefficients larger, in general, than the value obtained through moments matching. The only exception is the case with $w(t) = t^2$ and the general form of boundary conditions (Table 9.2 and Fig. 9.7). The main reason for this occurrence is that the time-domain parameter estimation process – especially if the normalized form of the response is

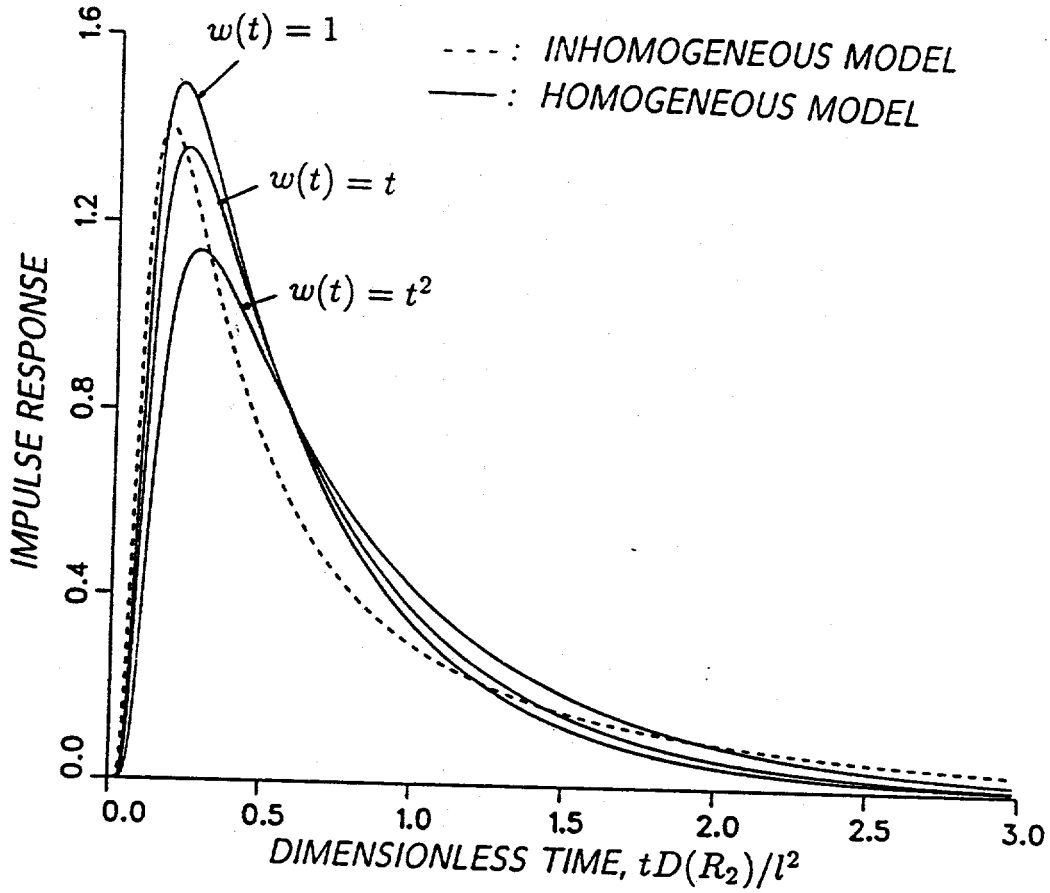

Figure 9.6: Comparison of the impulse response of the inhomogeneous model with the impulse responses of the homogeneous model for effective diffusivities estimated through curve fitting using different weight functions in the expression for the square error (see Table 9.1). The diffusion cell has one of its ends closed, and the model parameters are the same as those of Fig. 9.2.

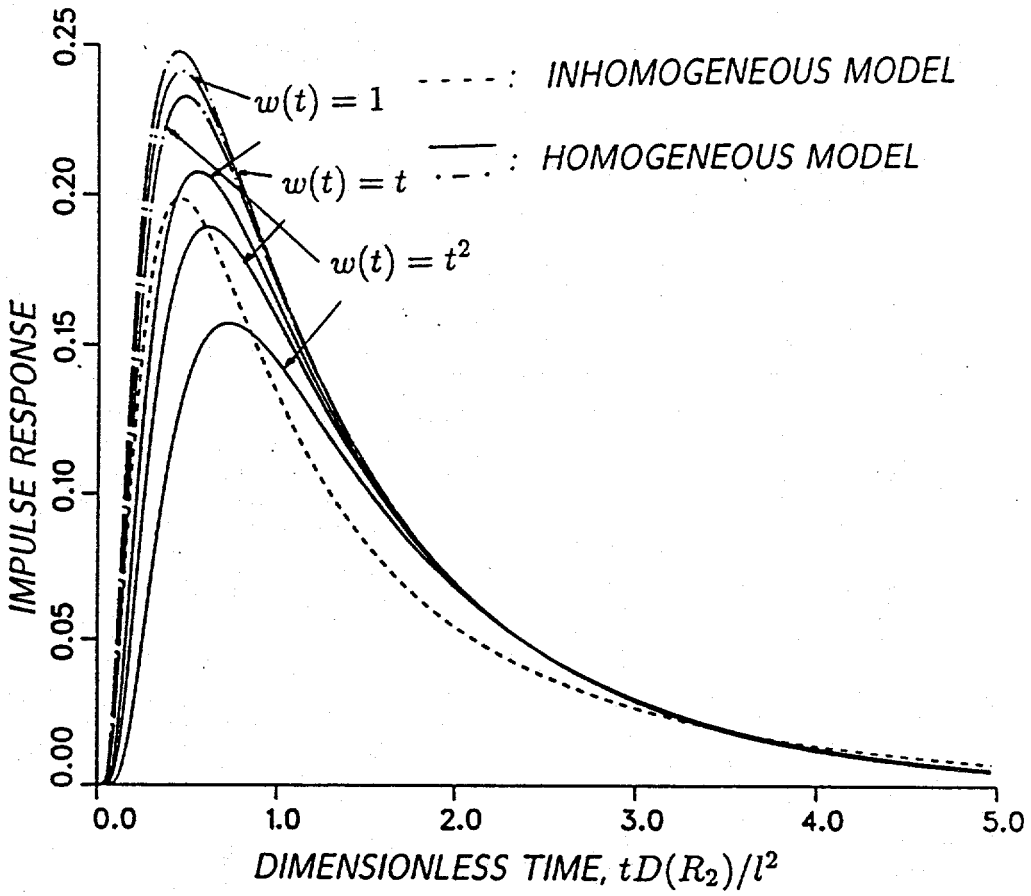

Figure 9.7: Comparison of the impulse response of the inhomogeneous model with the impulse responses of the homogeneous model for effective diffusivities estimated through curve fitting using different weight functions in the expression for the square error (see Table 9.2). The diffusion cell has both ends exposed to gaseous flow, and the model parameters are the same as those of Fig. 9.3. The chain-dotted (– · –) curves were obtained by matching the normalized impulse responses of the inhomogeneous and of the homogeneous models.

used – places more weight on the initial response of the system where the impulse response has larger values. As more weight is put on the difference between the homogeneous and inhomogeneous impulse responces at large times, by using weight functions t and t^2, the effective diffusivity becomes smaller and the response curve moves to the right – except when the normalized response is used with $w(t) = t$ in Table 9.2 and Fig. 9.7. Using $w(t) = t$ appears to give the best, in a qualitative sense, results, but it should be kept in mind that unless the effective diffusivity obtained via moments matching is used, the steady-state behavior will not be predicted by the homogeneous model. Only the effective diffusivity given by Eq. (9.10) or (9.20) reproduces the zero moment of the response, which as we have already mentioned is the steady state concentration at $x = l$ for $c_1 = 1$ and $c_2 = 0$.

Method	$D_i^e/D(R_2)$	Zero Moment	First Moment
Moments	0.275	0.3113	0.4858
$w(t) = 1$	0.3578	0.3411	0.4972
$w(t) = t$	0.3048	0.3232	0.4906
$w(t) = t^2$	0.2290	0.2894	0.4762
$w(t) = 1^*$	0.4805	0.3712	0.5067
$w(t) = t^*$	0.5082	0.3765	0.5082
$w(t) = t^{2*}$	0.4465	0.3641	0.5046

Table 9.2: Effective Diffusivities from Moments Matching or Time-Domain Parameter Estimation on the Diffusion-Cell with both ends open. (*Using the normalized form of the impulse response.)

For the simple set of boundary conditions (Eqs. (9.11)-(9.14)), the first moment is inversely proportional to the effective diffusivity (see Eq. (9.17)), and as a result, the relative differences among the first moments of Table 9.1 are proportional to those among the effective diffusivities. However, as the results for the first moments of Table 9.2 show, when both ends of the diffusion cell are exposed to flowing streams (the standard experimental arrangement), the sensitivity of the first moment to the effective diffusivity is considerably

weaker. This different behavior is due to the fact that the contributions of the dynamics of the mixing chambers to the overall first moment (see Eq. (9.30)) are weakly influenced by the effective diffusivity. There are two important consequences of this observation for those using transient operation of a diffusion cell to extract effective diffusivities. First, sufficient information on the dynamics of the mixing chambers must be available to obtain accurate effective diffusivity estimates. Second, small errors in the moments may produce large errors in the diffusion coefficient estimates.

9.5. Pore Interlinking and Mismatch between the Homogeneous and Inhomogeneous Model Responses

The parallel pore model does not offer an acceptable representation of the internal structure of porous media encountered in practical applications. Its main drawback is that it does not allow for pore communication in the interior of a porous sample, and as a result, the concentration fields in pores of different size interact only at the external surface of the sample. Real porous media, however, exhibit a highly interconnected pore structure – a point in the interior can be reached from almost any point of the external surface – and with such frequency that in most cases it is impossible to discern long uninterrupted pore segments between pore intersections. Thus, in this section we will examine how the mismatch between the responses of the inhomogeneous and homogeneous models (with D^e given by Eq. (9.10) or (20)) is affected by pore communication (pore interlinking) in the interior of the porous medium.

A simple porous medium with interconnected pores, probably the simplest, is obtained by considering a laminated structure in which each lamina is topologically equivalent to the parallel pore structure of Fig. 9.1, that is, it contains parallel, noninteracting pores arranged perpendicularly to its faces. Between two adjacent laminae, there exists a thin void layer whose sole function is to preserve the continuity of diffusion paths between adjacent laminae and equilibrate the concentration there. The assumption that the concentration is uniform in the region between adjacent laminae does not necessarily imply that there is no diffusion resistance in this region parallel to the faces of the slab. It simply means that over the smallest region of the face of each lamina that is statistically

representative of the cross-section of the pellet at large – that is, it contains a statistically representative sample of pore mouths – concentration differences are negligible. A structure consisting of k laminae of equal thickness l/k is schematically shown in Fig. 9.8. Obviously, if only one layer is considered, the parallel pore structure considered thus far in our analysis (Fig. 9.1) is obtained.

In the diffusion cell experiment, the laminated structure is assumed to be positioned in such a way that diffusion takes place parallel to the pores, as in Fig. 9.1. Eq. (9.7) now holds in the interior of each lamina, and Eqs. (9.11)-(9.14) or (9.21)-(9.24) are still the boundary conditions at the two faces of the porous slab. Let $c^i(R)$ be the concentration in the interior of the ith lamina in a pore of radius R. Continuity of flux and concentration at $x = \frac{il}{k}$ requires that

$$\int_R D(R)\frac{\partial c^i(R)}{\partial x}\varepsilon(R)dR|_{x=(\frac{il}{k})^-} = \int_R D(R)\frac{\partial c^{i+1}(R)}{\partial x}\varepsilon(R)dR|_{x=(\frac{il}{k})^+} \tag{9.37}$$

$$c^i(R)|_{x=(\frac{il}{k})^-} = c^{i+1}(R)|_{x=(\frac{il}{k})^+} = c_n^i \tag{9.39}$$

with c_n^i being the concentration, common for all pores, of the inhomogeneous model at $x = il/k$. Obviously,

$$c_n^0 = c_0; \quad c_n^k = c_l \tag{9.39a,b}$$

Using the solution of Eq. (9.7) in each layer, Eq. (9.37) takes the form

$$\alpha c_n^{i+1} - c_n^i + \alpha c_n^{i-1} = 0; \quad \alpha = g_{3n}/2g_{4n} \tag{9.40a,b}$$

with

$$g_{3n} = \int_R D(R)\sqrt{\frac{s}{D(R)}}\frac{1}{sinh(\sqrt{\frac{s}{D(R)}}\frac{l}{k})}\varepsilon(R)dR \tag{9.41}$$

$$g_{4n} = \int_R D(R)\sqrt{\frac{s}{D(R)}}\frac{cosh(\sqrt{\frac{s}{D(R)}}\frac{l}{k})}{sinh(\sqrt{\frac{s}{D(R)}}\frac{l}{k})}\varepsilon(R)dR \tag{9.42}$$

Solving the difference equation described by Eq. (9.40a) and using Eq. (9.39) and the general form of boundary conditions, we get, after some manipulations, that

$$G_n(s) = \frac{c_l}{c_1} = \frac{f_1(\rho_2 - \rho_1)}{f_2 f_3(\rho_2^k - \rho_1^k) - f_1(f_2 + f_3)(\rho_2^{k-1} - \rho_1^{k-1}) + f_1^2(\rho_2^{k-2} - \rho_1^{k-2})} \tag{9.43}$$

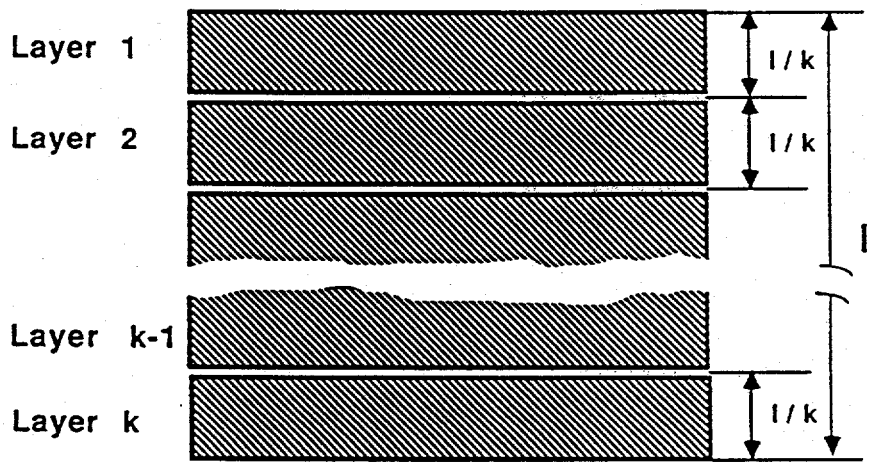

Figure 9.8: Schematic representation of a multilayered slab. The pore structure of each layer is the same as that shown in the circled graph of Fig. 9.1.

with

$$\rho_{1,2} = \frac{1 \pm \sqrt{1 - 4\alpha^2}}{2\alpha} \tag{9.44}$$

$$f_1 = \frac{A}{F_1} g_{3n};\ f_2 = 1 + \tau_1 s + \frac{A}{F_1} g_{4n};\ f_3 = \phi + \tau_2 s + \frac{A}{F_1} g_{4n} \tag{9.45a-c}$$

By setting $\tau_1 = \tau_2 = \phi = 0$ and letting $F_1 \to \infty$, Eq. 9. (43) gives the transfer function for the simple set of boundary conditions (Eqs. (9.11)-(14)), which turns out to be

$$G_n(s) = \frac{g_{3n}(\rho_2 - \rho_1)}{g_{4n}(\rho_2^k - \rho_1^k) - g_{3n}(\rho_2^{k-1} - \rho_1^{k-1})} \tag{9.46}$$

For $k = 1$, Eqs. (9.43) and (9.46) take the form of Eqs. (9.31) and (9.18), respectively. It is possible to further simplify Eqs. (9.43) and (9.46), but such a simplification is unnecessary for their inversion using the Fast Fourier Transform method.

The expressions for the first and zero moments of the impulse response of the transfer functions of Eqs. (9.43) and (9.46) are again derived using Eq. (9.16). After a number of algebraic manipulations, one finds that the zero and first moments of the impulse response of a multilayered slab are independent of the number of layers, k, for both types of boundary conditions. Thus, the zero moment of the impulse response of Eq. (9.46) is unity, its first moment is given by Eq. (9.19), and the zero and first moments of Eq. (9.43) are given by Eqs. (9.34) and (9.35), respectively. This result obviously implies that the effective diffusivity in a multilayered slab that is obtained through moments matching is independent of the number of layers and is given by Eq. (9.10) or (9.20).

Increasing the number of laminae in the slab increases the degree of interaction of pores of different size in the porous medium. The effects of pore interlinking on the response of the diffusion cell may therefore be investigated by examining how the number of laminae influences the behavior of the system. Figs. 9.9 and 9.10 present impulse response curves, constructed by inverting Eqs. (9.46) and (9.43), respectively, for various values of k, with each layer in the slab characterized by discrete, bimodal distribution of pore size. The pore size distribution and the other parameters of the cell are identical to those used to obtain the results of Figs. 9.2-9.7 for the single layer slab. It is seen that as the number of layers is increased and the degree of pore interaction between the two sides of the porous slab rises, the response of the diffusion cell (inhomogeneous model) gets closer

to that predicted by the homogeneous model using the effective diffusivity of Eq. (9.10) or (9.20) (dashed curve). Even with only two layers in the porous slab, that is, with the pores interacting only at a single point, there is a dramatic decrease in the difference between the inhomogeneous and the homogeneous model response. With both ends of the cell exposed, the response of the inhomogeneous system becomes almost identical, for most practical purposes, to that of the homogeneous model for less than 8 layers in the slab. However, since the two responses are further apart when the simple set of boundary conditions is used, it takes more layers for the difference between the two responces to be reduced to a similar extent in this case (compare Figs. 9.9 and 9.10). In the hypothetical situation of an infinite number of pore layers, a perfectly inteconnected pore network obtains, in which the microscopic concentration field in each pore coincides with the macroscopic one given by the homogeneous model with D^e taken from Eq. (9.10) or (9.20).

The above observations point to the conclusion that under conditions of pore communication – as it is expected to be the case in an actual porous medium – the disagreement between the predictions of the homogeneous and inhomogeneous model might not be of such magnitude to justify the use of a complex inhomogeneous model to describe the diffusion process. It can thus be argued that provided that a diffusion flux model consistent with the topology of the pore structure of the porous medium is employed (Sotirchos, 1989), a pseudohomogeneous model employing effective values for the various transport properties may provide a satisfactory description not only of the steady-state but also of the transient processes occurring in a solid with distributed pore size.

9.6. Summary and Concluding Remarks

The relation between the effective diffusion coefficients of nonadsorbing gases obtained from steady-state and transient diffusion-cell experiments was investigated in this study. A simple geometrical model consisting of parallel noninteracting pores, of some pore size distribution (parallel bundle pore model), was used to represent the physical structure of the porous medium, and two different experimental arrangements were employed in the analysis of the system; namely, one in which the concentration of the tracer gas is monitored at a closed end of the diffusion cell and another in which gaseous streams flow over

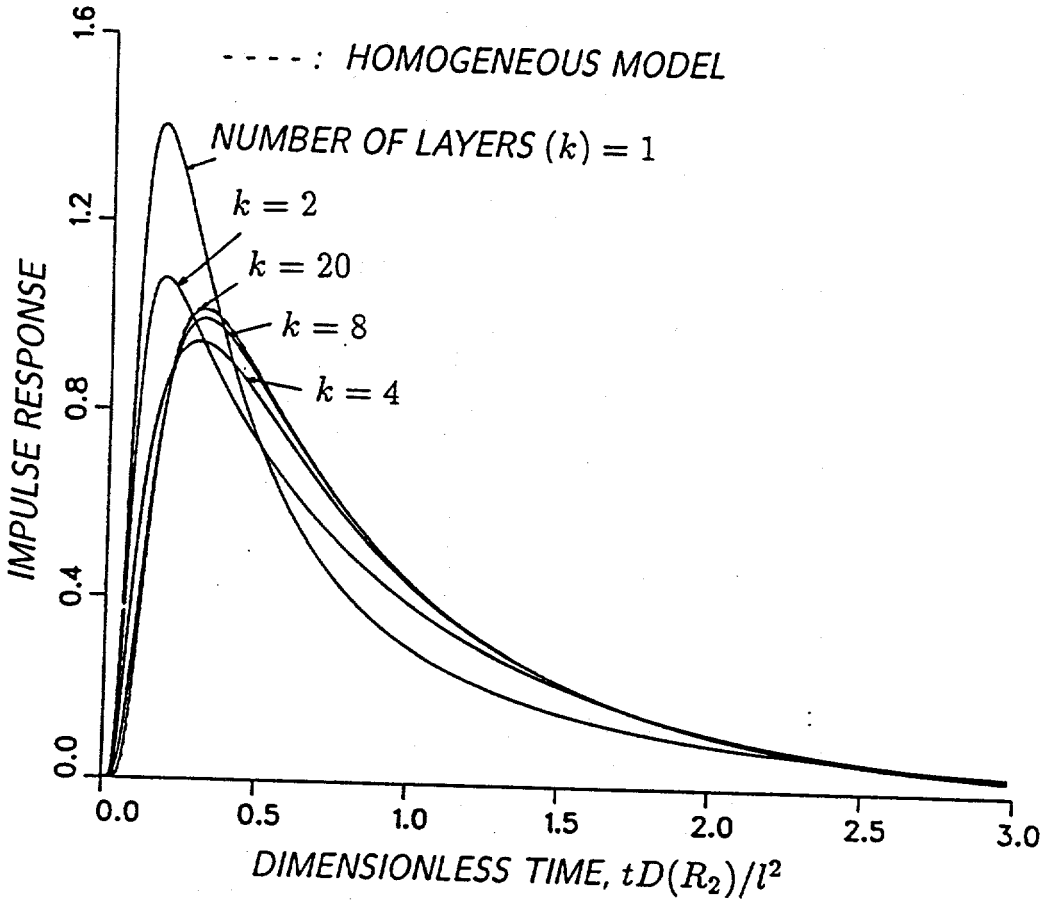

Figure 9.9: Effect of the number of layers in a sample of fixed thickness on the impulse response of the homogeneous model (D^e from Eq. (9.10) or (9.20)) for a diffusion cell with closed end. Model parameters same as in Fig. 9.2.

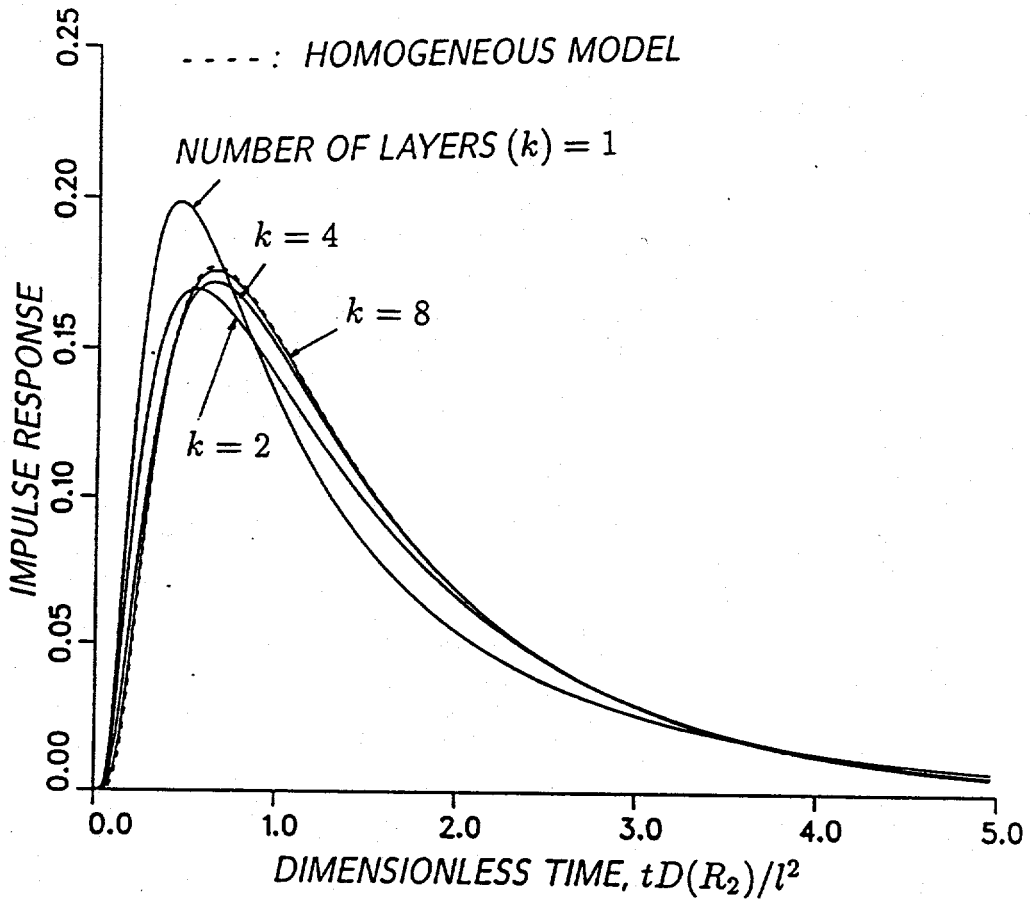

Figure 9.10: Effect of the number of layers in a sample of fixed thickness on the impulse response of the homogeneous model (D^e from Eq. (9.10) or (9.20)) for a diffusion cell with both ends exposed to gaseous flow. Model parameters same as in Fig. 9.3.

both faces of the porous slab. The parallel pore model does not permit communication of pores in the interior of the porous slab, and thus, in order to examine the effects of pore interlinking on our conclusions, we also studied the diffusion problem in a laminated structure, in which the pore structure of each lamina is described by the parallel bundle pore model.

The analysis of the problem showed that the effective diffusivity determined by matching the zero and first moments of the experimental (inhomogeneous model) response of the diffusion cell with the corresponding moments of the response of the homogeneous model is identical to the effective diffusion coefficient derived from steady-state diffusion cell experiments. Because of the existence of different time constants for diffusion in a solid with a pore size distribution, the time-domain response predicted by the homogeneous model, which has a single time constant, is different from that of the inhomogeneous model. If a time-domain parameter estimation scheme is employed, the obtained effective diffusivities are, in general, larger than the steady-state value. These findings are in sharp contrast with the conclusions reached by Cui et al. (1989, 1990) from their analysis of particle-bed transient data, where it was found that effective diffusivities extracted from particle-bed experiments through moment matching for solids with distributed pore size and noninteracting pores (parallel bundle model) can be smaller, by a few orders of magnitude in some cases, than the steady-state diffusivities.

Allowing for pore communication in the interior of the porous solid causes a dramatic reduction in the difference between the responses of the homogeneous and inhomogeous model in the time domain. It can thus be argued that the intrinsic inability of a pseudo-homogeneous model to describe diffusion and reaction in a physically inhomogeneous pore structure might not be an issue in practical applications, and that explanations for any discrepancies between transient and steady-state estimates of effective diffusivities from diffusion-cell experiments should be sought elsewhere. It should be pointed out that in their comparative study of measuring methods of effective diffusivities in porous catalysts, Baiker et al. (1982) obtained experimental results that are in agreement with the conclusions of my study and of the study of Burghardt et al. (1988). The steady-state diffusion-cell effective diffusivities in the industrial catalysts they studied were found to be

practically the same as, or in a few cases slightly smaller than, the transient effective diffusivities measured using the same unit. Only when the particle-bed method was used, the dynamic diffusivities were significantly smaller than the steady-state values, in agreement with the analysis of Cui et al. However, Baiker et al. concluded that the differences between the particle-bed and diffusion-cell results were within reasonable limits considering the sources of uncertainty in the bed experiments.

9.7. Notation

Symbols that do not appear here are defined in the text.

c	concentration, $kmol/m^3$
c_0	concentration at $x = 0$, $kmol/m^3$
c_l	concentration at $x = l$, $kmol/m^3$
c_i	inlet concentration of the stream flowing over face i of the slab, $kmol/m^3$
$c(R)$	concentration in a pore of radius R, $kmol/m^3$
$c^i(R)$	concentration in a pore of radius R in layer i of a multilayered slab, $kmol/m^3$
c_n^i	concentration at the interface of layer i and $i+1$ of a multilayered slab, $kmol/m^3$
D^e	effective diffusion coefficient, m^2/s
D_s^e	steady-state effective diffusion coefficient, m^2/s
D_t^e	transient effective diffusion coefficient, m^2/s
f_i	parameters defined in Eq. (9.45)
F_i	flow rate of the stream flowing over face i of the slab, m^3/s
g_{ih}	parameters defined in Eqs. (9.26) and (9.27)
g_{in}	parameters defined in Eqs. (9.32), (9.33), (9.41), and (9.42)
$G(s)$	transfer function between c_l (output) and c_1 (input)
k	number of laminae in a multilayered slab
l	slab thickness, m
m_i	ith moment of impulse response, m^i
N	diffusion flux, $kmol/m^2 \cdot s$
$N(R)$	diffusion flux in a pore of radius R, $kmol/m^2 \cdot s$